Beyond 5G White Paper
6G Radio Technology Project
“Radio Propagation Technology”

Version 1.1
September 30, 2025
XG Mobile Promotion Forum

XGMF

【Revision History】

Ver.	Date	Contents	Note
1.0	2025.5.7	Initial version	
1.1	2025.9.30	Revised version	

Preface

The Radio Propagation Working Group of 6G Radio Technology Project, established within the XG Mobile Promotion Forum (XGMF), produced this white paper. It describes world trends in standardization and academia in radio propagation and Japan's efforts in the related fields. This white paper was prepared with the generous support of many who participated in the Radio Propagation Working Group. In particular, Chapter 1 was compiled by Mr. Kuno (NTT DOCOMO) with the help of Mr. Fukui (SHARP), Ms. Hirata (SHARP), Dr. Yokomakura (SHARP), Dr. Suyama (NTT DOCOMO), Dr. Omote (SoftBank), Dr. Yamada (NTT), Prof. Kim (Niigata University), Mr. Matsuno (KDDI Research, Inc.), and Mr. Nagao (KDDI Research, Inc.). Chapter 2 was compiled by Mr. Ito (KDDI Research, Inc.) with the help of those who introduced their activities. I would like to express my sincere gratitude to all of you who have contributed so much to this white paper. The cooperation of telecommunications industry players, academia experts, and representatives of various industries other than the communications industry has also been substantial. Thanks to everyone’s participation and support, I believe this white paper covered a lot of helpful information for future mobile system development and business creation discussions between industry, academia, and government and for investigating solutions to social issues in the telecommunications industry and across all sectors. We hope this white paper will help Japan create a better future for society and promote significant global activities.

Tetsuro Imai

Tokyo Denki University

I. Trends of Radio Propagation towards Beyond 5G/6G

This chapter introduces recent standardization and academic activities related to radio propagation. I-1 "Recent Standardization Activities" reports the standardization trends in 3GPP Release 19 and ITU-R. I-2 "Recent Academic Activities" reports the academic trends in Japan.

I-1. Recent Standardization Activities

I-1.1. 3GPP Release 19

I-1.1.1. Channel Modelling for System Design

Toward starting 6G studies in 3GPP Release 20, 3GPP is studying on channel modelling enhancements for FR3 (Frequency Range 3), i.e., 7-24GHz [1]. FR3 has great potential to expand mid-band spectrum while enabling macro deployment (e.g., sub-urban macro: SMa) for wider bandwidth and coverage. Furthermore, the adoption of massive MIMO for FR3 introduces challenges such as near-field effects and spatial non-stationary effects, where different spatial channels can be observed by different antenna elements.

I-1.1.2. ISAC Channel Modelling

For ISAC realization in 6G, the discussion of ISAC channel modeling started from the May 2024 meeting based on the following formula [2], [3].

$$H_{ISAC} = H_{target} + H_{background}$$

It was first agreed that the ISAC channel model should consist of two channels: a target channel influenced by the sensing target and a background channel unaffected by the target. Six modes of monostatic or bistatic sensing between the TRP and the target were defined. In addition to the target, for example, an object that is different from the target but knows its location is defined as environment object (EO), and the discussion started based on how to determine the details of each channel of the target, background, and EO. Furthermore, environmental objects are classified into EO type-1 if they are the size and shape equivalent to the sensing target (For example, people, UAV, AGV etc.), and EO type-2 if they are much larger than the target (For example, walls, buildings, grounds, etc.), and the effects of each type will be discussed in detail [3].

The basis such as the generation of stochastic clusters by the target channel, and the deterministic parameters at the TRP and target were started by using the existing model of TR38.901 [4]. And it was agreed that the scattering point in the target is divided into single case and multiple case, and that the sensing is mainly by the value of RCS (radar reflection cross section) in the single scattering point [5], [6]. In addition to discussing the RCS model for each target, the remaining issues such as target polarization, diffraction/blockade modeling, multi-scattering point target modeling, EO type-2 modeling, and spatial consistency modeling are being discussed at the recent meeting [7], [8].

I-1.2. ITU-R

I-1.2.1. NTN

HAPS (High Altitude Platform Stations) and NTN (Non-Terrestrial Networks) may share frequencies with terrestrial networks and other radio systems. Therefore, accurate estimation of radio propagation characteristics is very important for system design and interference study of HAPS and NTNs. The ITU-R is standardizing a “Radio Propagation Estimation Method for Interference Study” to evaluate interference between different radio systems. This provides a foundation for smooth frequency sharing.

Japan has contributed to the international standardization activities for ITU-R Recommendation P.1409, which is a radio propagation estimation method for HAPS, and its related recommendations in ITU-R SG3. These include models for estimating radio propagation characteristics under various environments assumed in HAPS, etc. Some of the models are applicable not only to HAPS but also to other NTNs, thus expanding the scope of standardization.

I-1.2.2. ITU-R SG 3 and SG 5 WP5D

Propagation loss estimation methods for the 4.4–4.8 GHz, 7.125–8.4 GHz, and 14.8–15.35 GHz bands are actively studied in SG 3 toward 6G. And the research is also advanced on the propagation loss estimation method over 100 GHz in anticipation of future sub-terahertz band applications. These are expected to be published as recommendations at the SG 3 meeting to be held in June 2025. Many contribution documents from Japan have been inputted into the Propagation Estimation Method Rec. P.1238 for Indoor Short Range and the Propagation Estimation Method Rec. P.1411 for Outdoor Short Range.

In ITU-R SG 5 WP5D, the name "IMT -2030" was agreed at the ITU-R SG 5 WP5D meeting in February 2022 as the name of the next generation IMT (commonly known as 6G). At the June meeting of the same year, the outline of the IMT for 2030 and beyond was agreed, and at the November meeting, a new report (ITU-R M. 2516, “Future Technology Trends”) was agreed. By this, the technology trends toward 2030 in which the realization of 6G is expected was arranged. Subsequently, at the June 2023 meeting, a new recommendation “Framework and overall objectives of the future development of IMT for 2030 and beyond” was agreed and published as recommendation ITU-R M. 2160. The recommendations provide a framework for future development and guidelines for overall goals toward the realization of IMT-2030. And at its 2024 meeting, SG 5 endorsed a new report, ITU-R M. 2541, “Technical feasibility of IMT in bands above 100 GHz”. In this report, many propagation measurement results above 100 GHz bands from Japan are contributed.

Currently, WP5D is considering the development of evaluation models for the following environments corresponding to 6 Usage Scenarios defined in Recommendation M. 2160. These tasks will be completed by the end of 2026.

- IC (Immersive Communication): Indoor Hotspot-IC、Dense Urban-IC、Rural-IC
- MC (Massive Communication): Urban Macro–MC
- HRLLC (Hyper Reliable and Low-Latency Communication): Urban Macro–HRLLC、Indoor Factory–HRLLC
- AIAC (AI and Communication): None
- ISAC (Integrated Sensing and communication): Indoor Factory–ISAC、[Indoor Hotspot–ISAC、Dense Urban–ISAC、Rural–ISAC、Urban Macro-ISAC
- UC (Ubiquitous Connectivity): Rural-UC

I-2. Recent Academic Activities

I-2.1. MmWave and Sub-THz Channel Modeling

The development of 6G networks focuses on achieving ultra-high data rates, extremely low latency, and global coverage. Since 2020, the ITU has led international 6G research, with the WRC expected to finalize spectrum regulations by 2027. 3GPP has begun standardization through Release 19. Future 6G systems are expected to utilize spectrum beyond the mmWave bands, including the sub-terahertz range (100–300 GHz), such as the D-band and G-band, to support high-speed communication. In line with global technological trends, Japanese academic research institutions and universities are actively conducting extensive investigations into mmWave and sub-THz communications. Channel modeling is a fundamental prerequisite for 6G system design and performance evaluation serving as the foundation for system-level simulations, performance benchmarking, and optimization of physical layer technologies.

Beyond 5G/6G is expected to become the foundational infrastructure for future industrial and societal activities, with global applicability. The National Institute of Information and Communications Technology (NICT) established the Information and Communications Research and Development Fund in 2022 to support long-term R&D and enhance Japan’s international competitiveness, promoting and encouraging research in the mmWave and sub-THz band to facilitate the smooth implementation of beyond 5G/6G networks. Regarding channel modeling research in the mmWave and sub-THz bands, recent academic efforts in Japan include the development of a quasi-deterministic site-specific channel modeling framework [9] and high-resolution spatiotemporal channel sounders for 24/60 GHz and 154/300 GHz measurements [10].

Further, measurement-based analysis of multi-beam MIMO capacity at 300 GHz demonstrates the feasibility of spatial multiplexing at this frequency, with further capacity enhancement enabled by the deployment of passive reflecting surfaces [11].

I-2.2. Radio Propagation for ISAC

Integrated sensing and communication (ISAC) is expected to be realized as one of the important roles in 6G. Therefore, a channel model for evaluating the performance of ISAC has been actively studied in academia. The examination of the channel model for ISAC mainly considers the radar cross section (RCS) characteristic of the target which is modeled by the deterministic modeling technique and the statistical modeling technique. The examination targets of RCS characteristics are mainly UAV, Robot, human and vehicle. In Japan, the IEICE held symposiums on research and development results in sensing, mainly in the field of antenna propagation, with the session titles of "Wireless Sensing Technology for the Realization of a Smart Society" at the IEICE Society Conference in 2020 and "Towards the Fusion of Sensing and Communication" at the IEICE General Conference in 2025, and many results were reported.

I-2.3. RIS-Based Propagation Modeling

The use of reconfigurable intelligent surfaces (RISs) has been gathering attention to improve various aspects of communication qualities such as coverage, channel capacity, power consumption, and physical security, and therefore, it is considered one of the key technologies for next-generation mobile communication systems. Since NTT Docomo's world first demonstration of throughput improvement using RIS in 2018 [12], various companies have reported on developments related to RIS and examination of propagation models.

KDDI research, Inc. examined the propagation via RIS in 28 GHz and 39 GHz bands using a newly developed dual-band and optically transparent RIS and commercial base station antenna mounted on a building [13]. Nihon Dengyo Kosaku, Co. Ltd. also examined in 5.6 GHz using a RIS, which switches the direction by the polarization of incident signal [14]. In each report, the received power P_r via RIS agreed with that calculated with the radar equation obtained by following equation [15]:

$$P_r = \frac{G_t G_r \lambda^2 \sigma}{(4\pi)^3 R_t^2 R_r^2} P_t,$$

where P_t is a transmitting power, G_t and G_r are the gain of transmitting and receiving antenna, R_t and R_r are the distance from transmitting and receiving antenna to the RIS, λ is wavelength, σ is the radar-cross section (RCS) of the RIS. Because the received power via RIS is determined with the RCS, various measurement results relating RCS of RIS are reported.

On the other hand, RCS is defined in the far-field region of RIS, and therefore, the radar equation is utilized in the far-field region. In practice, RIS is also utilized in the near-field region of RIS as reported in [16]. In the near-field region of the RIS, the received power via RIS is calculated with physical optics (PO)-based approach. In this approach, the received power is calculated by synthesizing the signal strength from each element of RIS as follows [15]:

$$P_r = P_t \frac{G_t G_r G s \lambda^2}{64\pi^3} \left| \Sigma_{n=1}^{N} \left(\frac{\sqrt{F_n}}{r_n^t r_n^r} \Gamma_n \exp\left(-\frac{2\pi}{\lambda} (r_n^t + r_n^r) \right) \right) \right|^2,$$

where N, G, and s are the number, gain, and area size of the element. F_n and Γ_n are the directivity and reflection (transmission) coefficient (phase and amplitude) of the n-th element. r_n^t and r_n^r are the distance between the n-th element and each transmitting and receiving element. Although PO based approach requires detailed information of reflecting element, it is utilized in both near-field and far-field region.

In each model, the received power via RIS is characterized by three components: the propagation between the transmitter and the RIS, the reflection (or transmission) performance of the RIS, and the propagation between the RIS and the receiver.

I-2.4. Radio Propagation for HAPS / NTN

At conferences such as the IEEE International Conference on Communications (ICC), the IEEE Global Communications Conference (GLOBECOM), the IEEE Wireless Communications and Networking Conference (WCNC), etc., have been actively discussing and studying the radio propagation of HAPS/NTN in recent years. Efforts are also being made toward international standardization of HAPS/NTN systems in cooperation with standardization bodies such as ITU-R (International Telecommunication Union, Radio Communication Sector). The main trends are as follows:

1. improvement of propagation model accuracy

   - **Influence of terrain and environment**: HAPS/NTN systems exhibit different propagation characteristics from conventional terrestrial communication systems due to their high altitude above the ground surface. In particular, it is important to accurately model the effects of topography and buildings in urban areas. Various methods have been proposed and discussed at the conference, including propagation analysis using electromagnetic simulations such as ray tracing and the FDTD method, construction of propagation models based on measured data, and propagation prediction using machine learning.
   - **Influence of meteorological conditions**: The influence of meteorological conditions such as rainfall, clouds, and refractive index variations in the atmosphere on

propagation cannot be ignored. The conference is analyzing the relationship between meteorological data and propagation characteristics, and developing propagation models that take meteorological conditions into account.

- Handling of moving objects: HAPS/NTN communications may be affected by Doppler effects and multipath fading differently than conventional communications. Propagation models that take into account the speed and travel path of the mobile terminal and the characteristic analysis of channel fluctuations are being developed at the conference.

2. interference evaluation and countermeasures

   - **Interference with terrestrial systems**: HAPS/NTN is likely to share frequencies with existing terrestrial communication systems, and mutual interference is a concern. At the conference, research is being conducted on simulation and measurement methods to accurately evaluate the amount of interference, frequency utilization techniques to suppress interference, and beamforming techniques.
   - **Interference between HAPS/NTNs**: When multiple HAPS/NTNs are in operation, interference between HAPS/NTNs is also an issue. Technologies to minimize interference by optimizing the placement and operation of HAPS/NTNs and signal processing techniques to avoid interference are being studied at the conference. 3.

3. performance evaluation and optimization

   - **Throughput and delay**: Methods to evaluate throughput and delay, which determine the communication performance of HAPS/NTNs, are being studied in consideration of propagation characteristics and system configuration.
   - **Coverage**: Antenna design, placement optimization, and beam control techniques are being studied to maximize coverage, the service area of HAPS/NTNs.
   - **QoS**: Techniques to provide Quality of Service (QoS) according to various application requirements, e.g., traffic control, resource allocation, scheduling, etc., are being studied.

I-2.5. Radio Propagation Emulation for Digital Twin

With the spread of autonomous driving, drones, IoT, and other technologies, wireless communication systems such as Beyond 5G/6G are becoming increasingly complex and sophisticated. As a result, the need for the rapid and flexible development and deployment of new wireless systems is increasing. However, testing in real-world environments is not only expensive and time-consuming, but also difficult to reproduce under the same conditions, making it difficult to perform accurate comparative verification.

As a means of solving such issues, the research and development of digital twin technology for wireless communication, which can emulate the behavior of wireless systems in virtual space, is becoming more active. Wireless digital twin technology is expected to be a technology that enables the verification of wireless systems at low cost and high precision with less restrict by testing in real environments.

I-2.5.1. Wireless Emulation for Digital Twin

Wireless emulation is a technology that reproduces the real-world radio environment in a virtual space to emulate the behavior of wireless communication systems. Conventional verification of wireless systems requires a large testing field or an expensive radio wave anechoic chamber, but wireless emulation makes it possible to reduce time and costs, set flexible testing conditions, and perform highly reproducible verification. The following systems are expected to be realized in the future.

- A large-scale verification test is conducted by building a 3D model that is faithful to the real environment and operating a virtual radio device within a virtual space.
- A radio system that uses a radio device that can be customized using software-defined radio is developed and evaluated under various conditions.

The National Institute of Information and Communications Technology (NICT) has developed a wireless emulator with the aim of evaluating wireless systems in real time under various conditions, as part of a research and development project by the Ministry of Internal Affairs and Communications. It supports wireless systems and frequencies, such as 5G and Wi-Fi, and can emulate up to 256 x 256 wireless links. Kyoto University and NICT conducted a multi-hop communication test using 10,000 wireless devices equipped with the Wi-SUN FAN communication standard for IoT using a wireless emulator.

I-2.5.2. Radio Propagation Emulation for Wireless Emulator

As described above, there are high expectations for wireless emulators, but in order to accurately verify them in an actual usage environment, it is essential to have a highly accurate radio propagation model. The wireless emulator developed by NICT, introduced above, uses a ray tracing method and also considers a channel generation method based on the 3GPP TR 38.901 [9] map-based hybrid channel model.

This method consists of stochastic clusters generated by path loss, Large Scaler Parameter (LSP), which represents time-space characteristics on macroscopic scales, and Small Scale Parameter (SSP), which represents multipath characteristics on microscopic scales, as well as deterministic clusters generated by ray tracing, and the channel impulse response is generated based on the Cluster Delay Line (CDL) parameters generated from these [17]. In addition, to improve the accuracy of the generated channel, various methods have been proposed to construct a model that expresses site-specific path loss and LSPs using machine learning [18].

As described above, there are high expectations for wireless emulators, but in order to accurately verify them in an actual usage environment, it is essential to have a highly accurate radio propagation model. The wireless emulator developed by NICT, introduced above, uses two approaches for channel emulation; the ray tracing method and the stochastic model based on the 3GPP TR 38.901 [9] map-based hybrid channel model.

In ray tracing, computational load tends to increase in environments with many multipaths. Therefore, parameter optimization suitable for indoor and outdoor environments, such as factories and offices, has been proposed as solutions to achieve the required accuracy with the necessary computing resources [19][20].

On the other hand, the stochastic method consists of stochastic clusters generated by path loss, Large Scaler Parameter (LSP), which represents time-space characteristics on macroscopic scales, and Small Scale Parameter (SSP), which represents multipath characteristics on microscopic scales, as well as deterministic clusters generated by ray tracing, and the channel impulse response is generated based on the Cluster Delay Line (CDL) parameters generated from these [21]. In addition, to improve the accuracy of the generated channel, various methods have been proposed to construct a model that expresses site-specific path loss and LSPs using machine learning [22].

Channel generation is performed for each grid in the above approaches. However, since mobile terminals move continuously, a mechanism for interpolating discretely generated channels has been proposed [23].

Wireless emulator emulates radio propagation by integrating these technologies.

I-2.6. Radio Propagation Simulation for CPS

With 6G in the 2030s, physical space and cyberspace will converge, and AI and others will be able to reproduce the real world on cyberspace (digital twin) and discover "future predictions" and "new knowledge" by emulating it beyond the constraints of the real world. Utilizing this in real-world services will enable the provision of various values and solutions. For this purpose, large-capacity, low-latency transmission of sensing information and other information from physical space and feedback from cyberspace to physical space through high-reliability, low-latency transmission of control signals are assumed. Ultra-high-performance wireless communications are indispensable for realizing advanced cyber-physical fusion (CPS).

Dynamic feedback from cyberspace to physical space requires real-time propagation and transmission emulation. In the field of propagation technology, various estimation techniques that are much faster and more accurate than conventional ray tracing methods are being studied for this real-time propagation emulation.

REFERENCE

[1] RP-234018, New SID: Study on channel modelling enhancements for 7-24GHz for NR, Dec. 2023.

[2] 3GPP R1-2401937, “Summary #3 on ISAC channel modelling,” TSG RAN WG1 #116, Athens, Greece, March 2024.

[3] 3GPP R1-2403716, “Summary #5 on ISAC channel modelling,” TSG RAN WG1 #116bis, Changsha, China, April 2024.

[4] 3GPP R1-2404636, “Summary #4 on ISAC channel modelling,” TSG RAN WG1 #117, Fukuoka, Japan, May 2024.

[5] 3GPP R1-2409280, “Summary #4 on ISAC channel modelling,” TSG RAN WG1 #118bis, Hefei, China, Oct. 2024.

[6] 3GPP R1-2410014, “Summary #4 on ISAC channel modelling,” TSG RAN WG1 #119, Orlando, US, Nov. 2024.

[7] 3GPP R1-241041 (NTT DOCOMO, INC.), “Discussion on ISAC Channel Modelling,” TSG RAN WG1 #119, Orlando, US, Nov. 2024.

[8] 3GPP R1-2501002, “Summary #4 on ISAC channel modelling,” TSG RAN WG1 #120, Athens, Greece, Feb. 2025.

[9] 3GPP TR 38.901 (V17.0.0): Study on channel model for frequencies from 0.5 to 100 GHz (Release 17), 2022.

[10] M. Kim, A. Ghosh, R. Takahashi and K. Shibata, "Indoor Channel Measurement at 300 GHz and Comparison of Signal Propagation With 60 GHz," *IEEE Access*, vol. 11, pp. 124040-124054, 2023

[11] M. Mao et al., “MIMO Channel Capacity Measurement in Open Square Hot Spot Access Scenarios at 300 GHz,” *IEEE Wireless Commun. Lett.*, Vol. 13, No. 9, pp. 2576-2580, Sept. 2024.

[12] https://www.docomo.ne.jp/info/news_release/2018/12/03_00.html.

[13] H. Matsuno, T. Ohto and T. Hayashi, "Development of Intelligent Reflecting Surfaces for Mobile Communication Systems," 2022 IEEE International Workshop on Electromagnetics: Applications and Student Innovation Competition (iWEM), Narashino, Japan, 2022, pp. 5-6, doi: 10.1109/iWEM52897.2022.9993561.

[14] M. Yoshino and D. Sugimura, "Intelligent Reflecting Surface Effect by Switching ±45° Incident Polarization in Outdoor Environment," in IEICE Communications Express, vol. 14, no. 1, pp. 26-29, January 2025, doi: 10.23919/comex.2024XBL0138.

[15] W. Tang et al., “Wireless Communications With Reconfigurable Intelligent Surface: Path Loss Modeling and Experimental Measurement,” in IEEE Transactions on Wireless Communications, vol. 20, no. 1, pp. 421-439, Jan. 2021, doi: 10.1109/TWC.2020.3024887.

[16] K. Goto, S. Suyama, T. Yamada, K. Arai and O. Kagaya, "Experimental Trials with

Combination of Multiple Transmissive Metasurfaces and Beamforming for mmW Coverage Enhancement," 2023 IEEE 98th Vehicular Technology Conference (VTC2023-Fall), Hong Kong, Hong Kong, 2023, pp. 1-5, doi: 10.1109/VTC2023-Fall60731.2023.10333724.

[17] H. Tsukada, N. Suzuki, B. Bag, R. Takahashi and M. Kim, "Millimeter-Wave Urban Cellular Channel Characterization and Recipe for High-Precision Site-Specific Channel Simulation," in *IEEE Transactions on Vehicular Technology*, vol. 74, no. 3, pp. 3598-3612, March 2025, doi: 10.1109/TVT.2024.3492719.

[18] T. Nagao and T. Hayashi, "A Study on Path Loss Modeling using ResNet and Pre-Training with Free Space Path Loss," 2022 IEEE 33rd Annual International Symposium on Personal, Indoor and Mobile Radio Communications (PIMRC), Kyoto, Japan, 2022.

[19] M. Hirose, T. Imai, S. Wu, S. Iwasaki, G. S. Ching and Y. Kishiki, "Ray Tracing Parameter Optimization System in Mobile Radio Propagation Prediction," *2022 IEEE 33rd Annual International Symposium on Personal, Indoor and Mobile Radio Communications (PIMRC)*, Kyoto, Japan, 2022, pp. 01-05.

[20] A. Haniz *et al.*, "Multipath Parameter Optimization for Improving Accuracy of Ray-Tracing-based Received Power Prediction in Industrial Environments," in *IEEE Transactions on Vehicular Technology.*

[21] H. Tsukada, N. Suzuki, B. Bag, R. Takahashi and M. Kim, "Millimeter-Wave Urban Cellular Channel Characterization and Recipe for High-Precision Site-Specific Channel Simulation," in *IEEE Transactions on Vehicular Technology*, vol. 74, no. 3, pp. 3598-3612, March 2025, doi: 10.1109/TVT.2024.3492719.

[22] T. Nagao and T. Hayashi, "A Study on Path Loss Modeling using ResNet and Pre-Training with Free Space Path Loss," 2022 IEEE 33rd Annual International Symposium on Personal, Indoor and Mobile Radio Communications (PIMRC), Kyoto, Japan, 2022.

[23] N. Keerativoranan, K. Saito and J. -I. Takada, "Grid-Based Channel Modeling Technique for Scenario-Specific Wireless Channel Emulator Based on Path Parameters Interpolation," in *IEEE Open Journal of the Communications Society*, vol. 5, pp. 1724-1739, 2024.

II. Recent Activities of Radio Propagation in Japan

This chapter presents initiatives related to radio propagation in Japan. II-1, "Measurement," reports analysis results of propagation characteristics based on measurement campaigns. II-2, "Simulation," reports the application of radio propagation simulation technologies and machine learning.

II-1. Measurement

II-1.1. Indoor Propagation Channel Measurements in 160 GHz

Nobuaki Kuno, Koshiro Kitao, Takahiro Tomie, Satoshi Suyama
NTT DOCOMO, INC.

***Abstract*— One of the requirements of the 6th generation mobile communication system (6G) is the high-capacity communication exceeding 100 Gbps. To realize this requirement, the use of sub-terahertz band and terahertz band of 100 GHz or more which can use very wide band is considered. In order to utilize new frequency bands, it is necessary to clarify the radio propagation characteristics of each usage scenario in those frequency bands for area design and system design. This article describes the measurement and analysis results of the spatiotemporal characteristics of the delay time in indoor office environment in the 160 GHz band.**

II-1.1.1. Introduction

The 5th generation mobile communication system (5G) will be launched as a commercial service in 2020, and various organizations are studying the realization of the 6th generation mobile communication system (6G) in the 2030s. The requirements for 6G include ultra-high speeds exceeding 100 Gbps and large-capacity communications 10 times faster than 5G [1]. In order to realize this ultrahigh-speed and large-capacity communication, the terahertz band above the 92 GHz band, which has a wider bandwidth than 5G, is expected to be used, and various studies have been initiated for its application [2-6]. The 2019 World Radiocommunication Conference (WRC-19) has established as an action item the study of frequency identification for land mobile and fixed telecommunications operations in the 275-450 GHz band [7]. In addition, Working Party 5D (WP5D) of the International Telecommunication Union Radiocommunication Sector (ITU-R) has started to study new propagation channel models in the 92-300 GHz band for 6G system evaluation [8-11]. These propagation channel models are used for system design, including feasibility evaluations in real-world environments. In order to construct a propagation channel model for the sub-THz band, it is essential to understand the highly accurate propagation channel characteristics in this frequency band.

The sub-THz band has an even shorter wavelength than the 28 GHz band used in 5G. Therefore, the arrival of radio waves is affected by the surrounding human body and surrounding structures, and the arrival conditions of radio waves also change significantly [2], [3]. The arrival conditions of radio waves are affected by the surrounding human body and structures, etc., and change significantly. Therefore, in order to construct a propagation channel model for the sub-THz band, it is necessary to elucidate the effects of propagation loss and shielding. The authors have investigated propagation channel characteristics in the 160 GHz and 300 GHz bands by measuring angular profile characteristics in an indoor conference room environment [12]. In this paper, the delay characteristics of the 160 GHz band in an indoor office environment were measured, and the measurement contents and results are presented.

II-1.1.2. Measurement environment and method

The measurements were performed in a room in the NTT DOCOMO R&D Center. The measurement environment is shown in Fig. II-1. It is an office environment with wooden-topped desks placed at regular intervals and displays lined up on the desks. The upper and left sides of Fig. II-1 are glass windows, and the lower and right sides are concrete walls. The three doors at the bottom of the figure are the entrances. The multiple separated spaces near the entrances and the spaces at the upper right and left are conference rooms separated by aluminum blinds and glass, with desks and chairs inside. The overall size of the room is approximately 50 m (right and left), 16 m (up and down), and 2.7 m (height) as shown in the figure.

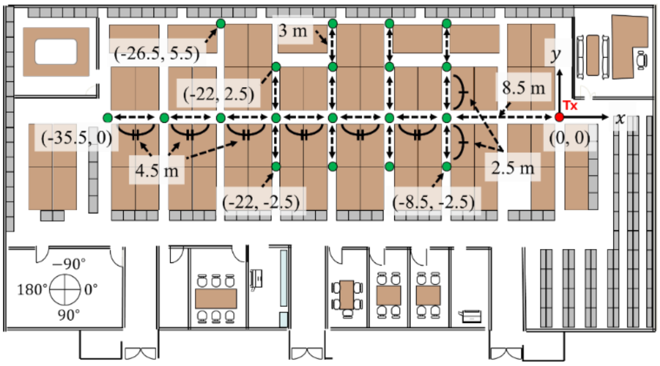

Fig. II-1. Measurement environment.

Table. II-1 shows the measurement parameters. An OFDM signal with a center frequency of 160 GHz and a bandwidth of 2 GHz was used for the measurements. An omni-antenna was used for the transmitter (Tx) and a horn antenna with a gain of about 25 dBi was used for the receiver (Rx). This allows measurement with a delay resolution of 0.5 ns. The resolution is about 15 cm in distance. The Tx and Rx antennas were measured at a height of 2 m and 1 m, respectively, assuming an access point near the ceiling and a tabletop wireless system. The position of the antennas in relation to the floor and ceiling is shown in Fig. II-2. The distances between the Tx and Rx antennas ranged from 8.5 m to 35.5 m. In addition, measurements were taken by varying the elevation angle of the Rx antenna to 0, 10, and 20 degrees to compare differences in the effects of reflections from the ceiling and other factors.

Table. II-1. Evaluation Parameters

Parameter	Value
Center frequency	160 GHz
Transmitting signal	OFDM
Bandwidth	2 GHz
Tx antenna	Omnidirectional antenna
Rx antenna	Horn antenna
Tx antenna height	2 m
Rx antenna height	1 m
Delay resolution	0.5 ns
Maximum delay	128 ns

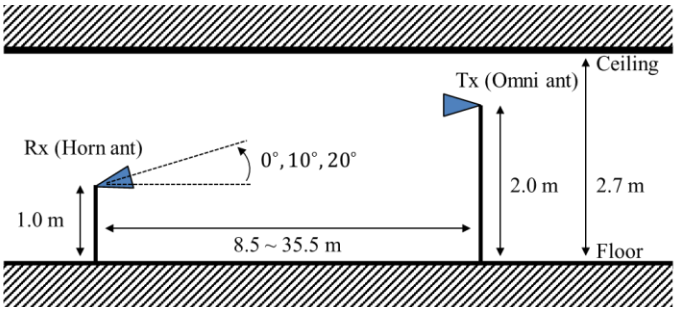

Fig. II-2. Relation between Tx and Rx antenna locations.

The delay profile was measured by pointing the Rx antenna in the right direction in Fig. II-1, taking that direction as 0 degree, and rotating it 360 degrees counterclockwise horizontally from there. Since it depends on the surrounding multipath, it is expected that the measurement results will vary depending on the location of the antennas. Therefore, as shown in Fig. II-1 Tx antennas were placed at the edge of the room, and Rx antennas were measured at 19 points. Here, of the 19 points, 7 measurement points are at $Y = 0$, which is on the LoS (Line-of-Sight) from Tx, and the remaining 12 points ($Y \neq 0$) are at the NLoS (Non-Line-of-Sight). The angular profiles were calculated by power-multiplying the paths for each horizontal angle.

II-1.1.3. Measurement Results

Fig. II-3 shows the measured delay profile at the point (-8.5, 0), which is the closest LoS measurement point from Tx. The received power is normalized to the highest value among the measured data. The distance between the Tx and Rx antennas is 8.5 m, and the difference in antenna height is 1 m. Therefore, the direction of the Tx antenna from the Rx antenna is at an elevation angle of 11.7 degree, and a 0 dB signal was observed at the nearest elevation angle of 10 degree in Fig. II-3 (b). The strongest paths were observed at a horizontal angle of 0 degree and a delay time of about 28.3 ns in the direction of the Tx antenna. In Fig. II-3 (a) and Fig. II-3 (b), strong radio waves were observed at a horizontal angle of ±50 degree and a delay time of around 40 ns. In Fig. II-3 (c), the same radio waves and those at a horizontal angle of 0 degree and a delay time of approximately 28.3 ns were both observed to be weak. This may be due to the fact that the direct wave and the reflected wave near the ceiling are out of the beamwidth of the Rx antenna.

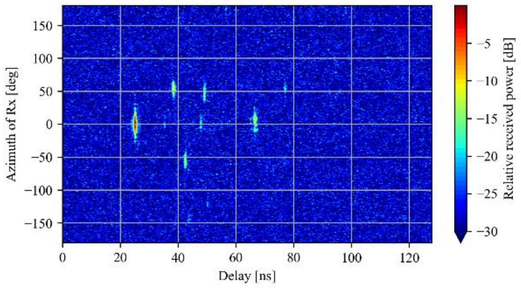

(a) Measurement results at an elevation angle of 0 degree.

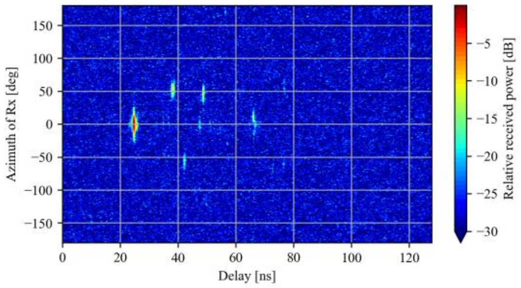

(b) Measurement results at an elevation angle of 10 degree.

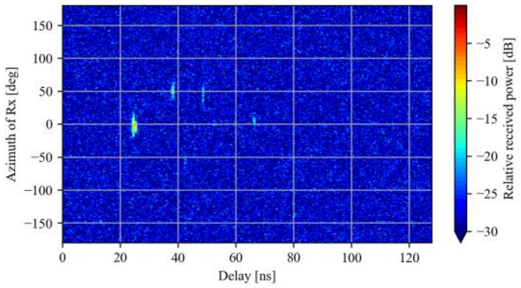

(c) Measurement results at an elevation angle of 20 degree.

Fig. II-3. Delay profile measurement result at point (-8.5, 0).

Fig. II-4 shows the measured delay profiles at the point (-17.5, 0) as more distant LoS point. Same as Fig. II-3, Fig. II-4 is also a point on the $Y = 0$ line of sight, with the distance between Tx and Rx doubled to 17.5 m. And it was confirmed that the direct wave had the strongest received power from 17.5 m to around 56.6 ns of delay time. Furthermore, for the paths of reflections and diffractions from the surroundings, it was confirmed that they were received around ±30 degrees, unlike Figure 1, where they were around ±50 degrees. This is thought to be due to the fact that the distance between Tx and Rx has increased, resulting in an obtuse angle with objects such as desks near the line of sight and a narrower angular spread as seen from Rx.

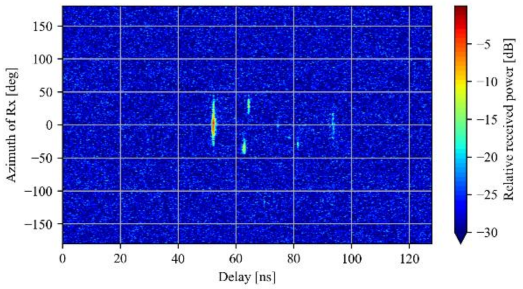

Fig. II-4. Delay measurement results for an elevation angle of 0 degrees at (-17.5, 0).

Fig. II-5 shows the extracted results of the delay profile measurements at 0° elevation and horizontal angles in Fig. II-3 (a). As in Fig. II-3 (a), a strong radio wave, which is considered to be a direct wave, was observed at a delay time of approximately 28.3 ns. In addition, a slightly stronger radio wave of about -10 dB was observed at a delay time of less than 70 ns. Compared to Fig. Fig. II-3 (b) and Fig. II-3 (c), the strongest signals were received at an elevation angle of 0°, and the delay time suggests that the waves were reflected once on the ceiling and once on the floor.

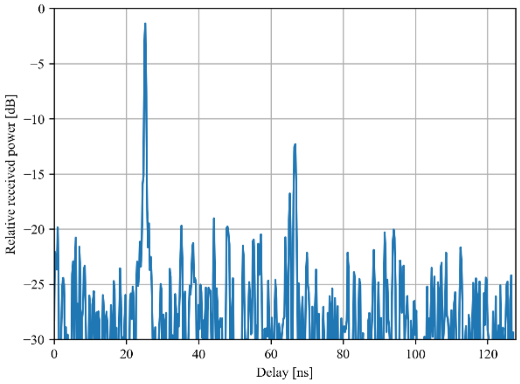

Fig. II-5. Delay measurement results for horizontal and vertical angles of 0 degrees at point (-8.5, 0).

Fig. II-6 shows the CDF of the delay spread calculated for 7 LoS points with $Y = 0$ and 12 NLoS points with $Y \pm 0$. The median of CDF for both LoS and NLoS points was approximately 5.5 ns, and the trend was similar. This indicates that the LoS and NLoS points are similar in this measurement environment. This is thought to indicate that reflected and diffracted waves arrived from a certain range for both the LoS and NLoS points in this measurement environment.

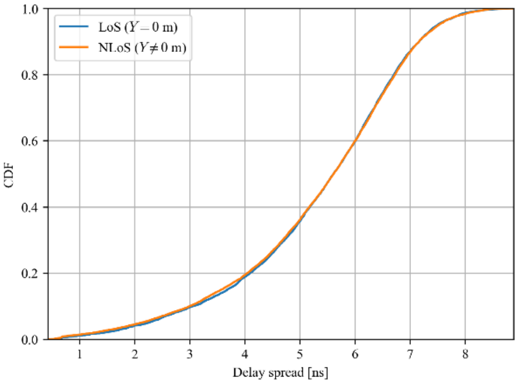

Fig. II-6. CDF of delayed spread.

II-1.1.4. Conclusion

This paper described the measurement method and results of the delay profile in the 160 GHz band, one of the frequencies being considered for use in 6G, in an indoor office environment. By using a 2-GHz OFDM signal, we were able to confirm reflected waves on the ceiling, reflected waves between the ceiling and floor, and diffracted waves from desks and other objects at the NLoS point, in addition to direct waves. Further evaluation will be conducted in the future to develop a propagation channel model.

REFERENCE

[1] NTT DOCOMO, INC., “White Paper 5G Evolution and 6G,” Jan. 2020.

[2] M. Inomata, W. Yamada, N. Kuno, M. Sasaki, K. Kitao, M. Nakamura, H. Ishikawa, and Y. Oda, “Terahertz Propagation Characteristics for 6G Mobile Communication Systems,” in *2021 15th European Conference on Antennas and Propagation (EuCAP)*, 2021, pp. 1–5.

[3] T. S. Rappaport, Y. Xing, O. Kanhere, S. Ju, A. Madanayake, S. Mandal, A. Alkhateeb, and G. C. Trichopoulos, “Wireless Communications and Applications Above 100 GHz: Opportunities and Challenges for 6G and Beyond,” *IEEE Access*, vol. 7, pp. 78 729–78 757, 2019.

[4] K. Guan, B. Peng, D. He, J. M. Eckhardt, H. Yi, S. Rey, B. Ai, Z. Zhong, and T. K¨urner, “Channel Sounding and Ray Tracing for Intrawagon Scenario at mmWave and Sub-mmWave Bands,” *IEEE Transactions on Antennas and Propagation*, vol. 69, no. 2, pp. 1007–1019, 2021.

[5] Y. Chen, Y. Li, C. Han, Z. Yu, and G. Wang, “Channel Measurement and Ray-Tracing-Statistical Hybrid Modeling for Low-Terahertz Indoor Communications,”

IEEE Transactions on Wireless Communications, vol. 20, no. 12, pp. 8163–8176, 2021.

[6] S. Ju, Y. Xing, O. Kanhere, and T. S. Rappaport, “Millimeter Wave and Sub-Terahertz Spatial Statistical Channel Model for an Indoor Office Building,” *IEEE Journal on Selected Areas in Communications*, vol. 39, no. 6, pp. 1561–1575, 2021.

[7] WRC 2019, “WRC 2019 Agenda Item Details.”

[8] ITU-R, “Work plan, timeline, process and deliverables for the future development of IMT,” *ITU-R WP5D*, March 2022.

[9] ITU-R, “Draft working document towards a preliminary draft new Report ITU-R M.[IMT. ABOVE 100 GHz],” *ITU-R WP5D*, March 2022.

[10] ITU-R, “Updated Annex 5 of the draft working document towards a PDN Report ITU-R M.[IMT.Above 100 GHz],” *ITU-R WP5D*, June 2022.

[11] ITU-R, “Technical feasibility of IMT in bands above 100 GHz,” *ITU-R WP5D*, October 2022.

[12] M. Nakamura, S. Suyama, K. Kitao, T. Tomie, M. Inomata, W. Yamada, N. Kuno, and M. Sasaki, “Measurement of Multipath Waves at 160 GHz and 300 GHz in an Indoor Conference Room,” in *2023 17th European Conference on Antennas and Propagation (EuCAP)*, 2023, pp. 1–5.

II-1.2. 300GHz Band Propagation Loss in the Vicinity of the Human Body

Kazuki Takezawa, Takahiro Hayashi
KDDI Research, Inc.

***Abstract*— The use of the THz band is being considered for ultra-high-speed and high-capacity communications for Beyond 5G and 6G. As one of the use cases, the virtualized terminal has been proposed to improve the communication speed of the uplink by applying it to the connection between peripheral devices such as wearable devices and user equipment (UE). To evaluate the wireless performance of this technology, it is necessary to clarify the radio propagation characteristics in the vicinity of the human body and to construct a propagation path model. The authors measured diffraction losses in the 300 GHz band using a human phantom in an upright position and showed that although the human body can be approximated by two screens and estimated accurately by the Double Isolated Edge (DIE) model, verification using an actual human body limits this accuracy and may be influenced by clothing. The results showed that this is not the case. This article introduces a propagation loss estimation method that takes this effect into account and shows that the RMSE (Root Mean Square Error) can be estimated with a high accuracy of approximately 8.35 dB by using actual measurements from experiments assuming walking movements.**

II-1.2.1. Introduction

For the Beyond 5G and 6G, realization of ultrahigh-speed and large-capacity communication exceeding 100 Gbps is expected, and the use of the THz band, which is expected to secure ultrawide bandwidth, is being considered for this purpose [1]. Various studies and proposals have been made regarding the use cases of these frequency bands, including communication within data centers and kiosk stations [1]. Among them, we have proposed a virtualized terminal technology that wirelessly connects peripheral devices such as wearable devices to the UE in the THz band and connects to the base station by converting to a relatively lower frequency, such as the millimeter wave band at the peripheral device [1,2]. In this technology, the UE and peripheral devices cooperate to virtually bundle each device's antennas, thereby eliminating the physical constraints of conventional UEs, such as transmission power and the number of antennas, and aiming to improve the communication speed of the uplink. In this context, to evaluate the wireless performance of this technology and optimize the number and position of peripheral devices, transmission power, antenna patterns, etc., to achieve the target throughput, it is necessary to simulate the variation in received power due to propagation loss and fading changes for each posture. For this purpose, it is necessary to clarify the radio wave propagation characteristics, especially in the THz band in the vicinity of the human body, and to construct a propagation channel model.

In this section, we describe the estimation method for diffraction loss of the human body that we have devised. Furthermore, as an example, we state that for the receiving points in the NLoS region, where the diffraction path is dominant, measurements taken using a human body in a walking posture can be estimated with an accuracy of approximately 8.35 dB RMSE.

II-1.2.2. Model correction term considering the influence of clothing

In the future, it is necessary to construct a model that adapts to various clothing scenarios, and for this purpose, consideration of a model based on physical interpretation is essential. Therefore, in this Section, we propose a diffraction loss model that considers the influence of clothing via the FDTD simulation and the measurement values reported in [3]. This model is based on the DIE model, which can accurately estimate the condition without clothing and adds a term to correct for the influence of clothing. As revealed in the simulation in Section 2, the newly occurring paths due to clothing are diffraction on the clothing surface and reflection inside the clothing. In [4], it was reported that scattering occurs due to clothing, and the angle of arrival tends to spread three-dimensionally. However, in this study, based on the considerations reported previously [3], we generate a correction term by fitting θ_{t+r} and $cos\theta_{t-r}$, as shown in Fig. 1, to represent this phenomenon simply. The diffraction loss model with this correction term is as follows in Equation (1).

$$PL'_{Diff} = PL_{Diff} - 23.87 \times \theta_{t+r} - 9.55 \times cos\theta_{t-r} \qquad (1)$$

The parametersθ_{t+r} andθ_{t-r} indicate the angles formed by the transmission point (Tx), receiving point (Rx), and the virtual diffraction point, using the 3D model of the human body including clothing as shown in Fig. II-7.

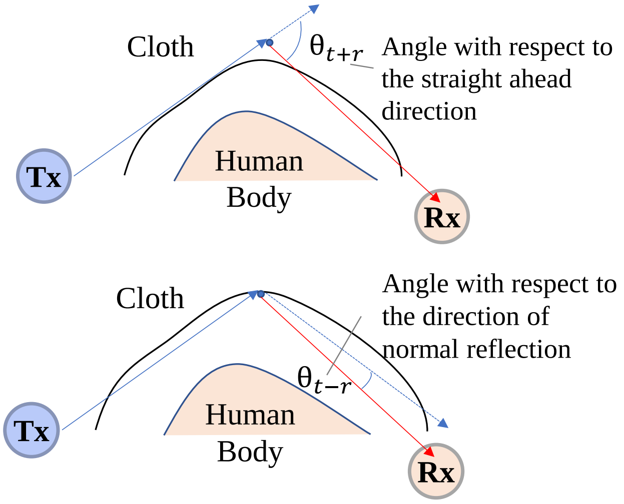

Fig. II-7. Parameters for the diffraction loss correction term when clothing is included

Note that PL_{Diff} is the diffraction loss obtained by approximating the human body as a double screen and using the DIE model[P.526]using parameters in Fig. II-8.

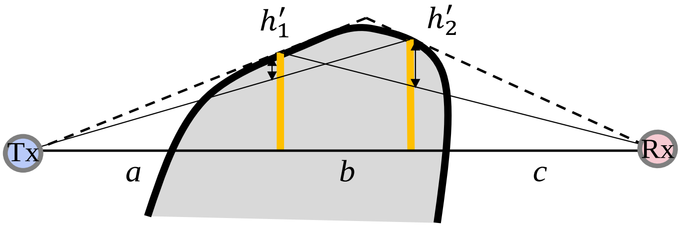

Fig. II-8. Parameters of the diffraction loss model for the human body.

II-1.2.3. Evaluation via measurements on real human bodies

In this section, we report the evaluation of the diffraction loss model with the added correction term, which uses measurement results from real human bodies. As shown in Fig. II-9 this measurement was conducted by assuming a walking posture, setting Tx at the position of the right hand, and placing Rx at a comprehensive position 7 cm from the surface of the human body, thereby extracting only the conditions where the diffraction path is dominant.

Fig. II-10 shows the measured values from which only the NLoS region was extracted and the evaluation results obtained via these measurements. The horizontal axis represents the distance between the antennas, and the vertical axis represents the propagation loss. The black dots are the measurement values, the green rectangles are the values estimated via the method previously proposed by the authors [5], and the red dots are the estimated values with the correction term added to the calculation of the power of the diffraction path. For comparison with previous studies, the KED estimates are plotted as gray triangles. Note that the parameters used for this estimation were extracted from a 3D model of a clothed human body.

The estimated values indicated in green tend to overestimate the propagation loss, whereas the estimated values with the correction term added tend to estimate well. Table. II-2 shows the accuracy of these estimates, where the RMSE was significantly improved from 14.81 dB to 8.35 dB in the NLoS region. In addition, the proposed method with the correction term produced more accurate results than the estimation with conventional KED; this is likely because the correction term was able to properly compensate for the influence of clothing on propagation loss.

In the future, we will study parameters and their extraction methods to further improve the accuracy of this estimation. We also study the correction terms and comparative evaluations for conditions different from those of the clothing used in this experiment.

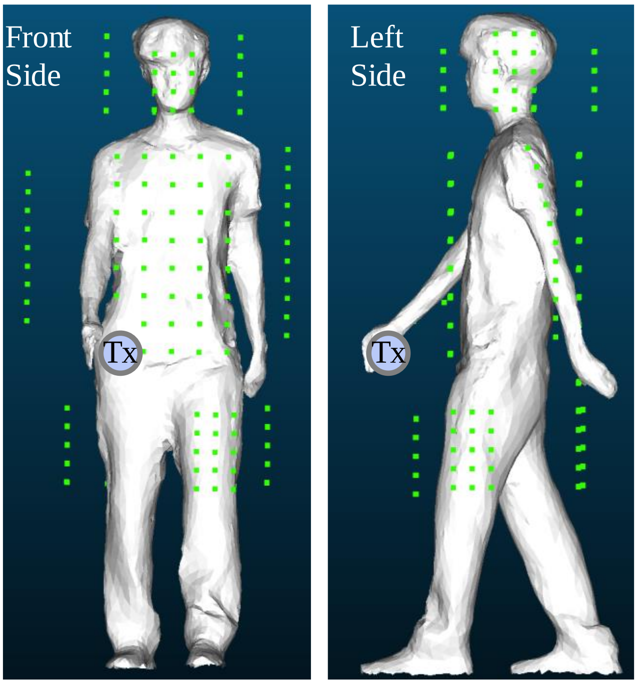

Fig. II-9. Evaluation using measurement results from a real human body

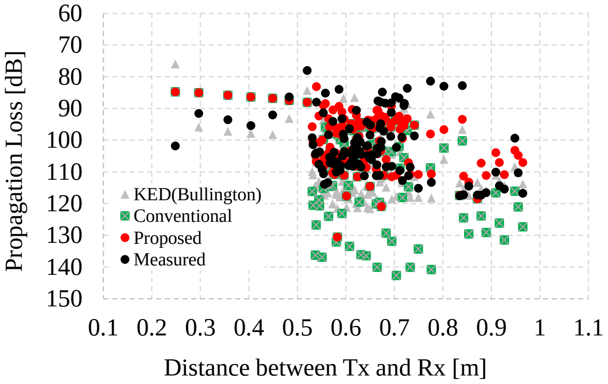

Fig. II-10. Evaluation using measurement results from a real human body

Table. II-2. Estimation accuracy of measurement by real human body (RMSE)

	Proposed	Conventional	KED
NLoS	8.35	14.81	11.17

Acknowledgements

These research results were obtained from the commissioned research (JPJ012368C00401) by National Institute of Information and Communications Technology (NICT), Japan.

REFERENCE

[1] W. Jiang, B. Han, M. A. Habibi and H. D. Schotten, "The Road Towards 6G: A Comprehensive Survey," in IEEE Open Journal of the Communications Society, vol. 2, pp. 334-366, 2021.

[2] KDDI Corporation, KDDI Research, inc., "Beyond 5G/6G white paper," Mar. 2021.

[3] K. Takezawa, Satoshi Ito, Tatsuya Nagao "A Study on 300GHz Band Propagation Loss Modeling in the Vicinity of the Human Body Considering the Effect of Clothing",IEEE Consumer Communications & Networking Conference (CCNC),2025, "in press"

[4] S. Takagi and A. Hirata, "Effect of Gap between Arm and Torso and Clothing on Human Body Shadowing at 300 GHz," 2023 IEEE International Symposium On Antennas And Propagation (ISAP), 2023

[5] K. Takezawa, T. Nagao and T. Hayashi, "300 GHz propagation loss estimation method for BAN assuming walking behavior" 2024 IEEE 99th Vehicular Technology Conference (VTC2024-Spring), 2024.

II-1.3. 300GHz Band Propagation Characteristics in the Indoor and Outdoor Environment

Satoshi Ito, Takahiro Hayashi
KDDI Research, Inc.

***Abstract*—The utilization of the terahertz bands is expected for realization of 6G systems. In this article, we provide the results of propagation experiments conducted at the 300-GHz band in both indoor and outdoor environments, including NLOS conditions. We report the obtained angle of arrival characteristics. Furthermore, on the basis of the arrival wave distribution obtained from the angle of arrival measurements, we analyze and describe the propagation mechanisms of the 300-GHz band in NLOS regions.**

II-1.3.1. Introduction

Towards 6G, one of the key technological elements for achieving ultrahigh-speed data transmission is the utilization of the terahertz (THz) band, which offers a wider bandwidth than the millimeter-wave band currently employed commercially in 5G. The ThoR project [1] has focused on exploring the applications of high-speed, high-capacity wireless networks using the THz band for constructing back- and fronthaul networks to connect mobile communication system base stations. Additionally, the use of the THz band as a relay link in conjunction with millimeter-wave bands in virtualized terminals is being considered [2]. However, to evaluate the feasibility and performance of these utilization methods, a propagation model applicable to the THz band is essential.

According to a survey paper on propagation characteristics above 100 GHz [3], reports on the propagation characteristics of the 300 GHz band are fewer than those for the 100-GHz band, particularly for non-line-of-sight (NLOS) conditions, which are even fewer outdoors than indoors. Papers reporting the NLOS characteristics of the 300-GHz band since the survey paper [3] include [4][5] for outdoor environments and [6] for indoor environments, indicating a need for more measurement results in various environments to statistically analyze the characteristics of the 300-GHz band, including under NLOS conditions. Therefore, we report the analysis results for the measured angle of arrival (AoA) characteristics of the 300-GHz band, primarily focusing on the less frequently reported NLOS conditions in both outdoor and indoor environments.

II-1.3.2. Measurement Environments

The measurement campaigns were conducted in both outdoor and indoor environments. First, outdoor measurement campaigns were conducted on roads and in parking lots surrounding an approximately 20-m-long building, as shown in Fig. II-11. The measurement environment was divided into an NLOS area obstructed by buildings, a vegetation NLOS (VNLOS) area obstructed by vegetation, and a LOS area.

Additionally, AoAs were measured at representative points in the NLOS and VNLOS areas, specifically at Rx1 and Rx2, which are obstructed by the building, and at Rx3, which is obstructed by vegetation.

Indoor measurement campaigns were conducted in the corridor inside a building. The measurement environment consists of a corridor in the basement of the building without windows and is divided into LOS and NLOS areas involving a single turn. Additionally, AoAs were measured at representative points in the NLOS area, specifically at Rx1 and Rx2, which occur immediately after the transition from the LOS area to the NLOS area. For additional details on the measurement specifications, the reader is referred to [7].

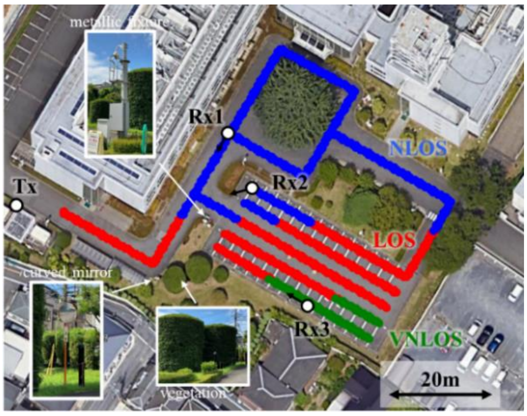

Fig. II-11. Top view of the measured outdoor environment[7].

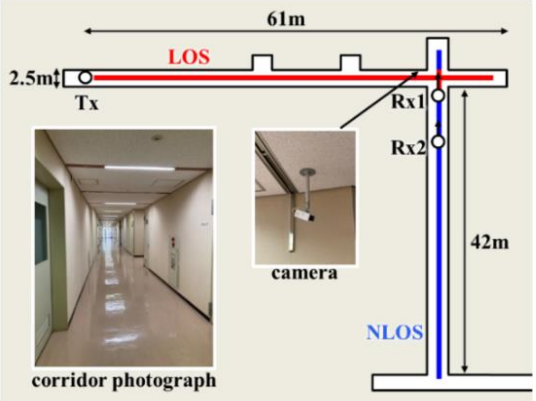

Fig. II-12. Top view of the measured indoor environment[7].

II-1.3.3. Measurement Results

II-1.3.3.1. Outdoor Environments

The AoA values at Rx1 to Rx3 are described. At Rx1, as in Fig. II-13 (a), weak diffracted waves from the building edge were noted due to a high diffraction angle, with wave A dominating. This wave reflected and scattered from a metallic mirror and trees, then off the ground. Reflections from the mirror and trees at B, scattering from vegetation at C, and a pole at D were observed. Waves from E were secondary reflections from building walls, indicating that under NLOS, reflections and scattering dominate over diffraction near building edges. At Rx2, as in Fig. II-13 (b), with a lower diffraction angle, wave A remained strong, supplemented by waves from metallic fixtures at B and C and visible trees. Reflected and scattered waves from fixtures and trees significantly contributed to power. Finally, at Rx3, as in Fig. II-13 (c), waves from A, B, and E passing trees were observed, but none through trees, due to density and loss from branches and foliage, highlighting the need to understand tree characteristics. Other waves included reflections from a lamp post at C and building edges at E and F, and scattering from trees at G. Results show that in the 300-GHz band, diffraction loss rises with angle, not aiding received power, while under NLOS and VNLOS, main paths are reflected and scattered waves from fixtures and trees, and low-angle diffracted waves from building edges.

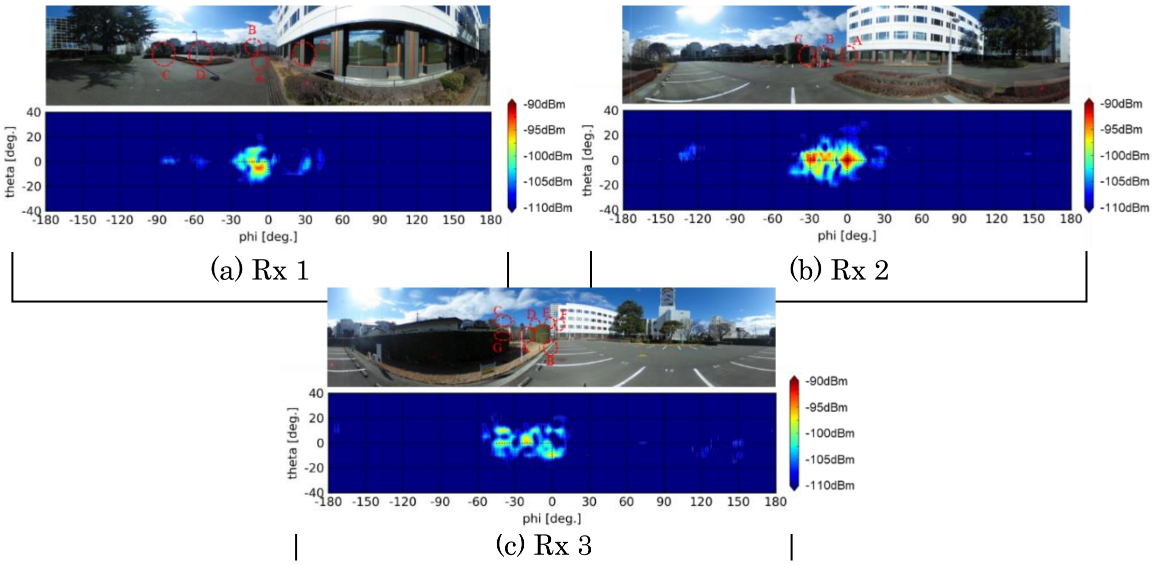

(a) Rx 1

(b) Rx 2

(c) Rx 3

Fig. II-13. AoA distributions with photographs obtained at each outdoor Rx [7].

II-1.3.3.2. Indoor Environments

We describe the AoA values at Rx1 and Rx2. At Rx1 (Fig. II-14 (a)), weak diffracted waves were noted from deep angles at F, while strong waves arrived from A and C at corridor edges with less acute angles, similar to outdoor observations. Scattered waves from the surveillance camera at B highlight that even small metal fittings can significantly contribute to received power. Waves at D and E were scattered from metal door parts on corridor sidewalls.

At Rx2, farther from the transmitter (Fig. II-14 (b)), A indicates edge-diffracted waves, while B represents wall-reflected waves from A, confirming long-distance propagation due to multiple reflections, supported by propagation loss characteristics.

These findings suggest that in the 300-GHz band, deep angle diffracted waves indoors exhibit significant losses and contribute minimally to power, similar to outdoors. Strongly reflected and scattered waves can arrive from fittings like surveillance cameras. Thus, using small reflecting panels can expand coverage indoors while keeping installation costs low.

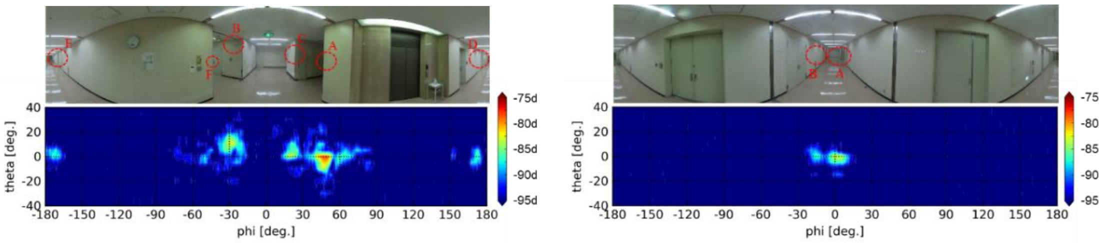

(a) Rx 1 (b) Rx 2

Fig. II-14. AoA distribution with photographs obtained at each indoor Rx.

II-1.3.4. Conclusion

We report measured AoA characteristics in the 300-GHz band, focusing on the NLOS conditions. The measured AoAs revealed that the contribution of diffracted waves from deep diffraction angles was minimal. Instead, the contributions of diffracted waves from shallow angles, metallic furnishings, and trees dominated under NLOS conditions.

Acknowledgements

These research results were obtained from the commissioned research (JPJ012368C00401) by National Institute of Information and Communications Technology (NICT), Japan.

REFERENCE

[1] T. Kawanishi, S. Hisatake, "ThoR," in THz Communications: Paving the Way Towards Wireless Tbps, T. Kürner, D. Mittelman, and T. Nagatsuma, Eds. Cham, Switzerland: Springer Int., 2022.

[2] S. Ito, Y. Kunisawa, T. Ooseki, T. Nagao and T. Hayashi, "Virtualized Terminal Using Terahertz-Band for Ultra High Capacity Towards Beyond 5G and 6G," in 2024 IEEE VTS Asia Pacific Wireless Communications Symposium (APWCS), Singapore, 2024, pp. 1-4.

[3] C. Han et al., "Terahertz Wireless Channels: A Holistic Survey on Measurement, Modeling, and Analysis," IEEE Commun. Surv. Tutorials, vol. 24, no. 3, pp. 1670–1707, 2022.

[4] M. Inomata et al., "Path-loss Characteristics and Modeling for 2-300-GHz bands in Urban Microcell Environment," 2023 17th European Conference on Antennas and Propagation (EuCAP), Florence, Italy, 2023, pp. 1-5.

[5] S. Ito, K. Takezawa and T. Hayashi, "Measurement-based Evaluation of Path Loss and Propagation Mechanisms in the 300 GHz band," 2023 IEEE 98th Vehicular Technology Conference (VTC2023-Fall), Hong Kong, Hong Kong, 2023, pp. 1-6.

[6] Y. Lyu et al., "Measurement-based channel characterization in a large hall scenario

at 300 GHz," in China Communications, vol. 20, no. 4, pp. 118-131, April 2023.

[7] S. Ito, A. Hiroki, T. Nagao and T. Hayashi, “Measurement Evaluation of Propagation Characteristics of the 300-GHz Band Focusing on the NLOS Environment,” 2025 IEEE 22nd Consumer Communications & Networking Conference (CCNC), Las Vegas, NV, USA, 2025, pp. 601-604.

II-1.4. Path Loss Characteristics from Microwave to Sub-Terahertz Bands in Urban Environment for Beyond 5G

Minoru Inomata, Wataru Yamada, Ryotaro Taniguchi, Daisei Uchida
NTT Access Network Service Systems Laboratories, NTT Corporation.
Nobuaki Kuno, Koshiro Kitao, Takahiro Tomie, Satoshi Suyama
NTT DOCOMO, INC.

Abstract **— Sixth generation (6G) mobile communication networks will require extremely high-speed and high-capacity communications data rates exceeding 100 Gbps using sub-terahertz bands. However, path-loss characteristics above 100 GHz have not been sufficiently studied in terms of distance attenuation and frequency dependency. Therefore, to clarify the system performances of 6G in new frequency bands and determine the service frequency bands, it is needed to clarify the basic path-loss characteristics above 100 GHz. We investigated the path-loss characteristics and propagation mechanism from 2 to 300 GHz in an urban microcell (UMi) environment. We also clarified the dominant paths that affect the distance attenuation and frequency dependency of path loss.**

II-1.4.1. Introduction

New spectrum used for 6G and beyond 5G are sub-terahertz (THz) bands above 100 GHz for extremely high-speed communication data rates exceeding 100 Gbps. The ITU-R Working Party 5D (WP5D) has agreed on a new recommendation on the Framework and overall objectives of the future development of IMT for 2030 and beyond and agreed a report on the technical feasibility in bands above 100 GHz [1]-[4]. 5G have been rolled out using a combination of sub 6 GHz and millimeter wave (mmW) band. And as networks move toward beyond 5G, newly exploiting the mid-bands in 7-24 GHz and the sub-THz bands, utilization of the combination of multiple frequency bands from microwave to sub-THz bands will be necessary for achieving extremely high-speed and reliable communications. In this study, aiming to exploit the new spectrums for beyond 5G, we reported the path loss, namely basic transmission loss, from microwave to sub-THz bands in urban environment [5]-[8].

II-1.4.2. Key Propagation Phenomena Affecting Radio Channel Characteristics in bands above 100 GHz

Fig. II-15 shows the key propagation phenomena that affect channel characteristics for the sub-THz bands in urban environment. ITU-R M.2412 [9] proposed models that can calculate path loss that building shadowing and human blockage is considered and the building penetration loss in accordance with the mixing ratio of building materials. The path loss governs the coverage distance and the interference levels for the coexistence of radio services using the same frequency bands. However, the M.2412 path loss models are constructed by using measurement frequency bands below sub 6 GHz and mmW bands [9]. Therefore, it is necessary to clarify the path loss characteristics, which includes frequency dependency from microwave to sub-THz bands for operating the combination of multiple frequency bands.

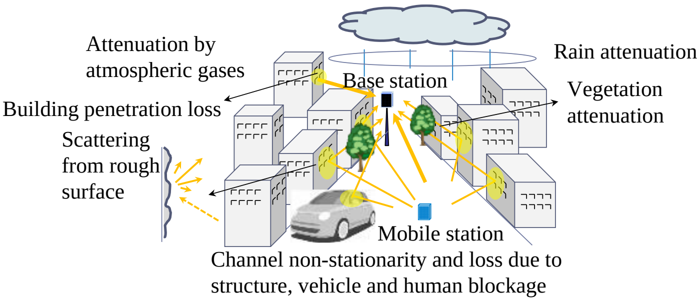

Fig. II-15. Key propagation phenomena in bands above 100 GHz [5][6].

II-1.4.3. Measurement System Setup

The measurement system uses frequency bands at 2, 26, 97, 158 and 300 GHz. Continuous wave (CW) signal was transmitted using the omni-directional antenna [7][8]. The omni-directional antenna with 60° of half power beam width (HPBW) for 2, 26, 97 GHz in the elevation plane, 20° of HPBW for 158, 300 GHz. At the 2 GHz, the Rx omni-directional antenna measured the path loss. At the 26, 97, 158 and 300 GHz, Rx measured the CW signal while the Cassegrain antenna with 4° of HPBW for 26 GHz, 2° of HPBW for 97 GHz, 1° of HPBW for 158 and 300 GHz was rotated 360 degrees in the azimuth plane and up to 20 degrees in the elevation plane. Path loss equivalent to the omni-directional antenna is obtained by this measurement method.

II-1.4.4. Path Loss Characteristics

The path loss measurement environment around Tokyo Station is shown in Fig. II-16 [7]. Path loss was measured at measurement points of the LOS and NLOS environment. The Tx antenna was set on the rooftop of a measurement vehicle with height of 2.55 m, which is lower than the surrounding building's rooftop level. The Rx antenna was fixed to the trolley, with height of 1.7 m. We compared the free space path loss (FSPL) $FSPL(f,d) = 32.4 + 20\log_{10} f + 20\log_{10} d$, M.2412, and measurement results. M.2412 path loss model was used a mandatory model for IMT-2020. The close-in (CI) model is always used to characterize the path loss for LOS and the Alpha-Beta-Gamma (ABG) model for NLOS. The CI model and ABG model are expressed by following equation:

$$PL_{CI}(f,d)(dB) = PL_{FSPL}(f,1) + 10n\log_{10} d + X_\sigma^{CI}$$

where n is the path loss exponent (PLE), and X_σ^{CI} is a shadow fading with a standard derivation of σ in dB.

$$PL_{ABG}(f,d)(dB) = 10\alpha \log_{10} d + \beta + 10\gamma\, log_{10}\left(\frac{f}{1\ \mathrm{GHz}}\right) + X_{\sigma}^{ABG}$$

where α and γ are the PLE and frequency dependence on path loss, respectively, β is the optimized offset in path loss. From Fig. II-17 (a) for LOS, the measured path loss indicate the similar tendency as the predicted path loss of FSPL. It is obvious that the direct wave in the LOS environment was dominant. Therefore, the PLE for M.2412 path loss model and PL_{CI} is equivalent to that for FSPL. From Fig. II-17 (b) for NLOS, PL_{ABG} by regressing the measured path loss had steeper PLE and larger frequency dependency than the calculation results using M.2412 path loss model. In urban NLOS environment, the diffracted and reflected waves with multiple reflection were major paths. Since the diffraction loss depends on the wavelength and the frequency dependency is significantly larger than M.2412 path loss model. Specifically, in the case of scattering from a building rough surface, the higher the frequency, the larger the scattering power and the lower the reflection power, so it is assumed that since larger reflected loss occurred, the path loss had steep distance attenuation.

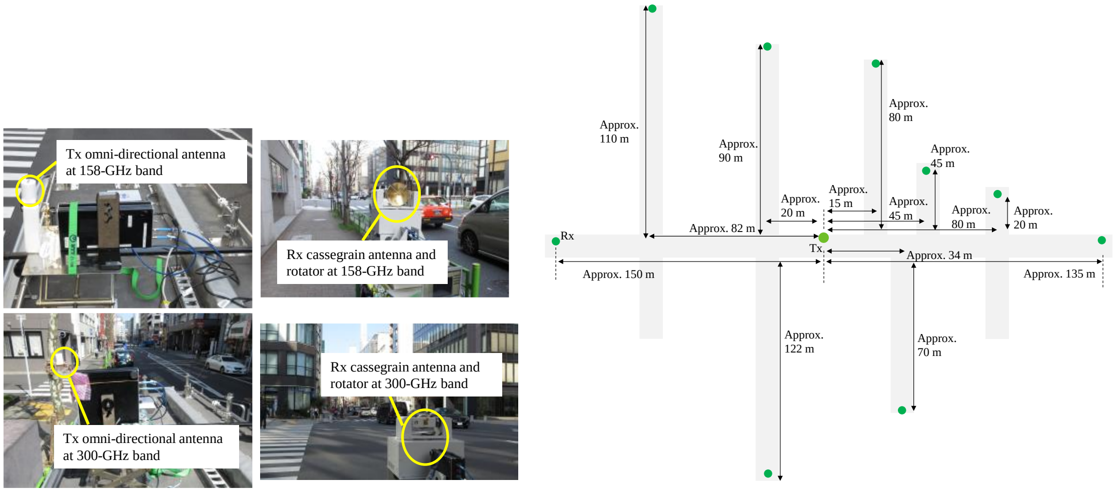

(a) measurement system setup (b) measurement routes

Fig. II-16. measurement system setup and routes [7]

Table. II-3. Comparison results [7]

		n	*Constant loss (dB)*		X_{σ}^{CI} (dB)
LOS	*PL_{CI}*	1.9	32.4+20log$_{10}$*f*		6.04
	FSPL	2.0	32.4+20log$_{10}$*f*		6.21
	M.2412	2.1	32.4+20log$_{10}$*f*		6.86
		α	β (dB)	γ	X_{σ}^{ABG} (dB)
NLOS	*PL_{ABG}*	4.34	-4.1	2.52	6.19
	M.2412	3.53	22.4	2.13	9.22

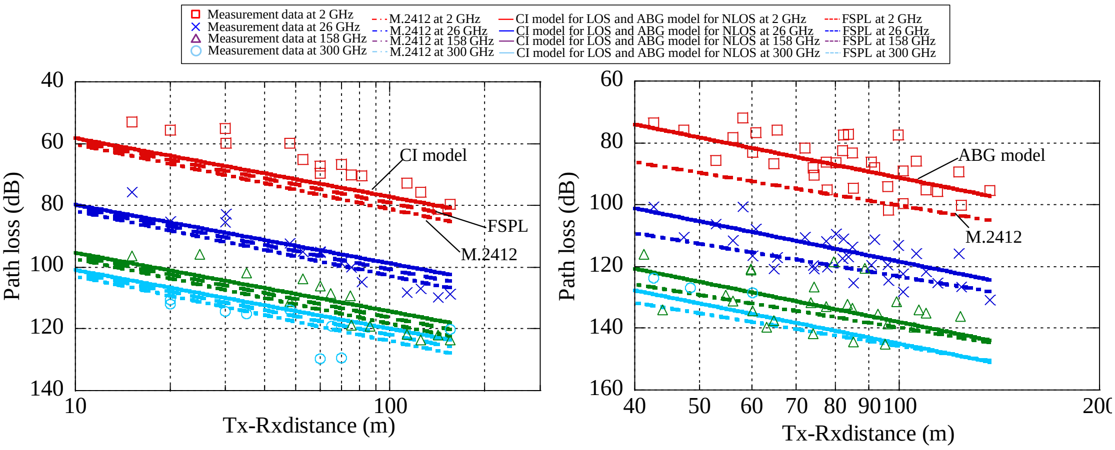

(a) LOS

(b) NLOS

Fig. II-17. measurement results [7]

II-1.4.5. Conclusion

Path loss characteristics were investigated from microwave to sub-THz bands in urban environment. In the basic outdoor path loss, the results indicate that since the direct wave in the LOS environment was dominant, the PLE for the CI model is equivalent to FSPL and M.2412. From results for NLOS, the PLE and frequency dependency were more significant than M.2412 due to larger diffraction and reflection loss.

REFERENCE

[1] NTT DOCOMO, INC. “White Paper, 5G Evolution and 6G,” Feb. 2021.

[2] ITU-R WP5D, “The ITU-R Framework for IMT-2030,” July.2023.

[3] ITU-R WP5D, “Preliminary draft new Report ITU-R M.[IMT.Above 100 GHz] Technical feasibility of IMT in bands above 100 GHz,” July 2023.

[4] D. Uchida, Technologies and Proof-of-Concept Activities for 6G 2022 (TPoC6G 2022) keynote speech, Finland, June 2022.

[5] M.Inomata, et al., “Sub-Terahertz Propagation Characteristics up to 150 GHz for 6G Mobile Communication Systems,” EuMA International Journal of microwave and wireless technologies, March 2022.

[6] M. Inomata et al., "Terahertz Propagation Characteristics for 6G Mobile Communication Systems," EuCAP2021, Germany, March 2021.

[7] M. Inomata et al., " Path-loss Characteristics and Modeling for 2-300-GHz bands in Urban Microcell Environment," EuCAP2023, Italy, March 2023.

[8] Rep. ITU-R M.2412-0, “Guidelines for evaluation of radio interface technologies for IMT-2020,” Oct. 2017.

II-1.5. Terahertz Band Building Penetration Loss Characteristics for Beyond 6G

Minoru Inomata, Ryotaro Taniguchi, Motoharu Sasaki,
Wataru Yamada, Yasushi Takatori
NTT Corporation

Abstract— **As cellular networks move toward 6G, newly exploiting the centimeter wave (cm-wave) and sub-terahertz (THz) bands, the utilization of a combination of multiple frequency bands will be necessary for achieving extremely high-speed and reliable communications. However, the building penetration loss characteristics have not been sufficiently studied in terms of the frequency dependency from the cm-wave to sub-THz bands. We therefore investigated and modeled the building penetration loss characteristics and, as the measurement results indicated a more gradual frequency dependency than the conventional ITU-R model, we opted to build the penetration loss model based on single transmission paths with the lowest transmission loss through multi-layer standard glass.**

II-1.5.1. Introduction

The new spectra utilized for 6G are sub-terahertz (THz) bands above 100 GHz to enable extremely high-speed communication data rates exceeding 100 Gbps [1]. It is now possible to use a significantly wider frequency bandwidth than 5G. The ITU-R Working Party 5D (WP5D), which is responsible for the overall radio system aspects of International Mobile Telecommunications systems, has agreed on a new recommendation on the framework and overall objectives of the future development of IMT for 2030 and beyond and published a report on the technical feasibility in bands above 100 GHz [2]-[8]. Therefore, it is necessary to clarify the building penetration loss characteristics and to model those characteristics, which include the frequency dependency from the cm-wave to sub-THz bands for operating the combination of multiple frequency bands. In this study, aiming to exploit the new spectra for 6G, we investigate the building penetration loss characteristics and propose a model from the cm-wave to sub-THz bands.

II-1.5.2. Measurement set up

The details of the measurement system setup for 2.2, 26.4, 97.5, and 158 GHz are summarized in Table. II-4. Fig. II-18 shows the measurement points. The Tx antenna was set on the roof of the building at a height of 2.24 m from the floor, and the Rx antenna was fixed to a trolley in various rooms at a height of 1.5 m from the floor. The building penetration loss was measured on routes A, B, C, and D on the 4th, 5th, and 6th floors with different incident angles. The azimuth incident angle of path is from 0 to 54.1

degrees and the elevation angle is from 1.5 to 13.1 degrees to obtain the additional loss due to the non-perpendicular incidence to the building facade. The distance from the Tx antenna to the building facade was about 29 m to minimize fading across the indoor measurement room, while between the Tx antenna and the building façade was the LOS environment. Also, to obtain the indoor distance attenuation, the indoor penetration depth was set to a maximum of 8 m with roughly 0.25-m intervals. The measurement building was composed of roughly 70% multi-layer standard glass and 30% concrete, which is a similar material composition to the low-loss model of the ITU-R M.2412 [3].

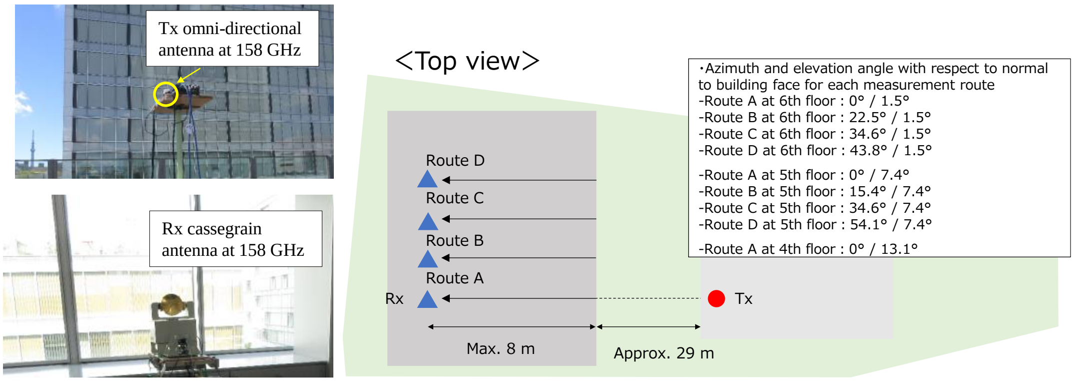

Fig. II-18. Measurement routes.

Table. II-4. Measurement system parameters.

Frequency	2.2 GHz	26.4 GHz	97.5 GHz	158 GHz
Signal	CW	CW	CW	CW
Tx antenna	Omni-directional antenna	Omni-directional antenna	Omni-directional antenna	Omni-directional antenna
Rx antenna	Omni-directional antenna	Cassegrain antenna	Cassegrain antenna	Cassegrain antenna
Tx antenna height	2.24 m from the floor	2.24 m from the floor	2.24 m from the floor	2.24 m from the floor
Rx antenna height	1.5 m from the floor	1.5 m from the floor	1.5 m from the floor	1.5 m from the floor
Tx antenna gain	2.1 dBi	2.0 dBi	0 dBi	7.0 dBi
Rx antenna gain	2.1 dBi	31.7 dBi	44.2 dBi	43.1 dBi
Max. measurable path loss	Approx. 151 dB	Approx. 200 dB	Approx. 198 dB	Approx. 152 dB

II-1.5.3. Measurement results

Typical building façades are composed of several materials. The measurement results in M.2412 model [3] can roughly be grouped into two categories: low building-penetration loss results for old buildings with standard glass, and high ones for modern buildings with infrared reflective glass. The proportion of measurement building composed of multi-layer standard glass was about 70%, and that of concrete was about 30%, and the material composite was similar to the low-loss model. Building penetration loss was calculated by sum of the building penetration loss through the external wall PL_{tw} and the indoor loss dependent on the depth into the building PL_{in}. PL_{tw} consists of an additional loss due to the non-perpendicular incidence and linear loss as a function of frequency. When the propagation is deeper into the indoor room, indoor loss PL_{in} and variation due to the shadowing of the furniture can occur. From the Fig. II-19, it was found that measurement loss due to the non-perpendicular incidence and indoor loss was equivalent to M.2412, but the measurement results were more gradually frequency-dependent than M.2412. Since the material loss tends to increase as the frequency becomes higher or permittivity becomes larger, the power of the transmission paths through concrete is significantly lower in bands above 100 GHz. Thus, it was assumed that the transmission paths through the glass were dominant and that the M.2412 low-loss model overestimated the building penetration loss due to the higher transmission loss of the concrete. In light of these findings, we designed an effective building penetration loss model based on single transmission paths with the lowest transmission loss through standard glass. The components of the proposed model are listed in Table. II-5. From the Table. II-6, the RMSE value of the proposed model was about 6.2 dB at 26.4 GHz, 3.4 dB at 97.5 GHz, and 11.6 dB at 158 GHz, which indicates an improvement over the M.2412 low-loss model for the 26.4–158 GHz bands.

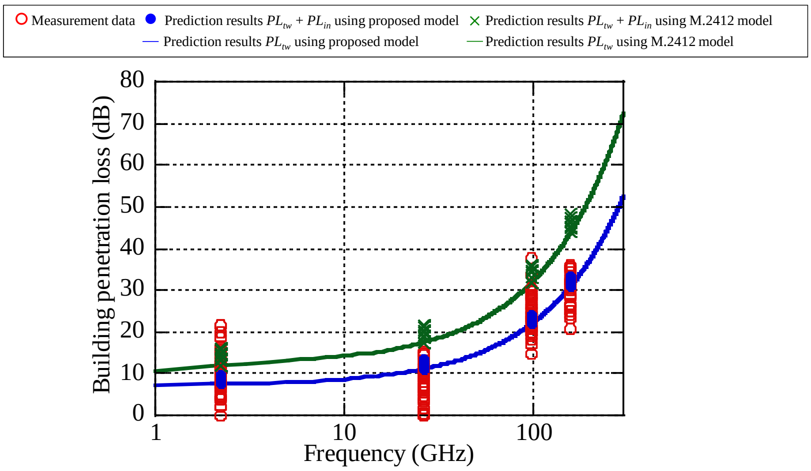

Fig. II-19. Measurement frequency dependency of the building penetration loss.

Table. II-5. Measurement system parameters.

	Path loss through external wall: PL_{tw} (dB)	
M.2412	$5 - 10\log_{10}(0.3 \cdot 10^{-L_{glass}/10} + 0.7 \cdot 10^{-L_{concrete}/10})$	
Prop.	$4.58 + L_{glass}$	
	Material loss: L_{glass} (dB)	Indoor loss: PL_{in} (dB)
M.2412	$2 + 0.2f$	0.5
Prop.	$2.58 + 0.15f$	0.28

Table. II-6. RMSE value for each frequency band.

	2.2 GHz	26.4 GHz	97.5 GHz	158 GHz
M.2412	6.4 dB	12.3 dB	9.4 dB	15.7 dB
Prop.	6.2 dB	6.1 dB	6.0 dB	4.1 dB

II-1.5.4. Conclusion

This paper introduced a measurement of the building penetration loss conducted from cm-wave to sub-THz bands. We investigated the building penetration loss characteristics on the basis of the measurement results and found that the results in the sub-terahertz bands were more gradually frequency-dependent than those of the conventional model. Therefore, we designed a building penetration loss model based on single transmission paths with the lowest transmission loss through multi-layer standard glass. We also confirmed the validity of the proposed model from the cm-wave to sub-THz bands.

REFERENCE

[1] NTT DOCOMO INC., “White Paper 5G Evolution and 6G (Version 5.0),” 2023. https://www.docomo.ne.jp/english/corporate/technology/whitepaper_6g/.

[2] Rep. ITU-R M.2541-0, “Technical feasibility of IMT in bands above 100 GHz,” May. 2024.

[3] Rep. ITU-R M.2412-0, “Guidelines for evaluation of radio interface technologies for IMT-2020,” Oct. 2017.

[4] M.Inomata, et al., “Sub-Terahertz Propagation Characteristics up to 150 GHz for 6G Mobile Communication Systems,” EuMA International Journal of microwave and wireless technologies, March 2022.

[5] M. Inomata et al., "Terahertz Propagation Characteristics for 6G Mobile Communication Systems," EuCAP2021, Germany, March 2021.

[6] M. Inomata et al., "Path-loss Characteristics and Modeling for 2-300-GHz bands in Urban Microcell Environment," EuCAP2023, Italy, March 2023.

[7] M. Inomata et al., "Sub-Terahertz MassiveMIMO Channel Sounder for 6G Mobile Communication Systems," EuCAP2024, United Kingdom, March 2024.

[8] M. Inomata, et al. "Building Penetration Loss Measurements and Modeling from Cm-Wave to Sub-Terahertz Bands," EuCAP2025, Sweden, March 2025.

II-1.6. Millimeter-Wave Urban Cellular Channel Characterization and High-Precision Site-Specific Simulation

Minseok Kim
Niigata University

Abstract**—This article proposed a site-specific channel modeling framework for millimeter-wave (mmWave) communication systems, leveraging the 3GPP map-based hybrid approach to enhance simulation accuracy. To improve prediction accuracy, an exponential decay model was introduced for non-line-of-sight (NLOS) cluster power-delay characteristics, addressing overestimation issues in deterministic models. Validation using the in-house channel model simulator (CPSQDSIM) demonstrated superior accuracy over the existing 3GPP map-based model. These results contribute to more precise mm-wave channel modeling for next-generation wireless networks.**

II-1.6.1. Introduction

With 50 billion connected devices projected by 2030, increasing communication demand leads to spectrum congestion, efficiency degradation, and interference. To support high data rates and low latency, millimeter-wave (mmWave) bands (24–71 GHz) offer high bandwidth but suffer from high propagation loss, obstacle sensitivity, and scattering effects. Accurate channel modeling is crucial for overcoming the limitations of existing models in mm-wave bands. Stochastic models (e.g., 3GPP, WINNER, COST2100) are easy to implement but lack site-specific precision. Deterministic models (e.g., ray tracing) provide environment-specific predictions but are computationally intensive. Hybrid models (e.g., QuaDRiGa, 3GPP map-based, Q-D model) balance accuracy and efficiency, integrating deterministic and stochastic components. However, modeling diffuse scattering effects remains a key challenge.

This work proposes a novel calibration method using an exponential decay model for power delay characteristics of non-line-of-sight (NLoS) clusters. This approach enhances deterministic modeling accuracy by integrating diffuse scattering effects without requiring complex material-specific setups, making it more feasible for large-scale propagation environments. Before deploying new wireless communication systems, it is crucial to analyze site-specific propagation behaviors and assess system-level performance. However, large-scale real-world testing is time-consuming, costly, and lacks reproducibility due to environmental variations. Therefore, high-precision radio wave simulation tools are essential for efficient system evaluation, optimization, and scenario-based testing. This study introduces a mmWave hybrid channel model with site-specific channel representation (SSCR), utilizing geometric data such as 2D maps and 3D CAD models to improve channel simulation accuracy for next-generation wireless networks [1].

II-1.6.2. Site-Specific Channel Modeling Methodology

This paper presents a quasi-deterministic (Q-D) channel model for site-specific channel representation (SSCR), as illustrated in Fig. II-20. The proposed model follows a three-step process: (Step 1) dominant paths are generated deterministically using simplified ray tracing, (Step 2) random cluster centroids are stochastically generated to capture site-specific inter-cluster properties (LSPs), and (Step 3) power spread is applied stochastically to define the complete cluster shape, ensuring accurate representation of site-specific intra-cluster properties (SSPs). The approach ensures site-specific propagation accuracy while maintaining spatial consistency, with deterministic clusters following geometry-based evolution and random clusters adhering to the 3GPP spatial consistency procedure. This study aims to develop a radio channel simulation technique for a cyber-physical system (CPS) wireless emulator, enabling high-precision site-specific radio propagation simulation. This significantly reduces the reliance on extensive field testing of wireless devices in real-world environments [3]. The proposed channel model is validated through measurement campaigns in two typical urban environments in Yokohama, Kanagawa, Japan: an urban macro (UMa) scenario around JR Kannai Station (Area 1) and an urban micro (UMi) scenario near Yokohama World Porters shopping mall (Area 2), as shown in Fig. II-21.

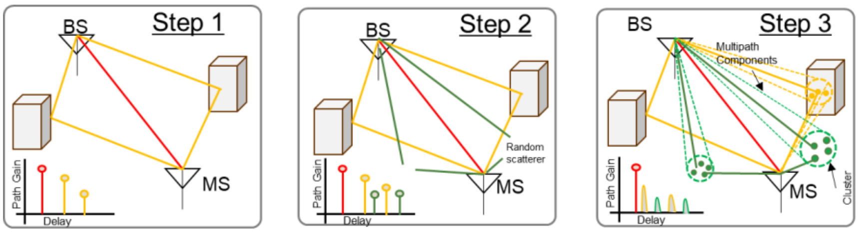

Fig. II-20. Quasi-deterministic (Q-D) channel model.

II-1.6.3. MmWave Channel Sounding

Fig. II-22 illustrates the in-house 24/60 GHz dual-band D-D channel sounder, comprising dual-band RF heads and baseband (BB) processing units [4]. The RF heads incorporate COTS phased array transceivers (EVK02001 for 24 GHz and EVK06002 for 60 GHz, SIVERS IMA) and feature four phased array antennas for a 90° azimuth sweep in four directions (−135°, −45°, +45°, and +135°). A dual 4×4 MIMO TDM scheme enables simultaneous measurement of 32 channels (16 per frequency band). The 60 GHz transceiver uses a 16-element ULA, while the 24 GHz transceiver employs a 2×8-element UPA, with HPBWs of 6° and 15°, respectively. Beam sweeping utilizes five beams at 24 GHz and 11 Tx/12 Rx beams at 60 GHz, achieving a 360° azimuth sweep. EIRP is 32 dBm at 24 GHz and 41 dBm at 60 GHz. Further details are available in previous works [4].

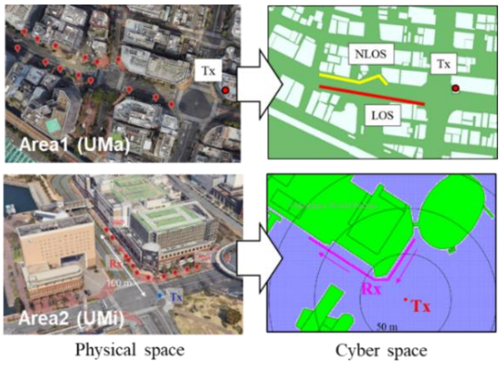

Fig. II-21. Evaluation Models.

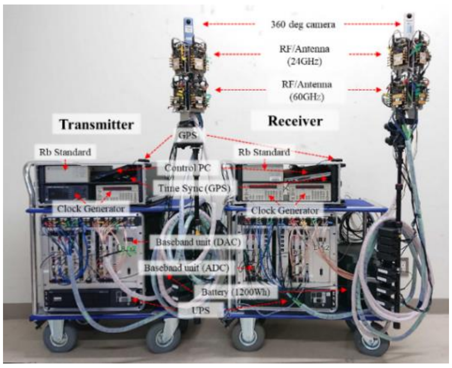

Fig. II-22. Channel sounder.

II-1.6.4. Extension of 3GPP Map-Based Model

To improve prediction accuracy, this study extends the 3GPP map-based hybrid channel model, which integrates deterministic and stochastic components to enhance site-specific channel modeling. The 3GPP model, widely used for 5G RAT evaluations, has evolved to incorporate 3D extensions, frequencies above 6 GHz, and spatial consistency procedures. Ensuring compatibility with the 3GPP framework is essential for developing new channel models. The 3GPP map-based model supports frequencies from 0.5 to 100 GHz across eight typical scenarios, including urban microcell (UMi) and urban macrocell (UMa). The methodology follows a 13-step process, including environment setup, deterministic cluster generation via ray tracing, random cluster modeling, and channel transfer function computation. While this study largely follows these steps for compatibility, modifications are introduced to generate a clustered multipath component (MPC) dataset (PathGridData) for use in the CPS wireless channel emulator [3]. The recipe for reflecting site-specific characteristics is as follows: 1) Deterministic Cluster Calibration: To improve NLoS cluster modeling, this study integrates a power delay decay model into Step 3 of the 3GPP model, enabling statistical calibration of deterministic clusters generated by ray tracing. This step adjusts power values using the z-score of power deviations, ensuring better alignment with measured environments. 2) Site-Specific Random Cluster Generation: Random clusters are generated following 3GPP procedures, but they incorporate site-specific large-scale (LSPs) and small-scale parameters (SSPs) derived from real measurement data, ensuring improved accuracy in the modeled propagation environment.

II-1.6.5. Development and Validation of Channel Model Generator

CPSQDSIM is a channel model simulator developed based on the proposed channel modeling framework, designed to generate a grid-wise clustered multipath component (MPC) dataset called PathGridData. As illustrated in Fig. II-23, the simulator integrates deterministic cluster centroids obtained via ray tracing with site-specific statistical parameters (LSPs and SSPs) to generate random clusters. The PathGridData is then created following the proposed channel model recipe described above. CPSQDSIM supports user-defined site-specific LSPs/SSPs datasets, enabling accurate reproduction of radio wave propagation characteristics for a given environment, enhancing the precision of site-specific channel modeling.

II-1.6.6. Conclusion

This work proposed a Q-D channel model framework for high-precision site-specific simulations at 24 GHz and 60 GHz. Measurement campaigns revealed significant NLoS power loss, especially at 60 GHz, leading to the development of an exponential decay model for improved accuracy. The framework integrates calibrated ray tracing, site-specific LSPs/SSPs, and 3GPP spatial consistency. The CPSQDSIM simulator generates grid-wise PathGridData, ensuring efficient radio wave modeling. Validation showed significant accuracy improvements over the 3GPP map-based model.

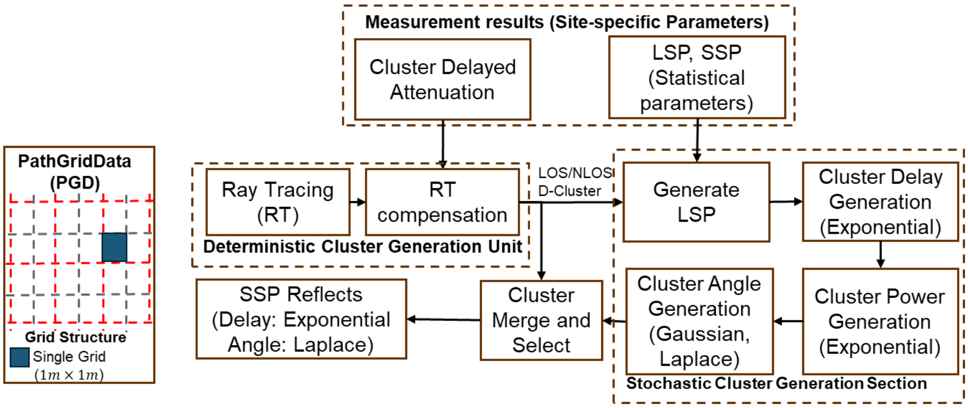

Fig. II-23. Functional Block diagrams of PathGridData generator (CPSQDSIM).

REFERENCE

[1] H. Tsukada et al., "Millimeter-Wave Urban Cellular Channel Characterization and Recipe for High-Precision Site-Specific Channel Simulation," *IEEE Trans. Veh. Technol.*, vol. 74, no. 3, pp. 3598–3612, March 2025

[2] “Advancement of radio wave simulation system technology in virtual space, ministry of internal affairs and communications, Japan,” Available: https://www.tele.soumu.go.jp/j/sys/fees/purpose/emulator/index.htm

[3] M. Kim et al., “A 24/60-GHz dual-band double-directional channel sounder using COTS phased arrays,” *IEEE ICC*, Seoul, Korea, May 2022, pp. 1113–1117.

[4] M. Kim et al., “Fast double-directional full azimuth sweep channel sounder using low-cost COTS beamforming RF transceivers,” *IEEE Access*, vol. 9, pp. 80288–80299, 2021.

II-1.7. THz Channel Characterization and Modeling Towards 6G Networks

Minseok Kim
Niigata University

***Abstract*— With the growing demand for extreme data rates and ultra-reliable low-latency communication (URLLC), the terahertz (THz) band (>100 GHz) has garnered significant attention. This article provides an overview of an in-house THz channel sounder and a measurement campaign conducted at 300 GHz in a typical indoor environment, such as a conference room. The developed system and measurement results offer new insights into THz channel propagation, contributing to the development and evaluation of mobile applications for future Beyond-5G (B5G) and 6G networks.**

II-1.7.1. Introduction

With the exponential growth of smart devices and doubling data rate demand every 18 months, the terahertz (THz) band (0.1–1 THz) emerges as a promising candidate to bridge the gap between millimeter-wave (mmWave) and optical frequencies. While mmWave can only partially meet the growing demand with advanced modulation and hardware, it falls short for ultra-high-speed applications like Tera-WiFi, Tera-IoT, Tera-backhaul, space communications, and nano-networks. Conversely, free-space optical (FSO) communication offers extreme data rates but suffers from environmental interference, background noise, and beam tracking challenges. The THz band provides a middle-ground solution, leveraging wide bandwidth and improved propagation characteristics.

Wireless communication relies on channel properties, which influence signal propagation more than transmission techniques or hardware. THz channel modeling requires extensive measurement campaigns using channel-sounding techniques to analyze signal modifications by the propagation medium. Extracting key channel parameters enables the development of accurate models, ensuring efficient spectrum utilization and unlocking the full potential of THz communications. While mmWave channels have been extensively studied through surveys on measurements, propagation, modeling, and future directions, these techniques cannot be directly extended to the THz band due to hardware constraints and unique propagation effects such as scattering from surface roughness and molecular absorption. Additionally, THz wavelengths enable large-scale antenna arrays, enhancing capacity but increasing modeling complexity due to non-stationarity across spatial, temporal, and frequency domains.

II-1.7.2. Sub-THz Channel sounder development

A 154/300 GHz dual-band channel sounder was developed based on a previous study [5] to facilitate high-precision THz channel measurements. The system parameters are summarized in Table. II-7. The transmitter generates two intermediate frequency (IF) signals at 8 GHz using an arbitrary waveform generator (AWG, M8195A, Keysight) operating at 64 GSa/s, along with a signal generator (SG). A local oscillator (LO) signal at 24.33 GHz is produced by the SG and upconverted using WR6.5 CCU and WR3.4 CCU (VDI Corporation), with multiplication factors of 6 and 12, resulting in signals in the 154 GHz and 300 GHz bands, respectively. The upconverted signals are filtered using band-pass filters (BPF) to eliminate image frequencies, amplified by power amplifiers (PA), and transmitted via a probe antenna. At the receiver, the transmitted signals are captured using a horn antenna and down-converted via WR6.5 CCD (154 GHz) and WR3.4 CCD (300 GHz) downconverters (VDI Corporation). The down-converted IF signals are subsequently amplified using low-noise amplifiers (LNA) and digitized by a high-speed digitizer (M8131A, Keysight) for further processing.

To enable precise time-delay resolution, multi-tone sounding signals were utilized with 4 GHz and 8 GHz bandwidths for the 154 GHz and 300 GHz bands, respectively. This configuration provided delay resolutions of 250 and 125 ps, while maintaining a 640 ns delay span. Due to propagation loss and the equivalent isotropic radiated power (EIRP) limit, the signal-to-noise ratio (SNR) of the received signal was significantly degraded, limiting the measurement range. To mitigate this, coherent averaging was employed across multiple symbol durations, effectively enhancing SNR and extending the effective measurement range.

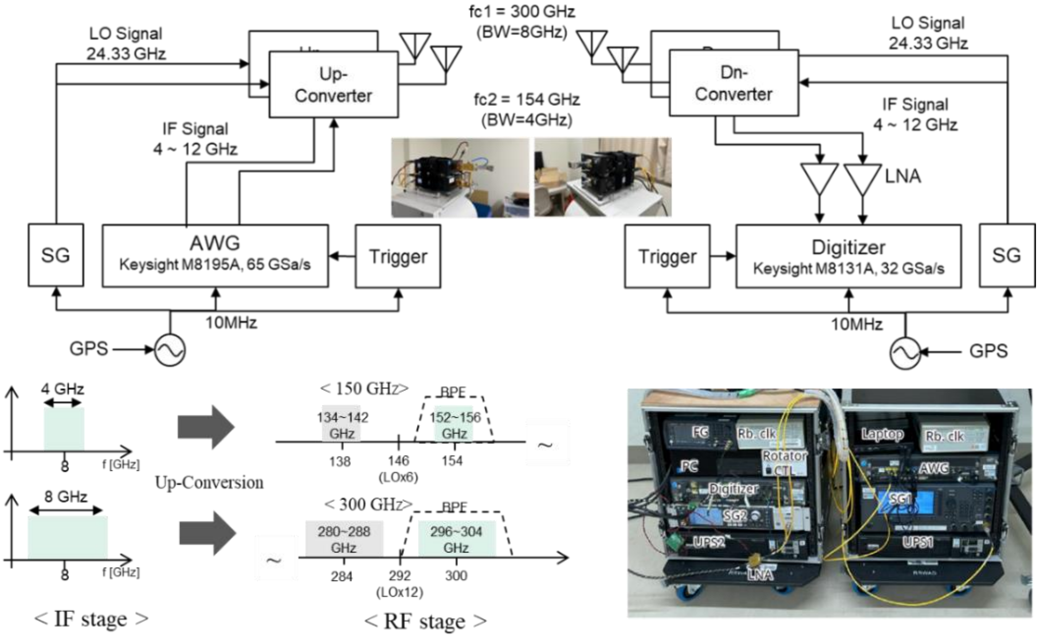

Fig. II-24. 154/300 GHz dual-band channel sounder.

Table. II-7. Channel Sounder Specification

	150 GHz band	300 GHz band
Center freq.	154 GHz	300 GHz
Signal BW	4 GHz	8 GHz
Sounding signal	2,560 tones	5,120 tones
Delay resolution	250 ns	125 ps
Delay span	640 ns	
Tx Ant	Gain: 26 dBi, HPBW: 9°	
Rx Ant		
EIRP	21.5 dBm	16.5 dBm
Dynamic range	62 dB@1m 42 dB@10m 22 dB@100m	60 dB@1m 40 dB@10m 20 B@100m

II-1.7.3. Measurement Campaigns and Results

Measurement campaigns were conducted in various indoor environments, including a conference room, office, and corridor, at 300 GHz [3][4]. As an example, Fig. II-25 illustrates the conference room measurement setup, where the receiver (Rx) antenna was positioned at 1.15 m, representing a mobile phone or laptop, while the transmitter (Tx) antenna was fixed at approximately 2.1 m, simulating an access point. A full azimuth scan was performed for all Rx positions, with the Tx rotating 180° along the azimuth plane. The measurement results, shown in Fig. II-26, provide insights into THz signal propagation by comparing the 300 GHz campaign with a previous 60 GHz campaign under a similar setup. The findings reveal that dominant clusters appear in both frequency bands, but at 300 GHz, the propagation is more LoS-dominant, exhibiting fewer multipath components (MPCs) due to higher loss compared to 60 GHz.

II-1.7.4. Conclusion

This work presents an in-house 154/300 GHz dual-band channel sounder, and a measurement campaign conducted in a medium-sized conference room. Due to the high bandwidth, clusters in the PDP exhibit impulse-like characteristics, enabling manual extraction based on PDP and ADPS analysis. The results were compared with those from a previous 60 GHz campaign in the same environment, revealing that dominant clusters appeared in both bands. A comparison of large-scale parameters (LSPs) confirmed that 300 GHz propagation is more LoS-dominant, with fewer significant multipath reflections due to higher propagation loss. The evaluated LSPs were further validated against existing literature, demonstrating good agreement.

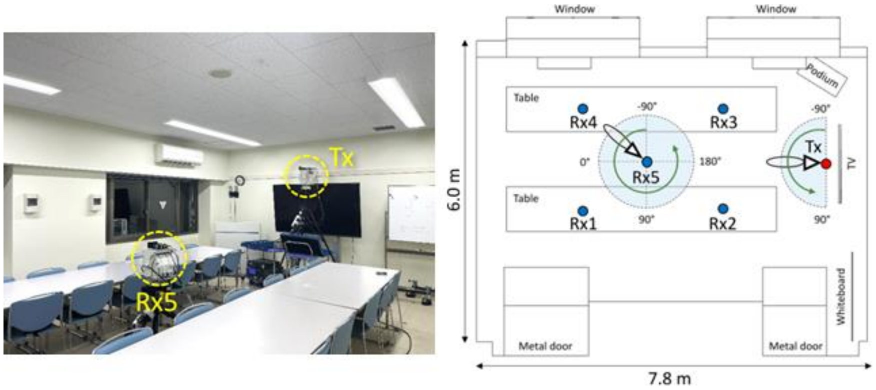

Fig. II-25. Conference room measurement setup.

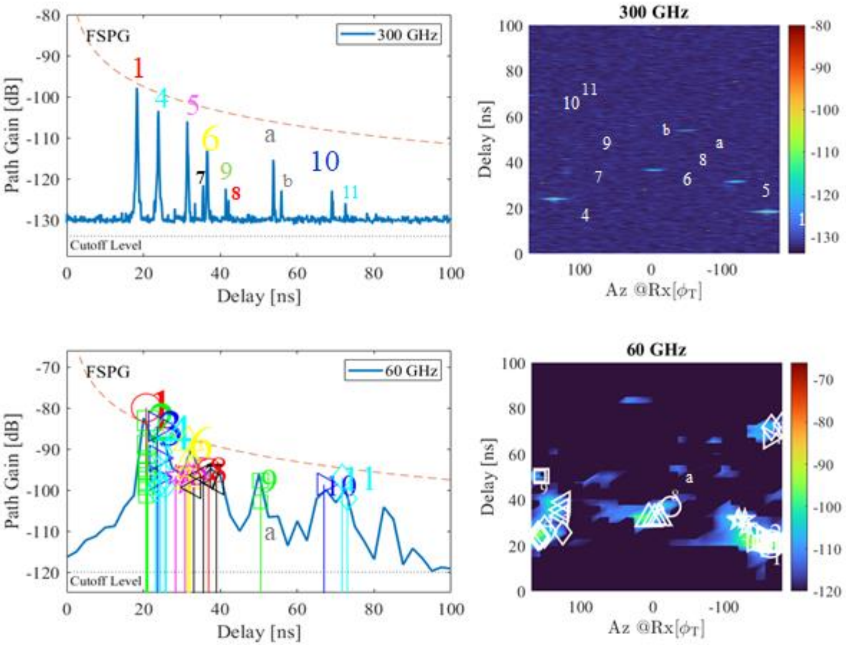

Fig. II-26. Power delay profiles (left) and azimuth delay power spectra (right) obtained at 300 and 60 GHz.

REFERENCE

[1] A. Ghosh, M. Kim, “THz Channel Sounding and Modeling Techniques: An Overview,” *IEEE Access*, Vol. 11, pp. 17823-17856, Feb. 2023.

[2] NICT beyond 5g R&D promotion project. Available: https://b5g-rd.nict.go.jp/en/

[3] M. Kim, A. Ghosh, R. Takahashi and K. Shibata, "Indoor Channel Measurement at 300 GHz and Comparison of Signal Propagation With 60 GHz," *IEEE Access*, vol. 11, pp. 124040-124054, 2023

[4] R. Takahashi, A. Ghosh, M. Mao and M. Kim, "Channel Modeling and Characterization of Access, D2D and Backhaul Links in a Corridor Environment at 300 GHz," *IEEE Trans. Antennas Propag.*, Vol. 73, No. 4, 2025.

II-2. Simulation

II-2.1. Fast Propagation Simulation by CI Method for CPS Realization

Takahiro Tomie, Satoshi Suyama, Koshiro Kitao, Nobuaki Kuno
NTT DOCOMO, INC.

***Abstract*— In order to maximize the performance of 6G systems using dynamic control by cyber-physical system (CPS), a technology for estimating and predicting radio propagation characteristics in real time with high accuracy is required. To realize the technology, we focused on the outdoor environment and proposed the color images method (CIM). In this article, we compare estimated path loss results of an outdoor urban environment using the CIM with the measured results in high frequency bands of sub-6 GHz band and millimeter-wave to clarify the estimation performance of the CIM. The root mean squared errors (RMSEs) of the difference between the estimated results and the measured results are small about 8 dB for all frequencies. The calculation time is extremely short.**

II-2.1.1. Introduction

Currently, research and development of realization of the 6th generation mobile communication system (6G) are carried out intensively by many organizations around the world [1], [2]. The requirements for 6G are extremely high such as a peak data rate of more than 100 Gbps, end-to-end latency of less than 1 ms, more than 10 million devices per square km for connecting, etc. In order to maximize the performance of 6G systems using dynamic control by cyber-physical system (CPS), a technology for estimating and predicting radio propagation characteristics in real time with high accuracy is required. This method also needs to be suitable for site-specific environments. Although there are several conventional estimation methods for specific environment such as ray tracing method (RTM) [3], [4], method based on deep learning [5]-[7], etc., these methods still do not satisfy the requirements of short calculation time and high accuracy. Hence, we proposed a new method named color images method (CIM) and clarified its high performance in an outdoor urban environment at low frequency band of 1 GHz [8]-[10]. However, the performance in high frequency bands has not been clarified. In this work, we estimated path loss results of an outdoor urban environment using the CIM and compared with the measured results in high frequency bands of sub-6 GHz band and millimeter-wave to clarify the estimation accuracy and calculation time of the CIM [11].

II-2.1.2. Evaluation Methods

II-2.1.2.1. Measured Data

For evaluating estimation accuracy of the CIM in high frequency bands, a measurement path loss data set of the outdoor environment in [12] is used. Fig. II-27 shows the Tx position, measurement courses and measurement conditions. The evaluation area is about 1 km^2. The Tx was set on the roof top of a building with 25 m height from the ground. The average height of the buildings in this area was about 20 m. The Rx was set on the roof top of a measurement car with 2.5 m height from the ground. The Rx was moved on the measurement courses to measure path loss at frequencies of 2.2, 4.7, 26.4, 66.5 GHz. After measurement, the median path loss at 10 m length was processed and thinned to a total of 1472 points. For the case of 66.5 GHz, only 392 points were used due to the limited range of the measurement equipment.

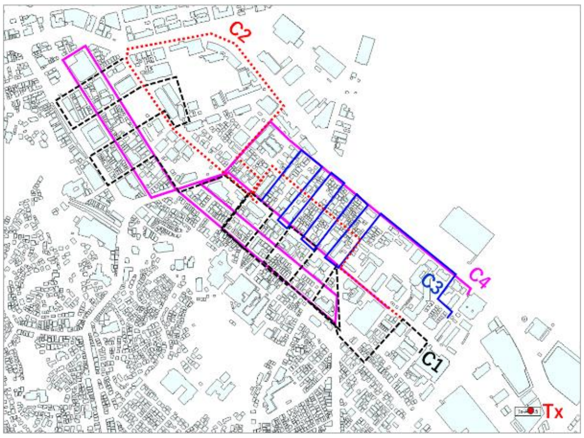

Fig. II-27. Position of the Tx and the measurement courses.

II-2.1.2.2. CIM

In this section, we describe a brief overview of the CIM proposed in [8] and its calculation conditions. The CIM is a simplified method for calculating scattering of building walls. Specifically, to find the scattering walls and calculate the scattered power, different RGB colors are assigned to walls of all buildings in the evaluation area, and two types of color images of the walls which are viewed from the positions of Txs and Rxs respectively, are created as shown in Fig. II-28. Here, the number of colors corresponds to the number of walls of all buildings. These images have view range of -90 degrees to +90 degrees in elevation, and -180 degrees to +180 degrees in azimuth. In these images, the number of pixels of each color corresponds with the visible area of each wall and depends on the distance and viewed angle from viewpoint (Tx or Rx) to the wall. Next, the scattering walls are detected by the corresponding colors which existed in both the Tx's image and Rx's image. By counting the number of pixels of these colors and multiplying with coefficients, the total received power P_R at each position of the Rx can be expressed as below:

$$P_\mathrm{R} = \sum_i k \cdot C(i) \cdot N_{\mathrm{P,T}}(i) \cdot N_{\mathrm{P,R}}(i) \tag{1}$$

Where $N_{\mathrm{P,T}}(i)$, $N_{\mathrm{P,R}}(i)$ are numbers of pixels of the colors corresponding with the scattering wall $\#i$ in Tx's image and Rx's image, respectively. The $\#i$ can be representative for the index of path i. $C(i)$ is a coefficient related to the transmitting power and the gains of the Tx antenna and Rx antenna. The coefficient k depends on materials of the walls, the frequency and size of image. In calculation, the coefficient k is defined as below:

$$10 \cdot log_{10} k = -198 - 20 \cdot log_{10},\ f[\mathrm{GHz}] \tag{2}$$

where f is the frequency with unit of GHz. In addition, the image size is 7200*3600 pixels.

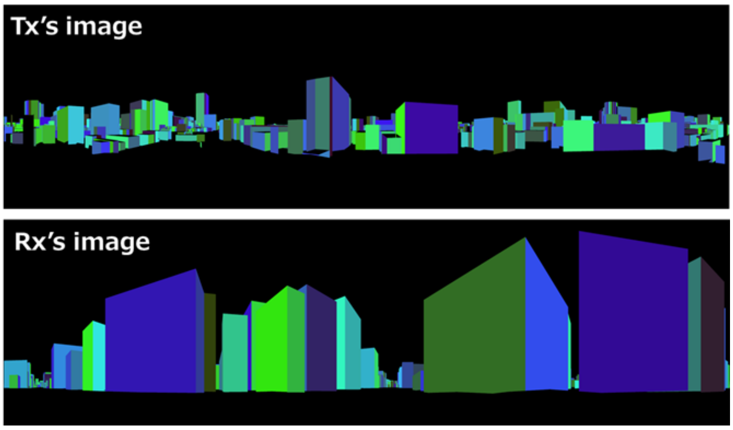

Fig. II-28. The color images viewed from the Tx and the Rx

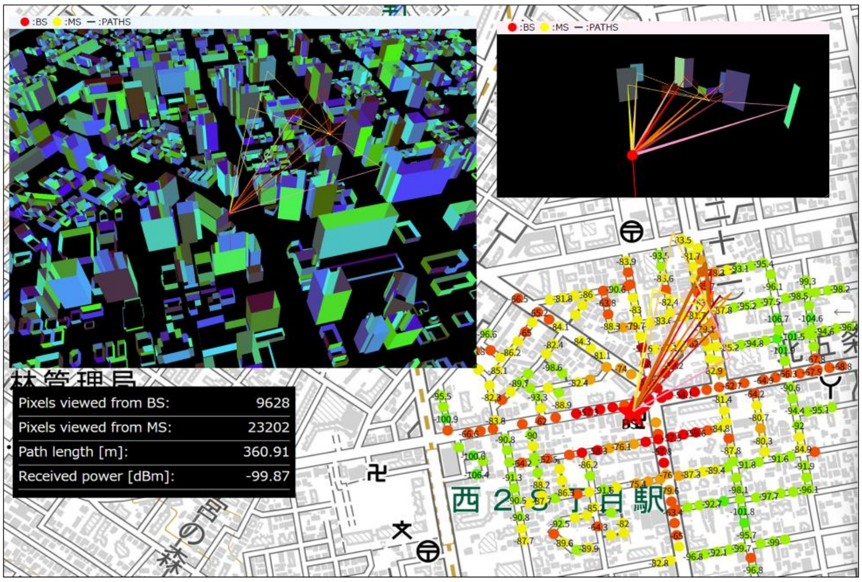

Pixels viewed from BS:	9628
Pixels viewed from MS:	23202
Path length [m]:	360.91
Received power [dBm]:	-99.87

Fig. II-29. The area evaluating tool using the CIM

The CIM can be used for calculating not only one-bounce scattering path but also more than two-bounces scattering path. Moreover, the CIM can calculate not only received powers (pathloss) but also delays, and angles of multipath of outdoor environment. To achieve short calculation time, the CIM can be divided into pre-processing and post-processing. The pre-processing includes creating and analyzing all Rx's images and storing the analyzed results to a database (DB). The post-processing includes creating and analyzing the Tx's image, matching the analyzed Tx's image result with analyzed Rx's image results, and calculating received power. Normally, pre-processing can be done in advance. Therefore, when radio propagation estimation is required, only post-processing is needed to do resulting in very short calculation time. Fig. II-29 shows the area evaluating tool using the CIM. The tool includes height above sea level data, building data, and road data as a database (DB). In addition, in order to perform calculations over a wide area with short calculation time, receiver points (Rxs) are located at certain intervals on roads, and images viewed from these Rxs are created and analyzed, then stored in the DB (pre-processing) in advanced. In addition, parallel processing on a computer is also utilized.

II-2.1.3. Performance Evaluation

Fig. II-30 shows the comparisons of estimated path loss results of the CIM with the measured results for course C1. It is found that estimated results of the CIM are matched with the measured results at all frequencies, especially at frequencies of 2.2, 4.7 GHz.

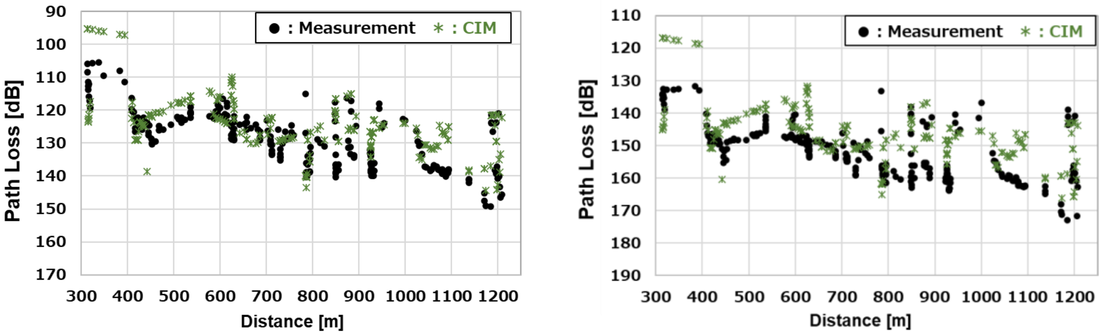

(a) $f = 2.2$ GHz

(c) $f = 26.4$ GHz

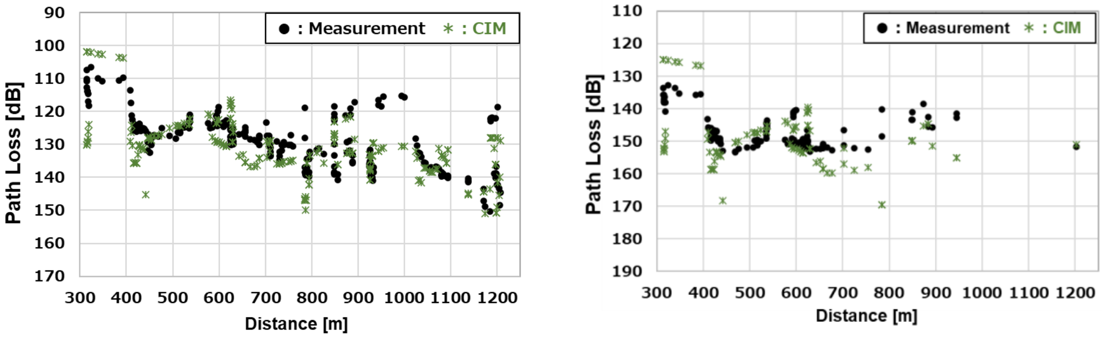

(b) $f = 4.7$ GHz

(d) $f = 66.5$ GHz

Fig. II-30. Comparison results for course C1

Fig. II-31 shows that, for each course, the RMSE has the nearly same trend with respect to frequency. The course C1 has the smaller RMSEs than the other courses except when the frequency is 66.5 GHz. For all courses, the RMSEs are 7.8, 7.7, 8.4, 7.5 dB at 2.2, 4.7, 26.4, 66.5 GHz, respectively. These values are nearly the same as the RMSE of the different urban outdoor environments in [8]-[10]. It means that the RMSE is independent of frequency and about 8 dB for all frequencies. Hence, the CIM has high estimation accuracy. The reasons for small values of RMSE of the CIM are that the CIM calculates received power based on scattering (arbitrary directional reflection) and scattering power is proportional with visible areas (numbers of pixels) of scatting walls viewed from the Tx and Rx. These are considered to match the real environment with buildings which have roughness and complex structures of walls resulting in scattering radio waves to arbitrary direction.

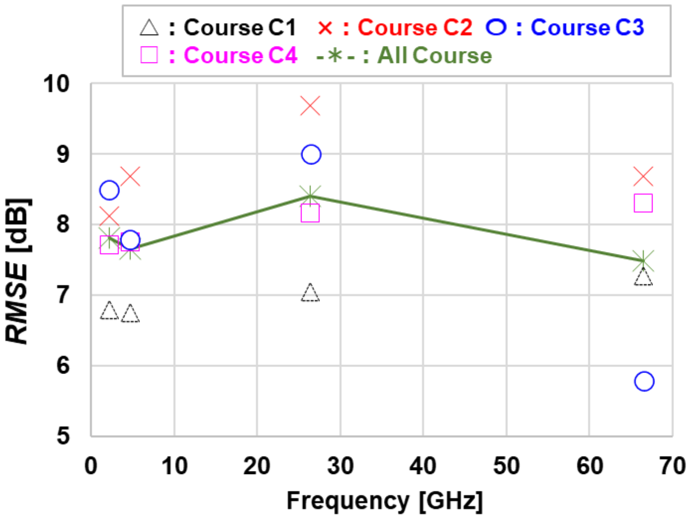

Fig. II-31. RMSE of difference of estimated results and measured results

About calculation time, the pre-processing and post-processing time were very short with 132 seconds and 8 seconds, respectively. In general, for the case of using ray tracing method to evaluate this area, the calculation time is more than several hours. Hence, the CIM has very short calculation time.

II-2.1.4. Conclusion

In this work, we estimated path loss results of an outdoor urban environment using the CIM and compared with the measured results in high frequency bands of sub-6 GHz band and millimeter-wave. It is found that the RMSEs of estimated errors are independent of frequency and are small, about 8 dB for all frequencies. The calculation time is very short with 8 seconds of post-processing. It means than the CIM has short calculation time and high accuracy in estimating radio propagation characteristics for sub-6 GHz band and millimeter-wave. In future work, we plan to consider using GPU technologies for real-time estimation of radio propagation characteristics.

REFERENCE

[1] NTT DOCOMO, INC. “White paper, 5G Evolution and 6G (Version 4. 0),” Jan. 2022. https://www.docomo.ne.jp/english/binary/pdf/corporate/technology/whitepaper_6g/DOCOMO_6G_White_PaperEN_v4.0.pdf

[2] Hexa-X, “Towards Tbps communications in 6G: use cases and gap analysis, ” Deliverable D2.1, Jun. 2021.

[3] S. C. Kim, et. al., "Radio propagation measurements and prediction using three-dimensional ray tracing in urban environments at 908 MHz and 1.9 GHz," IEEE Trans. Veh. Technol., vol. 48, no. 3, pp. 931–946, May 1999.

[4] Wireless InSite Reference Manual, Version 3.3.4.1, https://www.remcom.com

[5] M. Ayadi, et. al.,, “A UHF Path LossModel Using Learning Machine for Heterogeneous Networks,” IEEE Trans. AP, val.65, no.7, pp.3675-3683, 2017.

[6] N. Kuno, et. al., "Deep Learning-Based Path Loss Prediction Using Side-View Images in an UMa Environment," EuCAP2022, Mar.-Apr. 2022.

[7] H. Nakabayashi and K. Itoi "Path Loss Prediction Method Merged Conventional Models Effectively in Machine Learning for Mobile Communications,” IEICE Trans. Commun. Vol. E105-B No. 6 pp. 737-747.

[8] T. Tomie, et. al., " A Novel Estimation Method of Radio Propagation Characteristics Based on Color Images,” 2022 IEEE 96th Vehicular Technology Conference, pp. 1-5.

[9] T. Tomie, et. al., " Evaluation of High-Performance Radio Propagation Simulation Method in Path Loss Estimation,” 2023 IEEE 97th Vehicular Technology Conference, pp. 1-5.

[10] T. Tomie, et. al., " A method of path loss prediction based on computer graphics technologies,” IEICE Communications Express, 2023 Vol. 12, No. 6, p. 300-304.

[11] T. Tomie, et. al., " Performance of Color Images Method for Path Loss Estimation in High Frequency Bands,” 2024 IEEE 99th Vehicular Technology Conference, pp. 1-5.

[12] M. Sasaki, et. al., “Extension of ITU-R Site-General Path Loss Model in Urban Areas Based on Measurements from 2 to 66 GHz Bands,” IEICE Trans. Commun. vol. E104.B, no. 7, pp. 849–857, 2021.

II-2.2. AI-Based Radio Propagation Modeling and Data Augmentation

Tatsuya Nagao, Takahiro Hayashi
KDDI Research, Inc.

***Abstract*— Traditional statistical propagation models based on regression models using simple environmental parameters such as the distance between the transmitter and receiver and actual measurement data are widely used. However, this method does not reflect site-specific environmental information in the model, and the prediction accuracy of propagation characteristics for each location is insufficient. Therefore, in recent years, various studies have been conducted on propagation modeling using AI with map data around the Tx and Rx points, and it has been shown that site-specific and highly accurate estimation can be achieved. However, in general, to construct a highly accurate model using AI (especially supervised machine learning), a large amount of measurement data is required for training. Therefore, in this article, we describe a frequency extension method using fine tuning and a data extension method using generative AI.**

II-2.2.1. Introduction

For the purpose of constructing a site-specific and highly accurate radio propagation model, AI-based modeling methods using map data around the Tx and Rx points are being developed [1-4]. This approach uses machine learning techniques such as image recognition to directly consider the propagation environment, which was difficult to express using traditional statistical models, and to extract features from multidimensional input data, and then models the propagation characteristics by adding site-specific environmental information using learning with actual measurement data as the objective variable, as shown in Fig. II-32.

In addition to AI-based methods, the accumulation of measurement data under various conditions is an important practical issue, as is the modeling method itself, when it comes to understanding and modeling radio propagation characteristics. In general, the measurement of radio propagation characteristics requires a great effort in terms of resources, including the construction of measurement systems and experimental environments, and data processing, so there is a growing trend towards the opening up of these measurement data [5]. The US National Telecommunications and Information Administration (NTIA) has published long-term, long-distance propagation measurement data. In ITU-R SG3 (Study Group 3), as part of the study of radio propagation for the improvement of wireless communication systems, a database called DBSG3 is maintained, and it is possible to register data to the database in the form of contributed documents from ITU member organizations. The IEEE provides a service called IEEE DataPort, which contains measurement data from various scenarios, including valuable data, such as that measured on ships and in agricultural areas. In Japan, the Propagation Database Committee, which is under the Technical Committee on Antennas and Propagation of the Institute of Electronics, Information and Communication Engineers (IEICE), is leading the provision of a propagation database and is also holding competitions.

Thus, towards the further activation of research and development related to radio propagation, efforts are being made to share valuable propagation data, but both the quality and quantity of data are important for improving the accuracy and generality of propagation models. In particular, AI-based modeling methods generally require a large number of training data. Therefore, in the following, we will introduce two approaches to this issue in AI-based propagation modeling. One is the fine tuning of models with fewer data, and the other is data augmentation using generative AI.

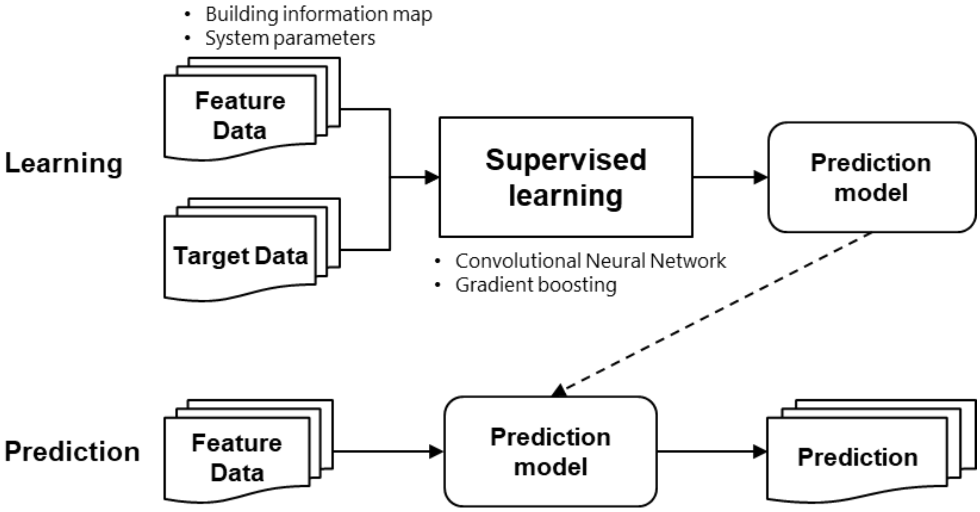

Fig. II-32. Overview of AI-based radio propagation modeling

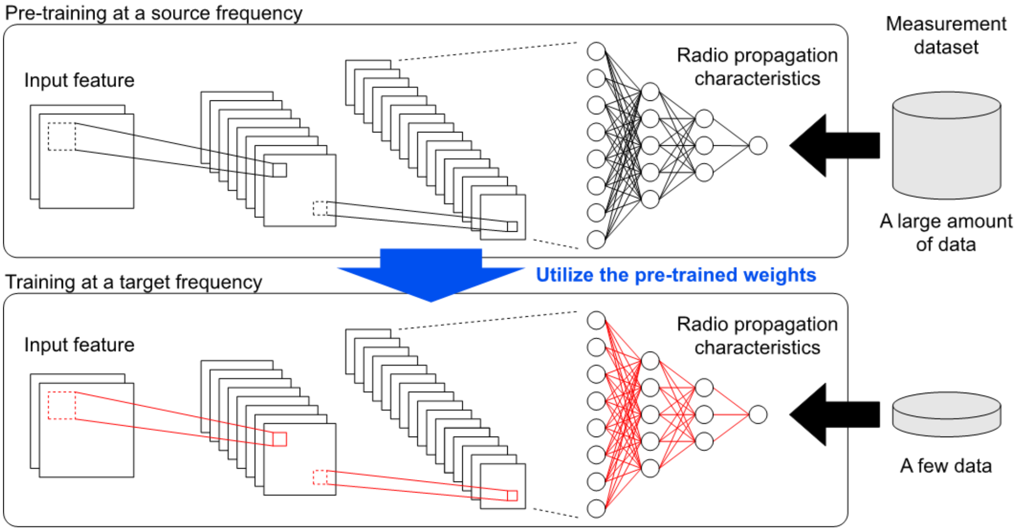

Fig. II-33. Frequency extension method of radio propagation model using fine tuning

II-2.2.2. Frequency Extension of Radio Propagation Model Using Fine Tuning

As mentioned above, to construct a highly accurate propagation model with AI, a large amount of training data is required. For example, in mobile networks such as 4G and 5G, data collection using system logs and other methods is possible for the frequencies in operation. However, when introducing new frequencies, the data that can be obtained may be severely limited.

This section describes the frequency extension method for propagation models using fine tuning proposed by the authors [6]. An overview of the proposed method is shown in Fig. II-33. This method applies fine tuning, a type of transfer learning, to construct a model with less accuracy degradation even when there are only a few training data for a new frequency f_t, based on a high-precision propagation model constructed by frequency f_s.

In deep learning, the initial values of the weights to be learned are usually set randomly, and a high-precision model can be constructed by minimizing the error between the training data (i.e. the ground truth) and the output values, which is expressed by the loss function, by optimizing the weights. The weights learned in this way are parameters that express the relationship between environmental information and propagation characteristics.

In the proposed method, the pre-trained weights are used as initial weights, and the weights are retrained using new frequency training data. This means that only the differences in the propagation characteristics due to the differences in frequency have to be trained, so even with a small amount of training data, the accuracy degradation is small, and a new frequency model can be constructed efficiently. This means that only the differences in propagation characteristics due to the differences between frequencies f_s and f_t need to be trained, so even with a small number of training data, the accuracy degradation can be kept to a minimum, and a new frequency model can be constructed efficiently.

The evaluation result of the proposed method in the 2.1 GHz path loss model is shown in Fig. II-34. The conventional method is the result of training with random initial weights without pre-training. The proposed method is the result of fine-tuning the weights pre-trained using approximately 80,000 points of 800 MHz training data as the initial weights. The horizontal axis shows the number of training data used to construct the 2.1 GHz model, and the vertical axis shows the RMSE. As you can see from the figure, the RMSE degrades by approximately 5 dB when the number of training data is about 700 points in the conventional method, whereas the proposed method is able to suppress the degradation to approximately 2 dB. This is equivalent to the accuracy when using approximately 7,700 points of training data in the conventional method.

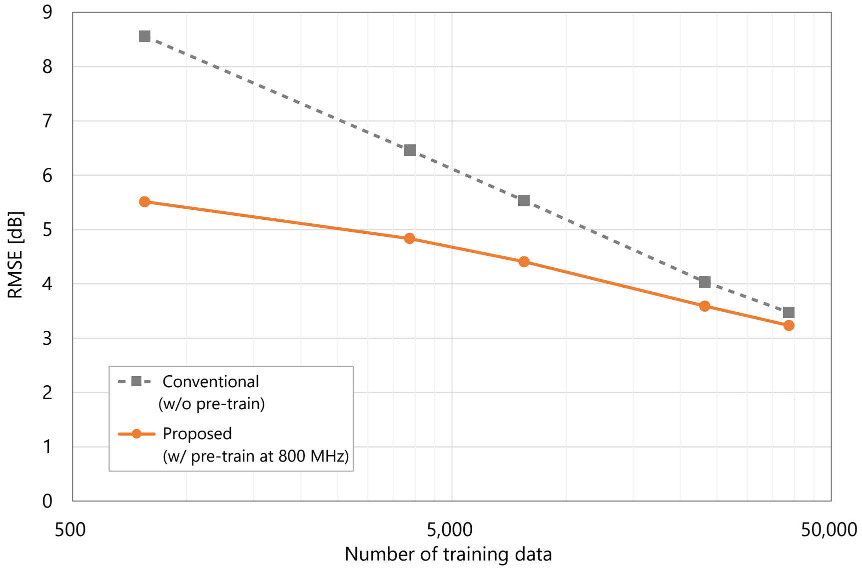

Fig. II-34. Evaluation result of prediction at 2.1 GHz

II-2.2.3. Generative AI-Based Data Augmentation for Radio Propagation Modeling

In this section, we will discuss another approach to improving the accuracy and generality of propagation models: the data augmentation method using generative AI [7]. As mentioned above, although efforts are being made to open up propagation data, it is also essential to expand environmental data for the construction of site-specific propagation models. However, acquiring 3D models of actual cities often requires costs, and in some cases, it is difficult to obtain sufficient data. Therefore, by using the Denoising Diffusion Implicit Model (DDIM), which is an image generation model, to generate a 2D map of building placement, and by assigning a building height to each building based on the distribution of building heights relative to the building area extracted from the actual 3D model of the city, it is possible to generate a fictional 3D model. By using this 3D model to perform ray tracing and other propagation simulations, it is expected that the training data can be augmented, and that this will contribute to improving the generalizability of the propagation model.

II-2.2.4. Conclusion

In this article, we introduced the opening up of actual measurement data on radio propagation characteristics, and we also focused on the issue of the availability of training data on AI-based radio propagation modeling technology and introduced two approaches: frequency expansion through fine-tuning and augmentation of 3D city models through generative AI. We expect that these approaches will contribute to improving the accuracy and generalization performance of propagation models, both by expanding the actual measurement data and by researching and developing more efficient modeling techniques.

Acknowledgements

This research has been conducted under the contract "R&D on the deployment of mobile communication systems in the millimeter wave band and other frequencies" (JPJ000254) made with the Ministry of Internal Affairs and Communications of Japan.

REFERENCE

[1] T. Imai, K. Kitao and M. Inomata, "Radio Propagation Prediction Model Using Convolutional Neural Networks by Deep Learning," *2019 13th European Conference on Antennas and Propagation (EuCAP)*, Krakow, Poland, 2019, pp. 1-5.

[2] T. Hayashi, T. Nagao and S. Ito, "A study on the variety and size of input data for radio propagation prediction using a deep neural network," *2020 14th European Conference on Antennas and Propagation (EuCAP)*, Copenhagen, Denmark, 2020, pp. 1-5, doi: 10.23919/EuCAP48036.2020.9135876.

[3] T. Nagao and T. Hayashi, "A Study on Urban Structure Map Extraction for Radio Propagation Prediction using XGBoost," *2021 15th European Conference on Antennas and Propagation (EuCAP)*, Dusseldorf, Germany, 2021, pp. 1-5, doi: 10.23919/EuCAP51087.2021.9411102.

[4] T. Nagao and T. Hayashi, "A Study on Path Loss Modeling using ResNet and Pre-Training with Free Space Path Loss," *2022 IEEE 33rd Annual International Symposium on Personal, Indoor and Mobile Radio Communications (PIMRC)*, Kyoto, Japan, 2022, pp. 01-05, doi: 10.1109/PIMRC54779.2022.9977760.

[5] W. Yamada, N. Kita, H. Iwai, T. Imai, “Activities for Open Data in Radio Propagation Research Fields,” The journal of the Institute of Electronics, Information and Communication Engineers 106 (7), 591-596, 2023-07.

[6] T. Nagao and T. Hayashi, "Fine-Tuning for Propagation Modeling of Different Frequencies with Few Data," *2022 IEEE 96th Vehicular Technology Conference (VTC2022-Fall)*, London, United Kingdom, 2022, pp. 1-5, doi: 10.1109/VTC2022-Fall57202.2022.10012911.

[7] R. Hagiwara, K. Ichige, T. Nagao and T. Hayashi, "Creation of Virtual City 3D Model for EM-Wave Propagation Dataset Extension," *2024 International Technical Conference on Circuits/Systems, Computers, and Communications (ITC-CSCC)*, Okinawa, Japan, 2024, pp. 1-5, doi: 10.1109/ITC-CSCC62988.2024.10628201.

II-2.3. Study on Machine Learning Propagation Loss Estimation Model using Point Cloud Data

Satoshi Iwasaki, Kento Sugiyama, Kenshi Horihata, Yukiko Kishiki
KOZO KEIKAKU ENGINEERING, INC.

***Abstract*—In this article, a machine learning model that uses point cloud data to improve the expressiveness of environmental information in propagation loss estimation was proposed. Conventional methods using CNN for 2D matrix data have the problem of insufficient representation of environments with complex structures. In this proposed model, environmental parameters that extract features from 3D data of buildings and structures are combined with system parameters such as the distance between the transmitter and receiver, and the features are learned using PointNet to estimate propagation loss. The evaluation was carried out using an outdoor bridge environment (measured data in the 2.4 GHz band) and a virtual indoor environment (simulation data using ray tracing). The results confirmed that feature extraction using PointNet is effective. In particular, in indoor environments, an estimation was possible that took into account the effects of blocking, diffraction and transmission loss. This method allows propagation loss to be estimated using a machine learning model in environments with complex structures that were difficult to express using CNN, and contributes to the construction of a highly accurate radio wave propagation model.**

II-2.3.1. Introduction

The application of machine learning to propagation loss estimation models has been investigated in various ways [1]. In particular, for propagation models assuming microcells and macrocells for land mobile communications, a propagation loss estimation model in which environmental information such as buildings and terrain is pre-processed into two-dimensional matrix data as feature quantities, and feature extraction using CNN and regression using FNN is widely used and achieves high accuracy. In the pre-processed matrix data, the array positions correspond to the coordinates of the real environment, and the values represent the environment, such as the height and altitude of buildings present at these coordinates. On the other hand, when the propagation environment contains complex structures and it is considered necessary to consider their influence on propagation, the representation is considered to be insufficient. Therefore, we investigated whether expressiveness (representation of the environment) could be improved by using point cloud data for environmental information. In this paper, a study using measured data from a propagation environment around a bridge as an outdoor environment [2] and a study using sampled data from a virtual environment assuming an indoor environment [3] was conducted.

II-2.3.2. Proposed Model

It is important to understand what propagation paths exist between the transmitter (Tx) and receiver (Rx) positions and to obtain the characteristics of the propagation paths that affect the propagation loss in that environment. A method of building a machine learning model that combines two parameters has been proposed [4]. One is environmental parameters whose features are extracted from 3D data of buildings and structures. The other is system parameters, such as Tx and Rx distance, frequency, and the presence or absence of line-of-sight (LoS), which is information that depends on the communication system and scenario. The propagation loss estimation model proposed in this study is shown in Fig. II-35. The feature extraction section uses PointNet [5], which can extract features from point cloud data.

The input information is environmental information in the form of 3D data of buildings and structures, and system parameters, which are the distance between the Tx and Rx. In this paper, sampled point cloud data is generated from the environmental information as a pre-processing step. N-dimensional point cloud data is generated from the system parameter information and sampled point cloud data, and features are extracted using PointNet, a machine learning method that uses point cloud data. From this, environmental parameters are generated, and the propagation loss is calculated by combining them with the system parameters.

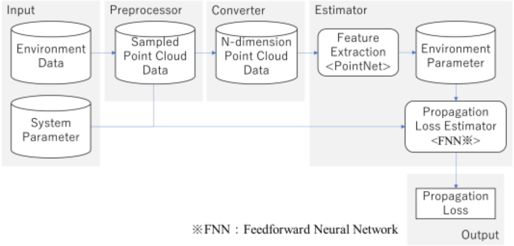

Fig. II-35. Proposed propagation loss estimation model.

Here we will explain about N-dimensional point cloud data. The point cloud data input to PointNet can be treated as N-dimensional data, which includes not only the coordinate values, but also the information that each point cloud data has due to the characteristics of the point cloud. We call this N-dimensional point cloud data (Fig. II-36).

Firstly, the point cloud data is three-dimensional coordinate data $[x, y, z]$ that indicates the position of a structure in each coordinate system. Five-dimensional point cloud data is created by adding the point cloud coordinates and the distances from the Tx and Rx points $[d_{tx}, d_{rx}]$ to this three dimensional data. By adding two distance data the data becomes five dimensional $[x, y, z, d_{tx}, d_{rx}]$. These two distance data were designed based on the results of the combination of the BS (base station or Tx) distance map and the MS (mobile station or Rx) distance map proposed in the literature [4], which showed improved accuracy.

By adding the normal vector of the plane to which each point belongs, it becomes an 8 dimensional data $[x, y, z, n_x, n_y, n_z, d_{tx}, d_{rx}]$, designed for indoor study and added so that points can recognize floors, ceilings, walls dividing rooms, etc.

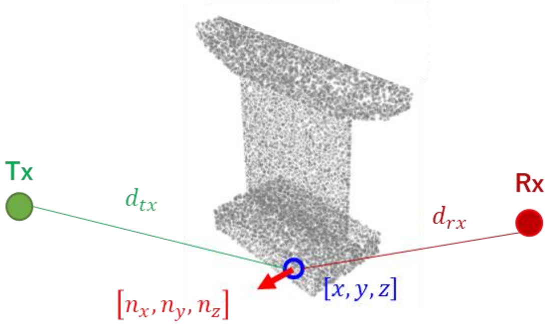

Fig. II-36. Example of N-dimensional point cloud data.

Next, we will explain the input data to PointNet generated by the environmental information conversion unit The N-dimensional point cloud data that is input to PointNet is a point cloud data with 3D coordinate information, such as point cloud data created by scanning an object. PointNet acquires features such as the positional relationship of the object that is the basis of the input data through learning, and is good at classifying and segmenting the object. In this study, we want to acquire features from the surrounding environmental information for one combination of Tx and Rx points and estimate its propagation loss value. Therefore, instead of an object, point cloud data around the Tx and Rx points is prepared and input to PointNet. In this study, the extraction target was point cloud data within a sphere centered on the Tx and Rx points and within a cylinder with the LoS of the Tx and Rx points as its center line (Fig. II-37).

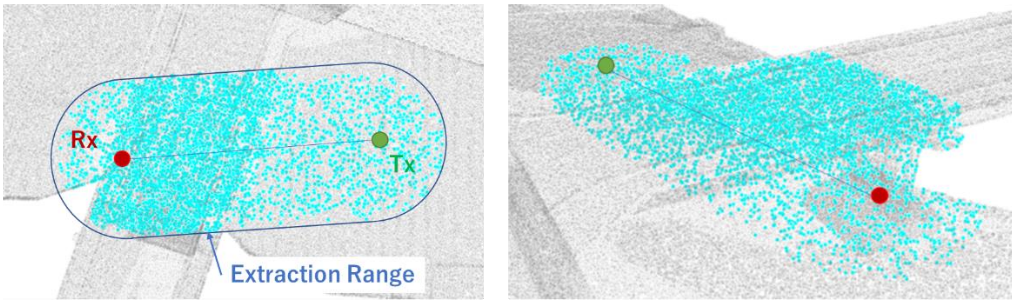

Fig. II-37. Example of input point cloud data (gray points: environment information, light blue points: extracted points)

II-2.3.3. Experiments

The performance of the proposed model was verified in the outdoor and indoor environments shown in Fig. II-38.

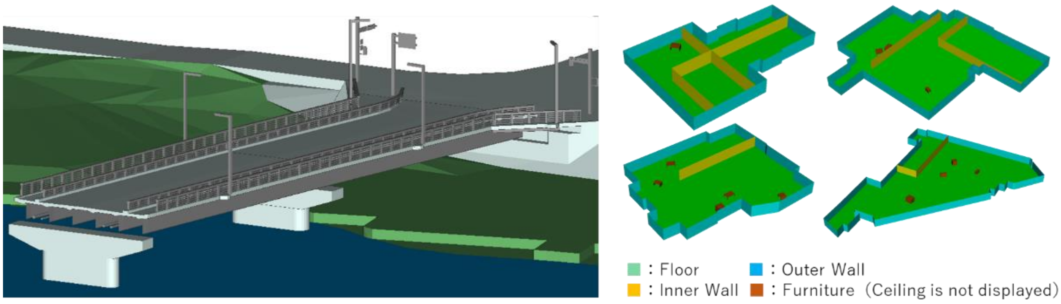

Fig. II-38. Verification environment (left: outdoor bridge environment. right: virtual indoor environment)

II-2.3.3.1. Outdoor Environment

Model training and evaluation was performed using the 2.4 GHz propagation loss values measured in the bridge environment shown on the left in Fig. II-38. The measured data were randomly split 7:3 and used for training and evaluation. The evaluation results are shown on the left-hand side of Fig. II-39, with an RMSE of 3.18 dB. The horizontal axis is the propagation loss value of the measured data and the vertical axis is the estimated value, with the light grey area indicating an error of 3 dB or less and the dark grey area indicating an error of 5 dB or less. It has been suggested that the model works as a propagation loss estimation model even when PointNet is used in the feature extraction section. However, as the validation was performed by splitting a single measurement dataset, validation of the generalization performance on different bridges is a future challenge.

II-2.3.3.2. Indoor Environment

A virtual indoor environment with multiple rooms and fixtures is prepared, as shown on the right side of Fig. II-38, and a dataset of ray tracing results is constructed at a frequency of 2.4 GHz. The indoor environment data used for learning and evaluation was divided per building, and an estimation of the area encompassing the buildings was performed, with an RMSE of 7.83 dB. An example of the evaluation results is shown on the right side of Fig. II-39. The solid lines indicate the exterior walls separating the indoor and outdoor areas, the black dotted lines indicate the interior walls, and the red dotted lines indicate the location of the fixtures. Each point in the area was estimated using PointNet. The characteristics of ray tracing, such as blockage by interior walls, the effects of diffraction, and transmission loss, were reproduced.

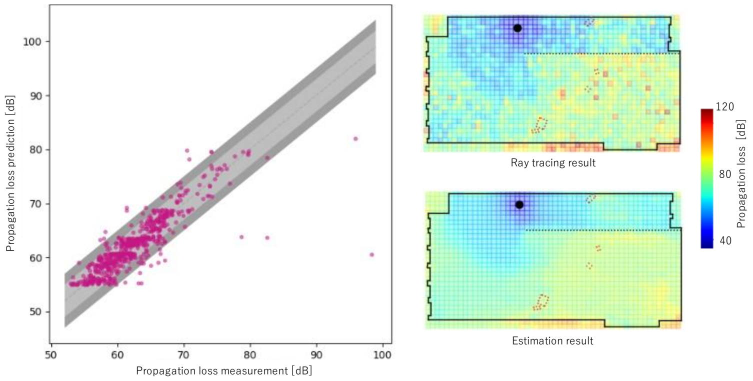

Fig. II-39. Verification results
(left: Error plot for outdoor environment. right: Area map of buildings with indoor environment)

II-2.3.4. Conclusion

This paper evaluates a machine learning model applying PointNet with point cloud data as input for outdoor and indoor environments, and confirms that point cloud data works as a means of extracting features of environmental information. We believe that this method can be used to apply machine learning models to environments with structures that are difficult to represent with CNNs, and will lead to the acquisition of highly accurate radio propagation estimation models. In the future, we plan to verify the generalization performance based on measurement data from various environments and study the feature set to improve the performance.

REFERENCE

[1] M. Vasudevan and M. Yuksel, "Machine learning for radio propagation modeling: A comprehensive survey", *IEEE Open J. Commun. Soc.*, vol. 5, pp. 5123-5153, 2024.

[2] S. Iwasaki, et. al., "Propagation Loss Estimation in Bridge Environment using 3D Structural Information as Deep Learning Features," *IEICE Technical Report*, vol. 123, no. 103, AP2023-64, pp. 181-186, Jul 2023.

[3] S. Iwasaki, et. al., "A Method for Estimating Ray-Tracing Parameters Using Machine Learning," *IEICE Technical Report*, vol. 123, no. 336, AP2023-164, pp. 24-29, Jan 2024.

[4] T. Imai, K. Kitao and M. Inomata, "Radio propagation prediction model using convolutional neural networks by deep learning", *Proc. 13th Eur. Conf. Antennas Propagat. (EuCAP)*, pp. 1-5, 2019.

[5] R. Q. Charles, H. Su, M. Kaichun and L. J. Guibas, "PointNet: Deep Learning on Point Sets for 3D Classification and Segmentation", *2017 IEEE Conference on Computer Vision and Pattern Recognition (CVPR)*, pp. 77-85, 2017.

II-2.4. Investigation of Automatic 3D model Construction Techniques of the Surrounding Environment for Ray Tracing

Kento Sugiyama, Daisuke Hosokawa, Wataru Okamura, Gilbert Ching,
Kenshi Horihata, Yukiko Kishiki
KOZO KEIKAKU ENGINEERING, INC.

***Abstract* — Ray tracing is a method of estimating propagation characteristics considering the surrounding environment, and a 3D model simulating the surrounding environment is necessary for its implementation. In this article, a method for automatically constructing a 3D model applicable to the ray tracing method from point cloud data of indoor and outdoor environments measured by a laser scanner etc. was investigated. In addition, a simplification method for 3D models of the outdoor environment was investigated to improve the calculation speed of the ray tracing method, and 3D models suitable for the ray tracing method were verified in terms of both calculation speed and accuracy.**

II-2.4.1. Introduction

Radio wave propagation simulation is useful for evaluating wireless communication systems. Ray tracing is one of the site-specific propagation estimation methods that can consider the surrounding environment, and its implementation requires a 3D model that simulates the surrounding environment. However, the task of manually creating 3D models using CAD software to evaluate each environment is time-consuming and is a bottleneck in the evaluation.

In this study, a technology to automatically construct a 3D model with surface and line information applicable to the ray tracing method from point cloud data, which is a collection of coordinate information of structures in indoor and outdoor environments measured by laser scanners, etc. was investigated. In addition, a method to simplify the 3D model for outdoor environments in order to improve the computational speed of the ray tracing method was investigated. By comparing the simulation results of the ray tracing method with measurement data, the results of verifying 3D models suitable for the ray tracing method in terms of both computational speed and accuracy are presented. [1]-[7]

II-2.4.2. 3D Modeling from Indoor/Outdoor Point Cloud Data

Fig. II-40 shows the point cloud data of indoor and outdoor environments used to consider the 3D model configuration. For indoor environments, point cloud data of one floor of an office environment was acquired using portable and fixed laser scanners. For outdoor environments, point cloud data of an urban environment was acquired using aircraft and vehicle-mounted laser scanners.

Fig. II-41 shows the 3D models automatically constructed from point cloud data in each environment. In the indoor environment, the height of the building's floor and ceiling, and the outlines of the walls and fixtures inside the building were obtained from the point cloud data, and the 3D model was constructed by combining polygonal prisms. In the outdoor environment, the height and outline of the ground and building were estimated from the point cloud data, and the 3D model was constructed by combining triangular meshes and polygonal prisms. By comparing the coordinate information of the original point cloud data and the constructed 3D model, it was confirmed that the error in constructing the 3D model was within 1m. In this way, it is possible to automatically construct a 3D model applicable to the ray tracing method with an accuracy of within 1m from the point cloud data of the surrounding environment measured by a laser scanner.

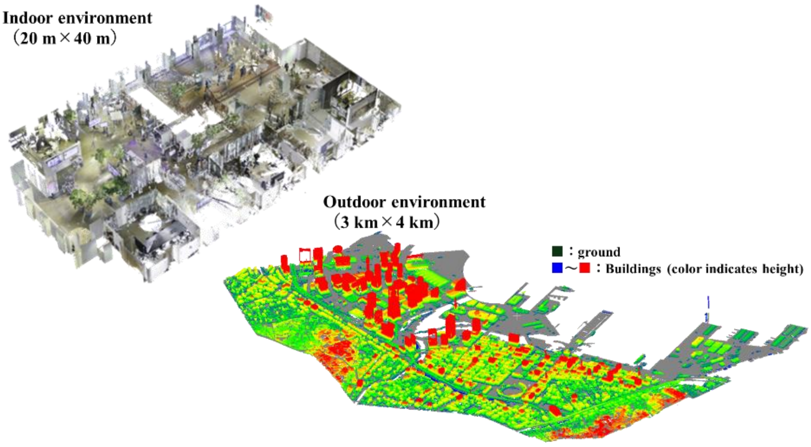

Fig. II-40. Point cloud data.

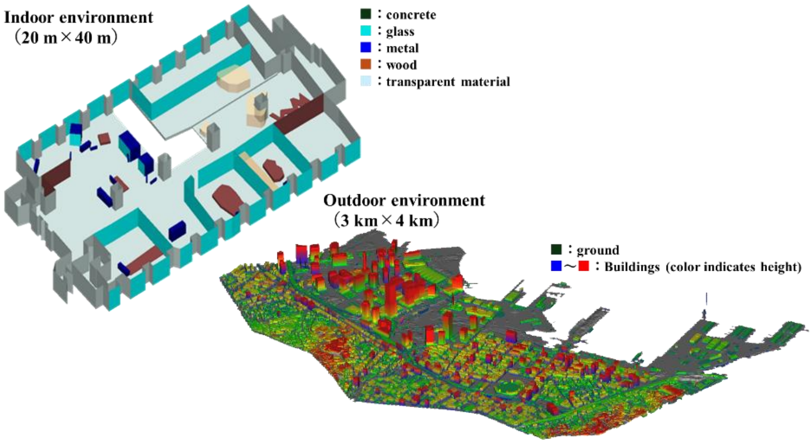

Fig. II-41. 3D model automatically constructed from point cloud data.

Fig. II-42 shows the results of applying this 3D model to the ray tracing simulation. The left figure shows the results of an area evaluation of the 2.4 GHz band in an indoor environment. It can be seen that the received power tends to fluctuate due to attenuation over distance, attenuation due to transmission through walls, and reflections from walls and surrounding fixtures. The right figure shows the results of an outdoor environment propagation evaluation of the 920 MHz band from a transmitter on the roof of a building to a receiver route along a road. Reflections and diffraction from the ground and buildings were confirmed, and it was confirmed that the trends generally matched those of actual measurements. In this way, it is possible to perform radio wave propagation simulations based on the ray tracing method using a 3D model automatically constructed from point cloud data.

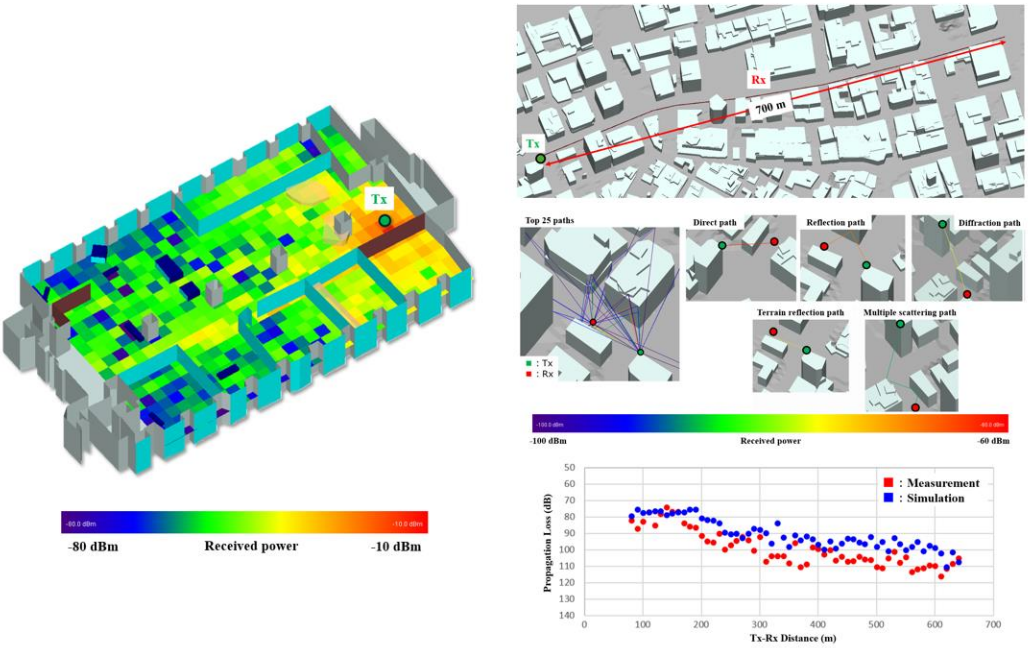

Fig. II-42. Application to ray tracing method.

II-2.4.3. Simplification of Outdoor 3D Model for Acceleration of Ray Tracing Method

When studying wireless communication systems in outdoor environments, it is expected that a wide range of studies will be required, which increases the amount of calculations for the ray tracing method. Therefore, we considered reducing the amount of calculations by simplifying the shape of the building 3D model as shown in Fig. II-43, and verified the appropriate degree of simplification of the 3D model from the perspective of calculation amount, accuracy, etc.

As shown in the figure on the right, it can be seen that the calculation speeds up the more the building 3D model is simplified. On the other hand, when the model was simplified by 10 times the wavelength, the RMSE value for all routes compared to actual measurements was below 10 dB, indicating that using a more detailed 3D model does not necessarily result in more accurate results, and that it is better to simplify surfaces to a certain extent to be close to the size of the wavelength. Since the ray tracing method is an approximation method that uses geometric optics approximation, calculations are performed using Fresnel reflection and diffraction coefficients assuming an infinite surface. For this reason, it is not suitable to use a 3D model that expresses even fine uneven shapes with a large number of surface information, and a certain degree of simplification is necessary.

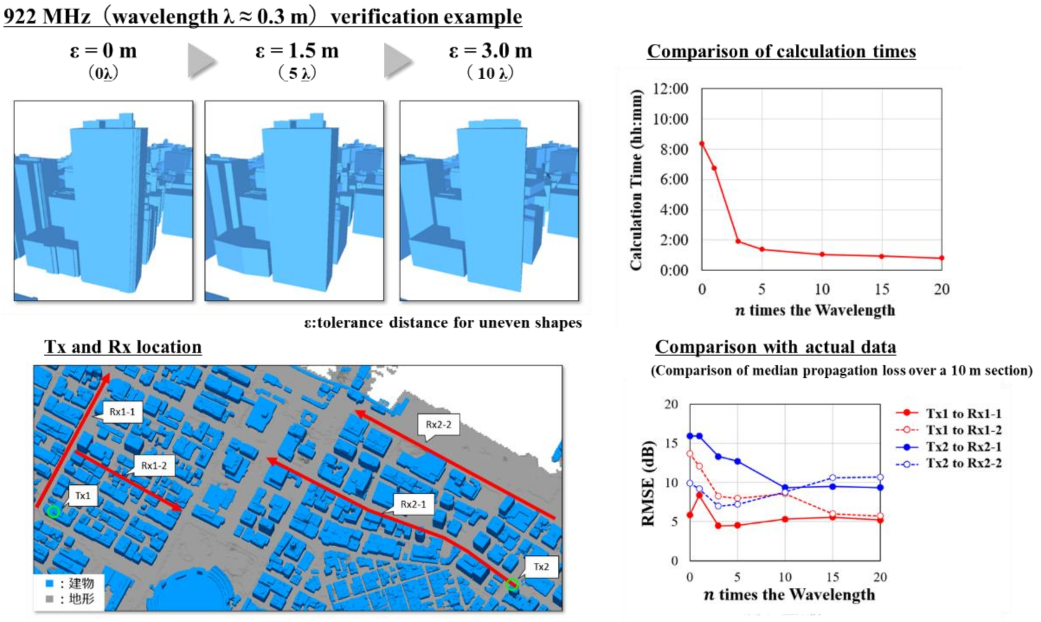

Fig. II-43. Simplification of 3D model.

II-2.4.4. Conclusion

In this paper, a technology to automatically construct 3D models with surface and line information applicable to the ray tracing method from point cloud data of indoor and outdoor environments measured by laser scanners, etc. was investigated. We confirmed that the constructed indoor and outdoor 3D models can be applied to the ray tracing method, and for outdoor 3D models, we verified 3D model simplification to obtain faster and more accurate results. We believe that the use of this method will enable efficient preparation of a simulation environment for the ray tracing method.

REFERENCE

[1] W. Okamura, K. Sugiyama, G.S. Ching, Y. Kishiki, K. Saito, J. Takada, “Indoor model reconstruction using 3D point cloud data for ray tracing simulation,” {2022 IEEE 33rd Annual International Symposium on Personal, Indoor and Mobile Radio Communications (PIMRC)}, Kyoto, Japan, pp. 1--5, Sept. 2022.

[2] K. Sugiyama, D. Hosokawa, G. S. Ching, Y. Kishiki and K. Saito, "A Study of Indoor 3D Modeling from Point Cloud Data for the CPS Wireless Emulator," The 2024 IEICE General Conference (Japanese Edition), B-1A-26, Mar. 2024.

[3] K. Sugiyama, W. Okamura, G. S. Ching, Y. Kishiki and K. Saito, "Automatic 3D Modeling of Urban Area from Point Cloud Data for Radiowave Propagation Simulation towards the CPS Wireless Emulator," IEICE Technical Report (Japanese Edition), AP2022, vol. 122, no. 378, AP2022-213, pp. 89-94, Feb. 2023.

[4] D. Hosokawa, K. Sugiyama, G. S. Ching, Y. Kishiki and K. Saito, "Accuracy Evaluation of Propagation Analysis using a High Accuracy Outdoor 3D Model for the CPS Wireless Emulator," The 2023 IEICE General Conference (Japanese Edition), B-1-24, Mar. 2023.

[5] K. Sugiyama, W. Okamura, G. S. Ching, Y. Kishiki and K. Saito, "Geometry Simplification of Automatic 3D Modeling from Outdoor Point Cloud Data for Radiowave Propagation Simulation towards the CPS Wireless Emulator," IEICE Technical Report (Japanese Edition), SRW2022, vol. 122, no. 401, SRW2022-43, pp. 1-1, March 2023.

[6] K. Sugiyama, W. Okamura, G. S. Ching, Y. Kishiki and K. Saito, "Geometry Simplification of 3D Modeling from Point Cloud Data for Radiowave Propagation Simulation of Urban Area towards the CPS Wireless Emulator," IEICE Technical Report (Japanese Edition), SRW2023, vol. 123, no. 75, SRW2023-3, pp. 13-18, June 2023.

[7] D. Hosokawa, K. Sugiyama, Y. Mizuno, Y. Kishiki and K. Saito, "Application of High-Frequency Bands in the Simplification of Outdoor 3D Models for CPS Wireless Emulator," The 2024 IEICE General Conference (Japanese Edition), B-1A-25, Mar. 2024.

II-2.5. Radio Zone Interpolation by Kriging Method

Motoharu Sasaki, Kenichi Kawamura, Minoru Inomata,
Ryoutarou Taniguchi, Wataru Yamada, Tomoaki Ogawa
NTT Corporation

***Abstract*—In this article, we propose an improved Kriging interpolation method that integrates the anisotropy of shadowing correlation based on base-station location. By transforming path-loss measurements into a distance and azimuth-angle plane, our method captures directional correlation variations, leading to more precise interpolation. Using 2.2-GHz urban path-loss data, we evaluate our approach on a dataset of 14,000 measurement points, with interpolation from 10 and 100 sampled points. Compared with four conventional interpolation methods, our proposed method significantly reduces the median and minimum root mean square error (RMSE) to 8.2 and 6.4 dB (N=10) and 4.7 and 4.2 dB (N=100), respectively. This advancement in REM construction supports enhanced network optimization and predictive communication strategies for 6G and digital twin applications.**

II-2.5.1. Introduction

The evolution towards 6G networks envisions an intelligent, hyper-connected world where digital twins and real-time simulations of physical environments play a crucial role [1]. Digital twins in wireless communications require accurate and dynamic radio environment maps (REMs) to predict and optimize communication quality in real-time. These REMs are particularly critical for autonomous vehicles and smart cities, where predictive quality of service (QoS) is essential for ensuring stable connectivity and safety.

Kriging-based interpolation is widely used for constructing REMs [2-7], but conventional methods often assume isotropic spatial correlation, which may not reflect real-world anisotropic propagation effects. These leads fail to capture the directionality of radio propagation caused by obstacles, urban structures, and base station positions. To address this limitation, we propose an anisotropic Kriging-based interpolation method that integrates spatial correlations based on both distance and azimuth angle from the base station, leading to more accurate REM construction.

The importance of considering anisotropy is illustrated in Fig. II-44, which shows the correlation dependency on azimuth angle and distance [8]. This approach enhances the precision of wireless communication predictions, facilitating the development of reliable digital twins for network optimization and autonomous system deployment.

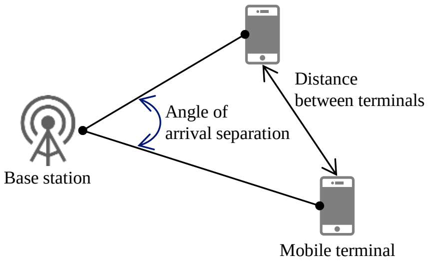

Fig. II-44. Shadowing correlation dependence on azimuth angle and distance.

II-2.5.2. Conventional Methods

Here we present the existing methods for comparison and evaluation of the proposed method.

- Nearest Neighbors Interpolation (NNI): Uses the closest observed data point for interpolation, leading to high efficiency but low accuracy.
- K-Nearest Neighbors (KNN): Averages data from the K nearest neighbors, improving accuracy at the cost of higher computation.
- Inverse Distance Weighting (IDW): Assigns weights based on inverse distances, emphasizing closer data points.
- Ordinary Kriging (OK): Interpolates using a spatial correlation model (variogram), assuming isotropic correlation [2].

II-2.5.3. Proposed Method

Our method modifies OK by incorporating anisotropic correlation shown below.

- Shadowing Correlation Dependence: Shadowing correlation varies with azimuth angle from the base station [10]. Existing studies indicate that considering this dependency enhances accuracy.
- Coordinate Transformation: Instead of using traditional latitude-longitude coordinates, we map observation points onto a plane defined by distance and azimuth angle relative to the base station as shown in Fig. II-45.
- Anisotropic Variogram: We introduce an angle-dependent range function:

  $$a' = \sqrt{a_1^2 \cos^2(\theta_{ij} - \vartheta) + a_2^2 \sin^2(\theta_{ij} - \vartheta)}$$

  where a_1 and a_2 represent different correlation ranges in the primary and perpendicular directions. The anisotropy factor $s = a_2/a_1$ is optimized using leave-one-out cross-validation.

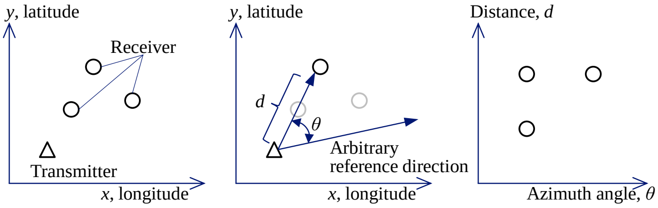

Fig. II-45. Coordinate transformation to distance and azimuth angle plane.

II-2.5.4. Evaluation and Results

We evaluated interpolation accuracy using 2.2 GHz path-loss measurements in an urban area. The dataset includes 14,000 measured points with random sampling of N=10 and N=100 as observation points. The measurement results and an example of sample data for interpolation are shown in Fig. II-46. In the evaluation, RMSE was calculated over 30 random samplings.

As shown in Fig. II-47, our method outperforms NNI, KNN, IDW, and OK, particularly when sample points are sparse (N=10). The proposed method achieves the lowest RMSE at all percentiles in the cumulative distribution function (CDF) analysis. Fig. II-48 shows RMSE distributions for different methods when N=10 and N=100. For N=10, RMSE is reduced to 8.2 dB (median) and 6.4 dB (minimum). For N=100, RMSE improves to 4.7 dB (median) and 4.2 dB (minimum).

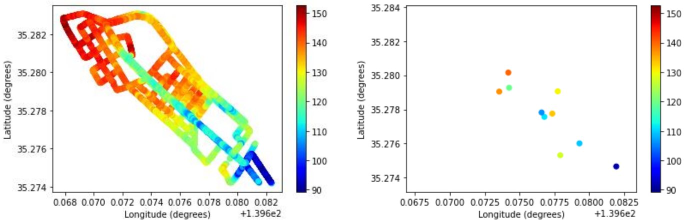

(a) All measurement (b) N=10 samples

Fig. II-46. Measurement results and example of sample data for interpolation.

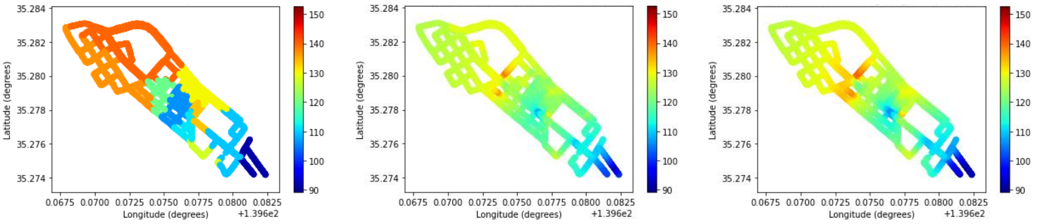

(a) NNI (b) KNN (c) IDW

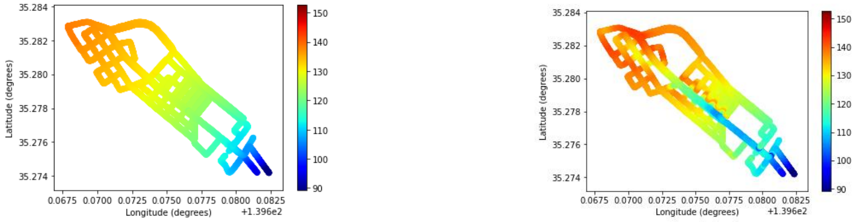

(d) OK (conv.) (e) OK w/ anisotropy (prop.)

Fig. II-47. Comparison of interpolation results for different methods.

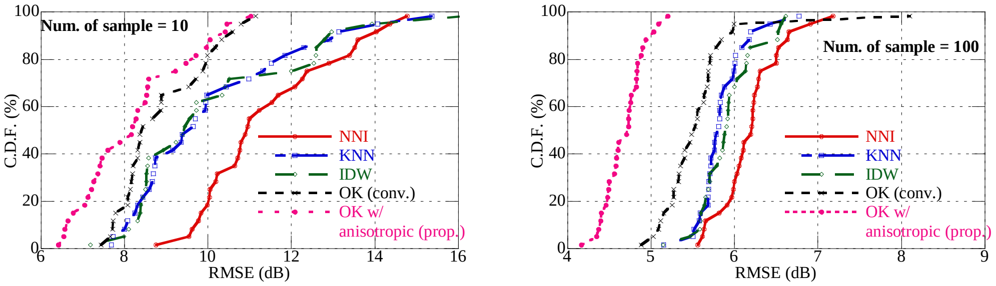

(a) N=10 (b) N=100

Fig. II-48. RMSE distributions of various interpolation methods.

II-2.5.5. Conclusion

The development of 6G networks and digital twins requires highly accurate radio environment maps (REM) to support predictive and adaptive wireless communication strategies. Our proposed anisotropic Kriging interpolation method significantly improves path-loss estimation accuracy by integrating the distance and azimuth-angle dependence of shadowing correlation. This advancement enhances REM-based predictive quality of service (QoS), enabling stable communication for autonomous vehicles, smart cities, and industrial applications.

By incorporating spatial anisotropy into Kriging-based interpolation, we contribute to the foundation of real-time, data-driven digital twins that optimize wireless communication performance. The proposed method can be integrated into next-generation network planning tools to enhance spectrum efficiency, improve link reliability, and support emerging 6G applications.

REFERENCE

[1] Recommendation ITU-R M.2083-0, "IMT Vision - Framework and overall objectives of the future development of IMT for 2020 and beyond," https://www.itu.int/rec/R-REC-M.2083.

[2] K. Sato and T. Fujii, "Kriging-Based Interference Power Constraint: Integrated Design of the Radio Environment Map and Transmission Power," IEEE Trans. on Cogn. Commun. and Netw., vol. 3, no. 1, pp. 13–25, Mar. 2017.

[3] K. Sato, K. Inage and T. Fujii, "Modeling the Kriging-Aided Spatial Spectrum Sharing Over Log-Normal Channels," IEEE Wireless Commun. Lett., vol. 8, no. 3, pp. 749–752, June 2019.

[4] C. Phillips, et al., "Practical radio environment mapping with geostatistics," 2012 IEEE Int. Symp. on Dyn. Spectr. Access Netw., Bellevue, WA, USA, pp. 422–433, Oct. 2012.

[5] Y. Gao and T. Fujii, "Kriging-based Trust Nodes Aided REM Construction under Threatening Environment," 2022 IEEE 96th Veh. Technol. Conf. (VTC2022-Fall), London, United Kingdom, pp. 1–7, Sep. 2022.

[6] Y. Deng et al., "Radio Environment Map Construction Using Super-Resolution Imaging for Intelligent Transportation Systems," IEEE Access, vol. 8, pp. 47272–47281, Mar. 2020.

[7] K. Sato, K. Suto, K. Inage, K. Adachi and T. Fujii, "Space-Frequency-Interpolated Radio Map," IEEE Trans. on Veh. Technol., vol. 70, no. 1, pp. 714–725, Jan. 2021.

[8] V. -P. Chowdappa, C. Botella, S. Santos Sáez, J. J. Samper and R. J. Martínez, "A low complexity distributed cluster based algorithm for spatial prediction," 2017 13th International Wireless Commun. and Mobile Computing Conf. (IWCMC), Valencia, Spain, pp. 2158–2162, June 2017.

[9] V. P. Chowdappa, C. Botella and B. Beferull-Lozano, "Distributed Clustering Algorithm for Spatial Field Reconstruction in Wireless Sensor Networks," 2015 IEEE 81st Veh. Technol. Conf. (VTC Spring), Glasgow, UK, pp. 1–6, May 2015.

[10] S. Szyszkowicz et al., "On the Feasibility of Wireless Shadowing Correlation Models," IEEE TVT, 2010.

[11] M. Sasaki et al., "Improving Interpolation Accuracy of Path Loss in Kriging using Anisotropy of Shadowing Correlation," 2024 IEEE 35th International Symposium on Personal, Indoor and Mobile Radio Communications (PIMRC), Valencia, Spain, Sep. 2024.

II-2.6. RNN Based Prediction Method of Wireless Communication Quality

Motoharu Sasaki, Kenichi Kawamura, Minoru Inomata,
Ryoutarou Taniguchi, Wataru Yamada, Tomoaki Ogawa
NTT Corporation

***Abstract*— This article presents a method for predicting variations in path loss using Long Short-Term Memory (LSTM) networks. The training and validation datasets consist of path loss measurements conducted in Kanagawa, Japan, at 2.2 GHz, 4.7 GHz, and 26.4 GHz. Using 100 fast-fading data points sampled at 0.1-second intervals, the model predicts the median path loss after one second. The Root Mean Square Error (RMSE) for validation data is approximately 2.2 dB at 2.2 GHz, 2.1 dB at 4.7 GHz, and 2.4 dB at 26.4 GHz, improving prediction accuracy by more than 1 dB compared to conventional methods.**

II-2.6.1. Introduction

With the advancement of 5G and the transition towards 6G, the use of higher frequency bands (above 6 GHz) is becoming essential to meet the growing demand for ultra-fast and reliable wireless communication [1]. 6G is expected to enable new paradigms such as digital twins, where real-time synchronization between physical and virtual environments is critical for applications in smart cities, autonomous vehicles, and industrial automation [2].

To support such advanced applications, network topology must be flexible and capable of dynamically managing base station connections while maintaining optimal communication quality. Predicting received power in real-time is crucial for ensuring seamless connectivity and efficient resource allocation [4]. While deep learning models, particularly LSTMs, have been explored for wireless signal processing [5,6], prior studies have mainly focused on frequencies below 6 GHz. However, millimeter-wave and sub-THz bands, essential for 6G, exhibit high path loss and severe channel variations, making accurate channel prediction even more critical [2].

This work extends path loss prediction to the 2–26 GHz range, covering both sub-6 GHz and millimeter-wave bands, without relying on external video-based data. The proposed model aims to enhance real-time channel estimation for future 6G networks, contributing to more robust and adaptive wireless communication systems.

II-2.6.2. Proposed Model Using LSTM

Fig. II-49 shows our model using LSTM, a type of recurrent neural network (RNN) that is well known for time series prediction and has been used to predict wireless communication quality in recent years [7, 8, 9, 10]. RNNs mainly have a vanishing gradient problem, which LSTM overcomes to make long-term memory possible. Our model consists of one LSTM layer with 50 units, three fully connected layers with 50 units each, and a final output layer with one unit. The input consists of 100 fast-fading data points, while the output is the median path loss one second ahead. The model is optimized using the Adam algorithm over 200 epochs.

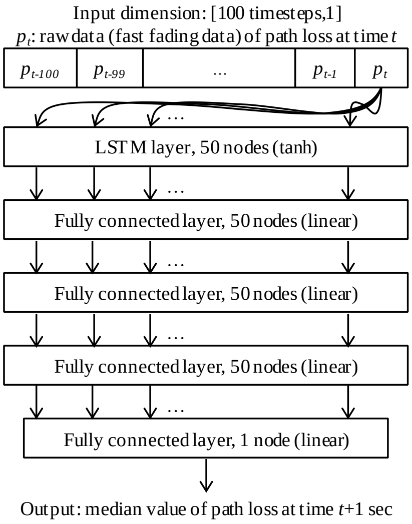

Fig. II-49. Structure of the proposed LSTM model

II-2.6.3. Measurement Method and Data Collection

Fig. II-50 shows the measurement environment. The measurements were carried out in an urban area in Yokosuka, Kanagawa, Japan. The average building height in the measurement environment was about 20 m. The buildings mainly consist of steel-reinforced concrete, reinforced concrete, or timber. We used three frequency bands (2.2, 4.7, and 26.4 GHz) and measured the path loss of all the frequencies at the same time. The Tx antennas were installed on building roofs at heights of about 16, 21, and 25 m (Tx 1, 2, and 3) in the area. The Rx antennas were set on the roof of the measurement vehicle at a height of 2.5 m. The received power was acquired at a sampling frequency of 45 kHz, but we did downsampling to 9.4 Hz before data processing (data samples were obtained about every 0.1 sec). The vehicle drove up to about 40 km/h so the running distance per sample was up to about 1 meter. The measurement path loss data of Tx1 and Tx2 are used for training, and the data of Tx3 are used to validate our LSTM model.

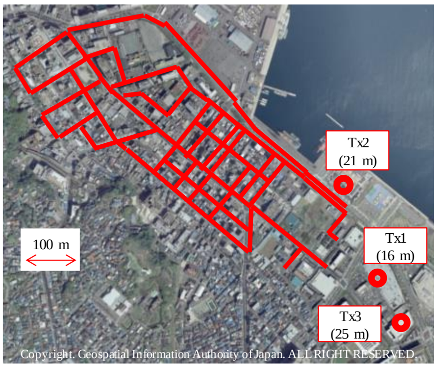

Fig. II-50. Measurement environment in Yokosuka, Kanagawa, Japan

II-2.6.4. Results and Evaluation

Fig. II-51 shows the prediction results for the validation data. We compared our model with a conventional method (Conv.) that uses the latest observed median path loss value for prediction. As can be seen from the figure, the validation data can be predicted to follow the measurement results, and the prediction is basically performed with higher accuracy than the conventional method.

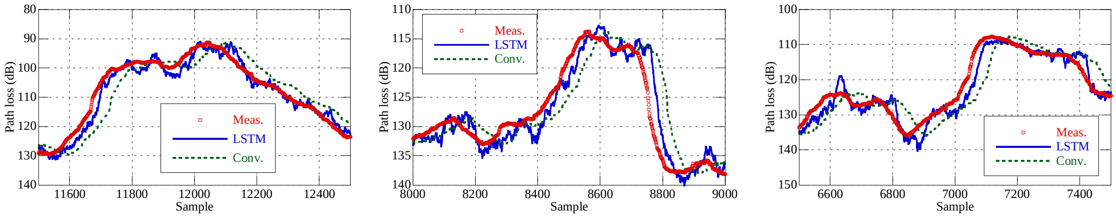

(a) 2.2 GHz (b) 4.7 GHz (c) 26.4 GHz

Fig. II-51. Example predictions for test data.

Fig. II-52 shows the root-mean-square error (RMSE) comparison results between our method using LSTM and the conventional method. In both the training data and the validation data, the RMSE is 1 dB or smaller with our method than with the conventional method. At 26.4 GHz, the RMSE of the conventional method is 4 dB or more for both training data and validation data, while the RMSE of our method is about 2.4 dB, and the RMSE is improved by 1.5 dB or more. This indicates a large path loss variation in the high frequency band and a large error with the conventional method, while our method maintains the same high prediction accuracy as other frequencies.

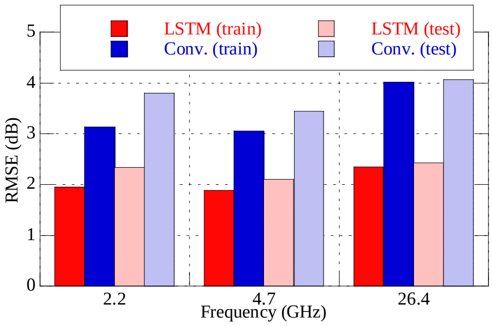

Fig. II-52. RMSEs of prediction results.

II-2.6.5. Conclusion

We proposed a method of predicting path loss using LSTM, a type of RNN used in time series prediction. The training data and validation data use the measurement results of path loss at 2.2 GHz, 4.7 GHz, and 26.4 GHz in an urban environment. The median data (median calculation interval 100 points) was predicted one second ahead using the 100 points of the acquired fast fading data as the input data. With our method, the prediction accuracy of RMSE was about 2 dB, more than 1 dB smaller than the conventional method using the latest observations in any frequency band including high frequency band of 26 GHz.

REFERENCE

[1] Recommendation ITU-R M.2083-0, "IMT Vision - Framework and overall objectives of the future development of IMT for 2020 and beyond," https://www.itu.int/rec/R-REC-M.2083.

[2] DOCOMO 6G White Paper. [Online]. Available: https://www.nttdocomo.co.jp/english/binary/pdf/corporate/technology/whitepaper_6g/DOCOMO_6G_White_PaperEN_20200124.pdf.

[3] A. Seetharam, et al., "A markovian model for coarse-timescale channel variation in wireless networks," IEEE Trans., Veh. Technol., vol. 65(3), pp. 1701–1710, 2016.

[4] C. Luo, et al., "Channel State Information Prediction for 5G Wireless Communications: A Deep Learning Approach," IEEE Trans. on Network Science and Engineering, vol. 7, no. 1, pp. 227–236, June 2018.

[5] Y. Yang, et al., "Deep Learning-Based Downlink Channel Prediction for FDD Massive MIMO System," IEEE Commun. Letters, vol. 23, no. 11, pp. 1994–1998, Nov. 2019.

[6] M. Mehrabi, et al., "Decision Directed Channel Estimation Based on Deep Neural Network k-Step Predictor for MIMO Communications in 5G," IEEE Journal on Selected Areas in Commun., vol. 37, no. 11, pp. 2443–2456, Nov. 2019.

[7] S. H. A. Shah, M. Sharma, and S. Rangan, "LSTM-Based Multi-Link Prediction for mmWave and Sub-THz Wireless Systems," ICC 2020 - 2020 IEEE International Conference on Communications (ICC), Dublin, Ireland, 2020, pp. 1–6, June 2020.

[8] Y. Yang, D. B. Smith, and S. Seneviratne, "Deep Learning Channel Prediction for Transmit Power Control in Wireless Body Area Networks," ICC 2019 - 2019 IEEE International Conference on Communications (ICC), Shanghai, China, pp. 1–6, May 2019.

[9] J. D. Herath, A. Seetharam, and A. Ramesh, "A Deep Learning Model for Wireless Channel Quality Prediction," ICC 2019 - 2019 IEEE International Conference on Communications (ICC), Shanghai, China, pp. 1–6, May 2019.

[10] A. Kulkarni, A. Seetharam, A. Ramesh, and J. D. Herath, "DeepChannel: Wireless Channel Quality Prediction Using Deep Learning," IEEE Transactions on Vehicular Technology, vol. 69, no. 1, pp. 443–456, Jan. 2020.

II-2.7. Deep Learning Propagation Loss Estimation Model Using Building Images

R. Taniguchi, W. Inomata, M. Sasaki, W. Yamada, Y. Takatori, T. Ogawa
Nippon Telegraph and Telephone Corporation

***Abstract*—Several deep neural network (DNN) models have been proposed for path loss estimation in the urban macrocell (UMa) environment, mainly using building heights around Tx and Rx as input images to the convolutional neural network (CNN). However, buildings between Tx and Rx have a more significant impact on path loss than surrounding buildings, especially when the Tx antenna is higher than them, making over-rooftop propagation dominant. These paths could enhance estimation accuracy. This article proposes a new model incorporating a side-view image of buildings along the Tx-Rx line and the conventional top-view image.**

II-2.7.1. Introduction

Deep neural networks (DNNs) have achieved remarkable success across various fields. In wireless communication system design, convolutional neural networks (CNNs) have been proposed for estimating path loss and received signal levels [1–4]. Most conventional deep learning models use top-view images of buildings around the transmitter (Tx) and receiver (Rx) as input to the CNN [1–4]. However, in urban macrocell (UMa) non-line-of-sight (NLoS) environments, the influence of nearby buildings diminishes as the distance from the transmitting station increases, making over-rooftop propagation the dominant factor. Traditional propagation models, such as the Walfisch-Ikegami and Sakagami models, incorporate over-rooftop propagation using scalar parameters [5–8]. To improve path loss prediction in the UMa environment, DNN-based models should also integrate this information appropriately. In this paper, we propose a novel DNN-based path loss prediction model that considers the propagation around Tx and Rx and the over-rooftop propagation between them. To achieve this, we introduce a side-view image along the Tx-Rx line as a new input to the CNN, complementing the conventional top-view image.

II-2.7.2. Conventional Model

A. Conventional Model by Deep Learning

Fig. II-53 shows the basic configuration of the conventional propagation loss prediction model using DNN [2–4]. In the CNN part at the initial stage, the height of the building around Rx is input as the building map, and the distance from Tx and Rx is input as the image. Depending on the model, the CNN part that inputs the building map around Tx is parallelized and connected. At the same time, system parameters such as the height of the transmitting station and the distance between transmissions and receptions are input to the fully connected neural network (FNN) part in the latter stage. The output value of the final stage is generally the path loss.

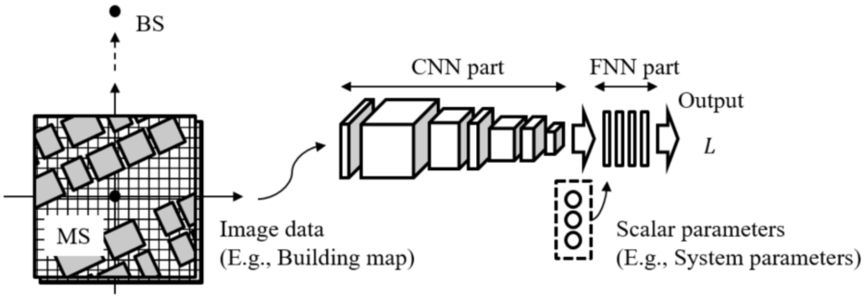

Fig. II-53. Structure of conventional model by deep learning

B. Traditional Model by Multiple Regression

In the UMa NLoS environment, as the distance from the transmitting station increases, the influence of buildings around the transmitter (Tx) and receiver (Rx) decreases. At the same time, over-rooftop propagation becomes dominant [5–8]. Fig. II-54 illustrates the concept of regression for over-rooftop propagation in the Walfisch-Ikegami model, a representative traditional approach based on this principle. This model incorporates scalar parameters that account for diffraction over rooftops and multiple reflections from buildings near Rx. Key parameters, including the distance d between Tx and Rx, the building separation b, and the road width W, are input into the model. To accurately estimate over-rooftop propagation in conventional DNN models, these factors must also be incorporated into the input image.

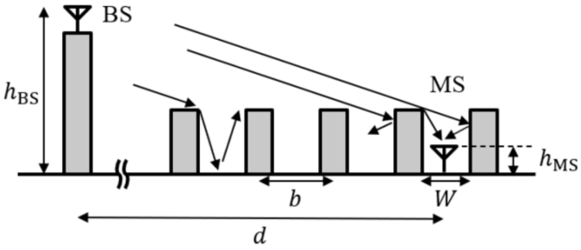

Fig. II-54. Concept of over-rooftop propagation in traditional model.

II-2.7.3. Proposed Model

A. DNN Architecture

The Fig. II-55 shows the configuration of the proposed model. Note that although the input image has been changed, the concept of how the CNN is used here is the same as that in Fig. II-53. To consider both roadside propagation and over-rooftop propagation, it is possible to incorporate both of them into the model by inputting both the top-view and the side-view image. In this case, we assume that the feature is automatically extracted from the image, so the system parameter, as shown in Fig. I-1, is not defined. However, it is possible to create a correspondence by similarly inputting the FNN part.

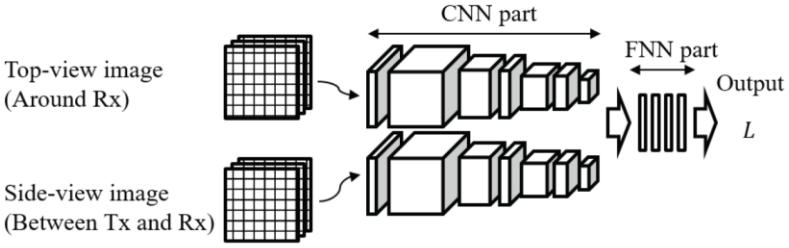

Fig. II-55. Structure of proposed model.

B. Side-View Image

The side-view image input to the proposed model is shown in Fig. II-56. Though plotted in color for ease of visualization, it is input as two-dimensional matrix data. Fig. II-56(a) shows the image of the boolean value indicating the presence or absence of a building. Fig. II-56(b) and (c) are images of the distance information from Tx and Rx, respectively, for defining the location of this building. We set the range of the y-axis to 128 m, which is sufficient for the height of the building, and the range of the x-axis to 2048 m, which is sufficient for the distance to Rx in this paper.

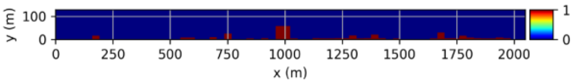

(a) Building height

(b) Distance from Tx

(c) Distance from Rx

Fig. II-56. Input side-view image to proposed model

II-2.7.4. Evaluation the Proposed Method

A. Measurement Data

The path loss data were measured with an Rx antenna mounted on a measuring vehicle. The average height of the buildings in this area was about 20 m. Three transmitting antennas with a Half Power Beam Width (HPBW) of 60 degrees were installed on the building's roof at 25 m, 21 m, and 16 m, respectively. The receiving antenna is an omni-antenna with a height of 2.5m. The measurement data were measured by switching the three patterns of Tx antenna installation positions and were limited to the NLoS environment. That is, the height of the surrounding buildings is higher than the Tx antenna position, and it is limited to the measurement data where the over-rooftop propagation between Tx and Rx becomes dominant, equivalent to Fig. II-54.

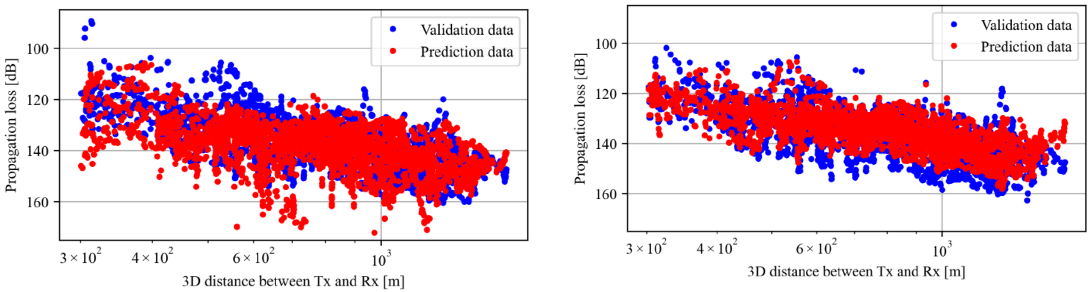

(a) Model using only side-view image

(b) Proposed model (using top-view and side-view images)

Fig. II-57. Prediction results of path loss.

B. Evaluation Results

Fig. II-57 shows the prediction results of the path loss. Although the conventional model (a) can be estimated to some extent, the variance of the prediction results is rather large regardless of the distance, and the RMS error is about 9 dB. This is probably because the over-rooftop propagation is not considered in the input image, leading to overfitting in the image around Rx. In contrast, in the result (b) of the proposed model using both the top-view and side-view images, we can confirm that the variance is suppressed. This is probably due to the improved estimation by the side-view images, which take into account the propagation between Tx and Rx, and the RMS error is less than 6 dB.

II-2.7.5. Conclusion

Conventional propagation loss estimation models using deep learning cannot input the over-rooftop propagation of buildings between Tx and Rx. We, therefore, proposed a new model in which the side-view images on straight lines are added to the input. Our evaluation using the measurement data in an urban NLoS environment demonstrated that the proposed model exceeds the estimation accuracy of the conventional model thanks to using the side-view image between Tx and Rx. We also found that the estimation error of the proposed model is less than 6 dB for the configuration using both the top and side-view images.

REFERENCE

[1] J. Thrane, B. Sliwa, C. Wietfeld, and H. L. Christiansen, “Deep learning based signal strength prediction using geographical images and expert knowledge,” in GLOBECOM 2020-2020 IEEE Global Communications Conference. IEEE, 2020, pp. 1–6.

[2] T. Imai, K. Kitao, and M. Inomata, “Radio propagation prediction model using convolutional neural networks by deep learning,” in 2019 13th European Conference on Antennas and Propagation (EuCAP), 2019, pp. 1–5.

[3] T. Hayashi, T. Nagao, and S. Ito, “A study on the variety and size of input data for radio propagation prediction using a deep neural network,” in 2020 14th European Conference on Antennas and Propagation (EuCAP). IEEE, 2020, pp. 1–5.

[4] N. Kuno and Y. Takatori, “Prediction method by deep-learning for path loss characteristics in an open-square environment,” in 2018 International Symposium on Antennas and Propagation (ISAP), 2018, pp. 1–2.

[5] J. Walfisch and H. L. Bertoni, “A theoretical model of uhf propagation in urban environments,” IEEE Transactions on antennas and propagation, vol. 36, no. 12, pp. 1788–1796, 1988.

[6] F. Ikegami, S. Yoshida, T. Takeuchi, and M. Umehira, “Propagation factors controlling mean field strength on urban streets,” IEEE Transactions on Antennas and Propagation, vol. 32, no. 8, pp. 822–829, 1984.

[7] T. Fujii, “Path loss prediction formula in mobile communication-an expansion of,” SAKAGAMI” path loss prediction formula-,” Trans. IEICE, Japan, J86-B, vol. 10, pp. 2264–2267, 2003.

[8] N. Kita, W. Yamada, and A. Sato, “Path loss prediction model for the over-rooftop propagation environment of microwave band in suburban areas,” Electronics and Communications in Japan (Part I: Communications), vol. 90, no. 1, pp. 13–24, 2007.

II-2.8. Achievable Channel Capacity of Multi-Beam MIMO Transmission at 300 GHz

Minseok Kim
Niigata University

***Abstract*— This article investigated the feasibility of multipath communication at 300 GHz using multi-beam MIMO, focusing on the achievable capacity in line-of-sight (LoS), Obstruct-LoS (OLoS), and Non-LoS (NLoS) channels. The analysis is based on a measurement campaign conducted in an outdoor hot spot environment. The findings are presented in terms of the number of nontrivial propagation streams that support multi-beam MIMO transmission. Motivated by these results, the study evaluates the average achievable channel capacity of multi-stream channels, both with and without passive reflecting surfaces (PRS). The results indicate that multi-beam MIMO significantly enhances capacity compared to single-beam systems, with PRS further improving performance.**

II-2.8.1. Introduction

Exploring frequency bands beyond 100 GHz is essential for the development of 6G communication networks, enabling advanced applications such as the metaverse, augmented reality, and holographic communications. The terahertz (THz) band offers immense potential due to its vast bandwidth, but it also introduces significant challenges, including lower output power and higher propagation loss [1]. Increasing transmission frequency allows for denser integration of antenna elements into compact designs, helping to counteract propagation loss. However, achieving optimal performance requires a comprehensive understanding of signal propagation in the targeted frequency range and an evaluation of the benefits of multiple antenna systems at both the transmitter (Tx) and receiver (Rx). Research in this field should focus not only on characterizing signal propagation but also on examining the effectiveness of multi-beam systems in mitigating propagation challenges [2]. By integrating advancements in antenna technology, signal processing, and network architecture, researchers can unlock the full potential of wireless communication beyond 100 GHz.

This article presents a channel measurement campaign conducted in an outdoor environment using an in-house-developed 300 GHz channel sounder, as described in [3]. It also details the ergodic channel capacity calculations based on a multi-beam MIMO transmission model, where the number of MIMO streams varies. The study investigates the feasibility of leveraging non-line-of-sight (NLoS) multipath components (MPCs) for spatial multiplexing to enhance channel capacity [4]. Furthermore, it examines the impact of strategically deploying passive reflecting surfaces (PRSs) on capacity improvement. By addressing these aspects, the study enhances the understanding of outdoor ultra-high-speed wireless access at 300 GHz, emphasizing the role of NLoS MPCs and PRSs in improving channel capacity.

II-2.8.2. Measurement Campaign

The channel measurement campaign was conducted in an open square environment on a university campus using an in-house-developed 300 GHz channel sounder [5]. The Tx and Rx antennas were designed with a half-power beamwidth (HPBW) of 9 degrees in the azimuth (Az) plane and had a gain of 26 dBi. Due to transmit power limitations, the received signal-to-noise ratio (SNR) degraded significantly because of the high propagation loss at 300 GHz. To address this issue, coherent averaging was applied to the continuously received symbols over 100 symbol durations during the measurement campaign. The Tx antenna was placed at the center of the square to simulate an access point (AP) or base station and was mounted at a height of 3.1 meters above ground level. The Rx antenna, acting as user equipment (UE), was positioned at 1.5 meters and sequentially moved to 15 different locations within a radial distance of 10 to 50 meters from the Tx. In the LoS scenario, represented by Rx01 to Rx11, the direct Tx-Rx link remained unobstructed. In contrast, the OLoS scenario, observed at Rx12 and Rx13, experienced partial signal obstruction due to foliage. The NLoS scenario, corresponding to Rx14 and Rx15, occurred when the direct line-of-sight path was completely blocked by surrounding buildings. To examine directional propagation characteristics, directional scan measurements were performed by rotating both the Tx and Rx antennas across a full 360-degree azimuth range in 9-degree increments.

II-2.8.3. Ergodic Capacity Evaluation

The ergodic capacity for a multi-beam MIMO transmission between a UE and an AP in an open square environment is evaluated. To simulate a multi-beam MIMO configuration, the angular samples measured at both the Tx and Rx are treated as beams, similar to a phased antenna array (PAA) beam book. Measurement results indicate the presence of three to four significant NLoS clusters on average at each position, leading to the consideration of up to four streams in the emulation. Tx-Rx beam pairs are selected based on the power of the identified clusters, establishing an $M \times M$ MIMO configuration when M Tx beams and M Rx beams are used. In the capacity calculation, the signal-to-noise ratio (SNR) for the nearest Rx position (Rx10), which experiences the lowest path loss at approximately 10 meters of separation distance, is set to 30 dB. The SNR values for other positions are adjusted proportionally based on their relative path loss compared to that at Rx10. The cumulative distribution function (CDF) of the average channel capacity is depicted in Fig. II-58, where multicolored lines represent different configurations. The results highlight that with optimal positioning, multi-stream propagation can achieve channel capacities exceeding 20 bps/Hz when the Rx is within the LoS path of the Tx. Furthermore, Fig. II-59 illustrates the increase in average channel capacity with the number of streams, showing that employing four streams nearly doubles the capacity compared to a single-input single-output (SISO) configuration. To assess the impact of PRS, metal-based PRS structures are assumed to be positioned at the interaction points of NLoS paths. The improvement in average channel capacity due to PRS is represented by multicolored dotted lines in Fig. II-59. The findings reveal that incorporating PRS in a 4×4 MIMO channel configuration results in an average achievable capacity approximately 2.7 times greater than that of SISO. These results underscore the effectiveness of beamforming in facilitating spatial multiplexing and enhancing channel capacity in THz MIMO channels for outdoor hot spot access scenarios, particularly when combined with PRS deployment.

II-2.8.4. Conclusion

This article presented double-directional channel measurements at 300 GHz in an open square hot spot scenario using high-gain directional horn antennas. Channel capacity analysis showed that even without PRS, a 9 bps/Hz capacity is achievable in LoS at 10 m with 20 dB SNR. With 4×4 MIMO and PRS, the capacity doubles, exceeding 18 bps/Hz, highlighting the potential of THz MIMO communication in open environments.

Fig. II-58. Measurement scenario.

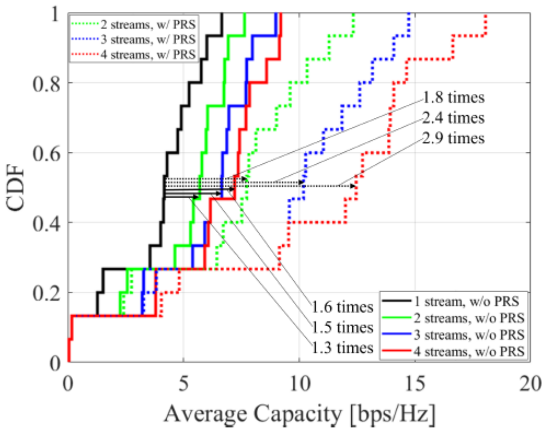

Fig. II-59. Achievable channel capacity.

REFERENCE

[1] Y. Xing et al., “Propagation Measurements and Path Loss Models for sub-THz in Urban Microcells,” *IEEE ICC 2021*, Montreal, QC, Canada, 2021.

[2] S. Ju and T. S. Rappaport, “Sub-Terahertz Spatial Statistical MIMO Channel Model for Urban Microcells at 142 GHz,” *IEEE Globecom*, Madrid, Spain, 2021.

[3] M. Kim et al., “Indoor Channel Measurement at 300 GHz and Comparison of Signal Propagation With 60 GHz,” *IEEE Access*, vol. 11, pp. 124040-124054, 2023.

[4] M. Mao et al., “MIMO Channel Capacity Measurement in Open Square Hot Spot Access Scenarios at 300 GHz,” *IEEE Wireless Commun. Lett.*, Vol. 13, No. 9, pp. 2576-2580, Sept. 2024.

[5] M. Kim, A. Ghosh, R. Takahashi and K. Shibata, "Indoor Channel Measurement at 300 GHz and Comparison of Signal Propagation With 60 GHz," *IEEE Access*, vol. 11, pp. 124040-124054, 2023

II-2.9. AI/ML-based Radio Propagation Prediction Technology

Tetsuro Imai, Tokyo Denki University
Koshiro Kitao, NTT DOCOMO. INC.
Satoshi Suyama, NTT DOCOMO. INC.

***Abstract*—Recently, advancement of AI/ML has been remarkable, and many applied research studies are attracting attention now. This is also true in the field of radio propagation. This article introduces its application to radio propagation prediction, which is currently under intensive study.**

II-2.9.1. Introduction

In recent years, artificial intelligence (AI) / machine learning (ML) has made remarkable progress, and many applied research studies have been reported. Here, they are mainly based on deep learning. The deep learning is one of the methods of ML for neural networks with many layers (or DNN: deep neural network). Deep learning has succeeded the dramatic performance improvement of image recognition, natural language processing etc., while utilizing of abundant computer resources and big data. The main reason for its success is that the deep learning can automatically extract features of contents.

In mobile communications, accurate prediction of radio propagation characteristics is needed for optimum cell design, various prediction models have been proposed so far [1]. These are categorized into two types. One is physical-based model which is based on electromagnetic theory, and another is statistical (or data-driven) model which is based on measurement data. Here, ray tracing (RT) is one of the physical-based models and has become popular tool for radio propagation analysis in recent years. In RT, various propagation characteristics such as loss, time of arrival, angle of arrival and so on can be predicted by tracing rays between transmitter (Tx) to receiver (Rx) while taking interaction (reflection, diffraction, transmission) into account. However, increasing the number of interactions considered to improve the prediction accuracy increases the computation time. So, when the target characteristic is only propagation loss, the statistical model, e.g. Okumura-Hata model [2] is preferred.

In statistical modeling, multi-regression analysis has been applied to model the data [3]. The multi-regression analysis is a very powerful tool, but it is needed to manually determine input parameters (especially environmental parameters related to building, street, etc.) and functional form beforehand. This is very difficult because there are a lot of candidates. So, the prediction models with neural network (NN) have been proposed in [4], [5]. By using these models, functional form is automatically generated, and it is reported that prediction accuracy for propagation loss is improved. However, the models are based on conventional fully connected neural network (FNN), optimal input parameters must be investigated, manually.

As mentioned above, the deep learning can automatically extract features of contents. Especially, deep convolutional neural network (DCNN) are very useful to extract features from image. This means that optimal parameters for propagation loss prediction can be automatically obtained from map data with information such as building spatial distribution. So, DCNN-based model has been proposed for propagation loss prediction [6] and is currently being vigorously studied [7]-[12]. This paper presents our latest results in [12].

II-2.9.2. DCNN-based Radio Propagation Prediction Model

II-2.9.2.1. DCNN Configuration

DCNN of our proposed model is constructed by two parts: feature extraction part and prediction part, as show in Fig. II-60.

The feature extraction part is for extraction of features of contents as key parameters for propagation loss prediction, and it is constructed by DCNN which has 13 convolutional layers: Conv_1 – Conv_13, and five max. pooling layers: Pool_1 – Pool_5. First, three maps (the size of each map: 256-by-256) are input. In Conv_1&2 layers, convolutional processing with 32 filters (the size of each filter: 3-by-3) is done and then the 32 maps (the size of each map: 256-by-256) are obtained. In next Pool_1 layer, max. pooling processing is done for 32 maps. Here, pooling size is 2-by-2, so the size of output map is reduced to 128-by-128. After the similar convolutional and pooling processing are repeated, 256 maps (the size of each map: 8-by-8) are output from Pool_5 layer. Here, the number of samples is 16384 (=8×8×256) and these are input to Dense_1 layer after conversion process to 1 D data in Flatten_1. The prediction part is constructed by FNN with two fully connected layers: Dense_1 and Dense_2. After the processing in Dense_1&2, propagation loss is predicted as output. Note that activation function is defined as: $f(x) = x$ in Dense_2 layer; otherwise, Rectified Linear Unit function, i.e. $f(x) = \max(0, x)$.

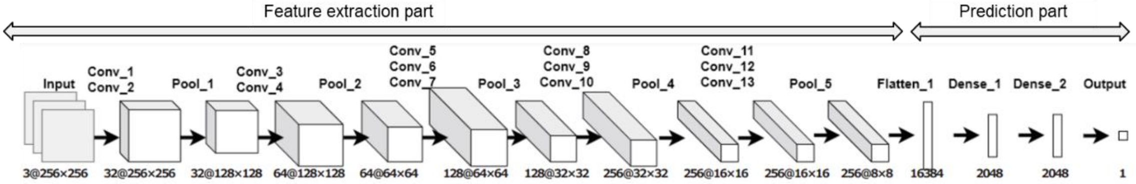

Fig. II-60. DCNN configuration

II-2.9.2.2. Input Map Data

In our model, the spatial information of rectangular area centered on mobile station (MS) position is input to DCNN as map data. The size of rectangular is 256 m -by- 256 m, and the area is sampled with 1 m mesh, so, the sample size is 256-by-256. In addition, the rectangular is defined so that the base station (BS) always exist in a certain direction. Specifically, as shown in Fig. II-61, the rectangular region is defined so that BS is oriented positively on the x_m axis in the local coordinates of the map with MS as the origin. By this definition, the spatial information about "BS direction" are indirectly considered for DCNN learning, even if the BS position are not directly input to the DCNN as parameter.

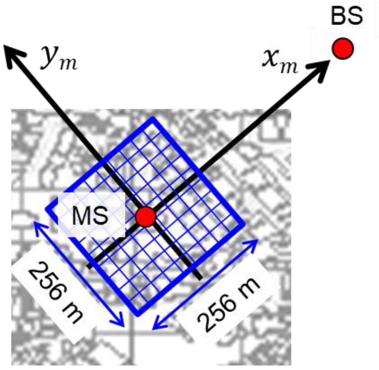

Fig. II-61. Definition of rectangular region

Input maps are three as follows.

- BS distance map: Map with distance from BS to each mesh as an element.
- MS distance map: Map with distance from MS to each mesh as an element.
- Building map: Map with building height information in each mesh.

In the building map, the height is normalized by the height of Fresnel-zone center when assuming one time scattering. This advantage is that BS antenna height and MS antenna height are indirectly considered as input parameters. Fig. II-62 shows the examples of input map data.

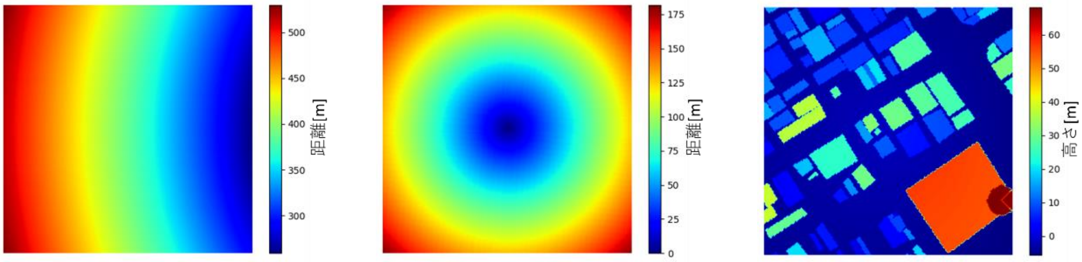

(a) BS distance map (b) MS distance map (c) Building map

Fig. II-62. Examples of input map data

II-2.9.3. Performance of DCNN-based Model

II-2.9.3.1. Measurement data

Propagation loss data measured in Kokura area are used for performance evaluation. Here, the data can be obtained for free from AP propagation database [13]. Fig. II-63 and Table. II-8 show the measurement area and conditions, respectively.

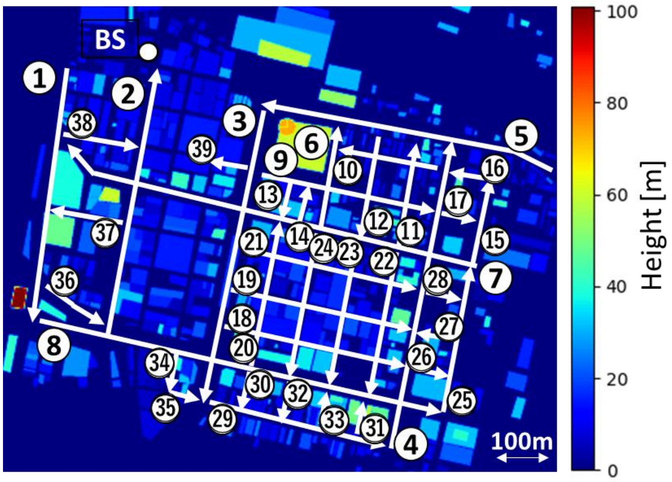

Fig. II-63. Measurement area (Kyushu Kokura area, Japan):
White lines represent measurement courses.

Table. II-8. Measurement conditions

Frequency	1298 MHz
Transmission power	39.5 dBm
BS antenna	$\lambda/2$ dipole antenna (2dBi)
MS antenna	
BS antenna height	12.5 m
MS antenna height	1.5 m

In this paper, the data of 5 courses (#6, #19, #24, #27, #32) are used for validation, the remaining data of 29 courses are for DCNN training. Here, data of course #5 is not used because sufficient input map data could be obtained. The total number of samples (or MS points) is 81 for validation and 713 for training.

II-2.9.3.2. Evaluation results

Fig. II-64 shows the prediction results for validation data. Horizontal axis represents distance from BS and vertical axis represents propagation loss. We find that measurement and prediction are agree well. Here, RMS error is 3.23 dB.

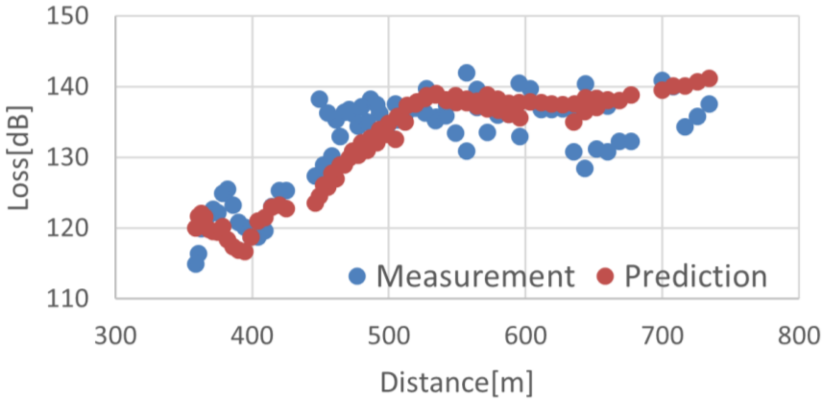

Fig. II-64. Prediction results.

The extracted features after training DCNN can be visualized by using Grad-CAM (Gradient-weighted Class Activation Mapping) [14], which one of XAI (Explainable AI) algorithms. Therefore, Grad-CAM were performed for three points as shown in Fig. II-65. Fig. II-66 shows the analysis results with Grad-CAM. In Fig. II-66, the larger the gradient value, the higher the contribution for the propagation loss prediction. From the results, DCNN-based model is thought to use the "distribution of low-rise buildings and spaces without buildings" in the vicinity of MS as the basis for determining the propagation loss prediction.

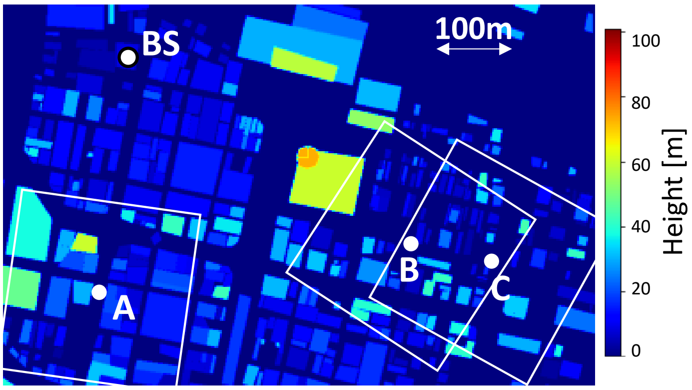

(a) Positional relationship with BS

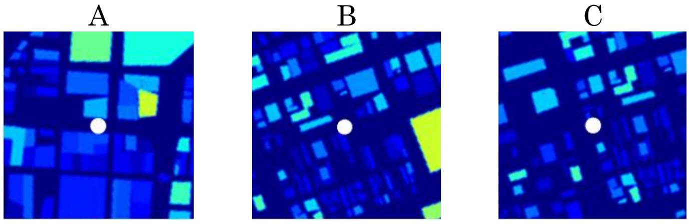

(b) Maps in local coordinate system

Fig. II-65. Reception points for evaluation of extracted features from map data.

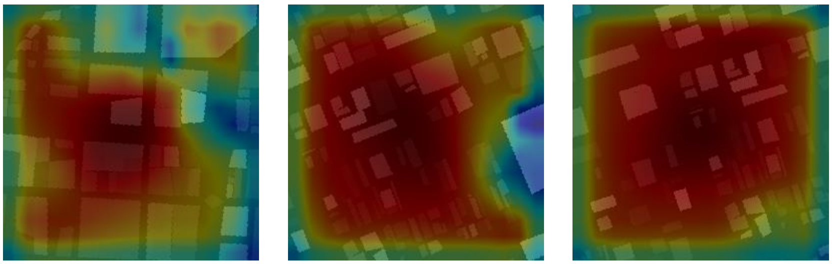
(a) Point A (b) Point B (c) Point C

Fig. II-66. Analysis results with Grad-CAM when using multiple maps.

Finally, Fig. II-67 shows propagation loss distribution predicted by trained DCNN when BS are installed in different location. Note that the other propagation conditions are same as that in table I. From this figure, we can see that even if the distance from the BS is the same, the propagation loss increases in areas with dense buildings.

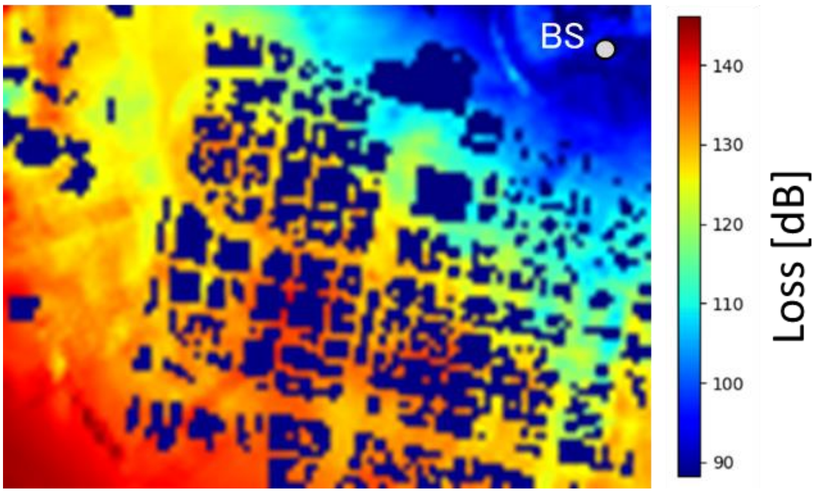

Fig. II-67. Propagation loss distribution predicted by trained DCNN.

II-2.9.4. Conclusion

In this paper, we introduced DCNN-based model for radio propagation loss prediction. This model predicts the propagation loss from map data with information such as building spatial distribution and its prediction accuracy is higher than conventional model based on multi-regression analysis. In our study, RMS error of about 3 dB is obtained. And also, we showed that the basis for determining the prediction in the DCNN-based model can be confirmed by Grad-CAM.

REFERENCE

[1] T. K. Sarkar, Z. Ji, K. Kim, A. Medour, and M. Salazar-Palma, “A Survey of Various Propagation Models for Mobile Communication,” IEEE AP Magazine, Vol. 45, No. 3, pp, 51-82, June 2003.

[2] M. Hata, “Empirical formula for propagation loss in land mobile radio services,” IEEE Trans. VT, vol. 29, no. 3, pp. 317-325, Aug. 1980.

[3] K. Kitao, and S. Ichitsubo, “Path loss prediction formula in urban area for the fourth-generation mobile communication systems,” IEICE Trans. Commun., vol. E91-B, no. 6, pp. 1999-2009, June 2008.

[4] E. Östlin, H. Zepernick, H. Suzuki, “Macrocell Path-Loss Prediction Using Artificial Neural Networks,” IEEE Trans. VT, vol. 59, no. 6, pp. 2735-2747, July 2010.

[5] M. Ayadi, A. Ben Zineb, and S. Tabbane, “A UHF Path Loss Model Using Learning Machine for Heterogeneous Networks,” IEEE Trans. AP, vol. 65, no. 7, pp. 3675-3683, July 2017.

[6] T. Imai, K. Kitao, and M. Inomata, "Radio Propagation Prediction Model Using Convolutional Neural Networks by Deep Learning," EuCAP2019, April 2019.

[7] T. Hayashi, T. Nagao, and S. Ito, “A study on the variety and size of input data for radio propagation prediction using a deep neural network,” EuCAP2020, March 2020.

[8] N. Kuno, W. Yamada, M. Inomata, M. Sasaki, Y. Asai, and Y. Takatori, “Evaluation of Characteristics for NN and CNN in Path Loss Prediction,” ISAP2020, Jan. 2021.

[9] X. Zhang, X. Shu, B. Zhang, J. Ren, L. Zhou, and X. Chen, "Cellular Network Radio Propagation Modeling with Deep Convolutional Neural Networks," in Proc. 26th ACM SIGKDD Int. Conf. Knowl. Discovery Data Mining, pp. 2378-2386, Aug. 2020.

[10] T. Nagao, T. Hayashi, “A Study on Urban Structure Map Extraction for Radio Propagation Prediction using XGBoost,” EuCAP2021, March 2021.

[11] K, Inoue, K. Ichige, T. Nagao, and T. Hayashi, “Learning-Based Prediction Method for Radio Wave Propagation Using Images of Building Maps,” IEEE AWPL, vol. 21, no. 1, pp. 124-128, Jan. 2022.

[12] K. Kozera, T. Imai, K. Kitao, and S. Suyama, “Performance Evaluation of DCNN-Based Model for Radio Propagation Loss Prediction - Analysis on Prediction Mechanism with Grad-CAM -,” IEICE Trans. Commun., vol. J106-B, no.9, pp. 618-627, Sep. 2023.

[13] AP Propagation Database: Online data repository created and supported by Technical committee on Antennas and Propagation, IEICE.
https://www.ieice.org/cs/ap/language/en/misc-eng/denpan-db/

[14] R. R. Selvaraju, et al.,” Grad-CAM: Visual Explanations from Deep Networks via Gradient-based Localization,” International Journal of Computer Vision, Dec. 2019.

Abbreviation List

Abbreviation	Explanation
ABG	Alpha-Beta-Gamma
AI	Artificial Intelligence
ALD	Atomic Layer Deposited
AMC	Adaptive Modulation and Coding
AoA	Angle of Arrival
AR	Augmented Reality
ASIC	Application Specific Integrated Circuit
AWG	Arbitrary Waveform Generator
BAN	Body Area Network
BCB	Benzo cyclobutene
BER	Bit Error Rate
BF	BeamForming
BS	Base Station
CC	Component Carrier
CI	Close-in
CMOS	Complementary Metal Oxide Semiconductor
CPS	Cyber Physical System
CSI	Channel State Information
DC	Direct Current
DFT	Discrete Fourier Transform
DL	Down Link
DNN	Deep Neural Network
DOA	Direction of Arrival
DSP	Digital Signal Processing
EIRP	Equivalent Isotropically Radiated Power
EVM	Error Vector Magnitude
eWLB	embedded Wafer Level Ball grid array
FDD	Frequency Division Duplex
FDE	Frequency Domain Equalize
FSPL	Free Space Path Loss

Abbreviation	Explanation
HARQ	Hybrid Automatic Repeat Request
HPBW	Half Power Beam Width
IBO	Input Back Off
IFFT	Inverse Fast Fourier Transform
InH	Indoor hotspot cell
ISAC	Integrated Sensing and Communication
ITU-R	International Telecommunication Union Radiocommunication Sector
KPI	Key Performance Indicator
LAN	Local Area Network
LNA	Low-Noise Amplifier
LOS	Light of Sight
LTE	Long Tern Evolution
MCM	Multichip Module
MIMO	Multiple-Input and Multiple-Output
MMIC	Monolithic Microwave IC
MS	Mobile Station
MOS	Metal Oxide Semiconductor
MOS-HEMT	Metal-Oxide-Semiconductor Eigh-Electron-Mobility Transistor
MSL	Microstrip Line
NLOS	Non-Line of Sight
NR	New Radio
NRNT	New Radio Network Topology
OAM	Orbital Angular Momentum
OFDM	Orthogonal Frequency Division Multiplexing
PA	Power Amplifier
PAE	Power Added Efficiency
PCB	Printed Circuit Board
PLE	Path Loss Exponent
QMH	Qualitative Microwave Holography
RAN	Radio Access Network
RAT	Radio Access Technology

Abbreviation	Explanation
RD	Relay Device
RF	Radio Frequency
RIS	Reconfigurable Intelligent Surface
RMSE	Root Mean Square Error
RS	Relay Station
Rx	Receiver
SAG	Selective-Area Growth
SC	Single Carrier
SiP	System-in-Package
SISO	Single-Input Single-Output
SIW	Substrate-Integrated Waveguide
SNR	Signal to Noise power Ratio
TDD	Time Division Duplex
TDS	Time Domain Spectroscopy
THz	Tera Hertz
TMA	Trimethylaluminum
TSV	Through-silicon Via
Tx	Transmitter
UCA	Uniform Circular Array
UE	User Equipment
UL	Up Link
VR	Virtual Reality